

A FERMI GAS MICROSCOPE APPARATUS

by

Dylan Jervis

A thesis submitted in conformity with the requirements  
for the degree of Doctor of Philosophy  
Graduate Department of Physics  
University of Toronto

© Copyright 2014 by Dylan Jervis

# Abstract

A Fermi Gas Microscope Apparatus

Dylan Jervis

Doctor of Philosophy

Graduate Department of Physics

University of Toronto

2014

This thesis reports on the design, construction, and performance of a new ultracold atom apparatus with the capability of resolving individual  $^{40}\text{K}$  fermions trapped in a 527 nm-period optical lattice for the purpose of investigating locally ordered quantum states. Our apparatus incorporates a high numerical aperture imaging objective to image fluorescence from the  $4S_{1/2} \rightarrow 5P_{3/2}$  transition while atoms are cooled on the  $4S_{1/2} \rightarrow 4P_{1/2}$  transition.

We demonstrate the performance of the apparatus by cooling  $^{87}\text{Rb}$  and  $^{40}\text{K}$  to quantum degeneracy in a series of magnetic quadrupole, plugged magnetic quadrupole, and optical traps. The quantum gases are created at the focus of the imaging objective, less than 1 mm from air.

We investigate the laser cooling of  $^{40}\text{K}$  atoms along the 404.5 nm  $4S_{1/2} \rightarrow 5P_{3/2}$  transition. A minimum Doppler temperature of  $63(6) \mu\text{K}$  was observed in a magneto-optical trap, as well as a factor of twenty increase in the phase space density when compared to a 766.7 nm MOT.

$^{87}\text{Rb}$  and  $^{40}\text{K}$  atoms are loaded into an optical lattice potential and measured using time-of-flight absorption imaging. With  $^{87}\text{Rb}$  atoms loaded, we are able to observe the superfluid-to-Mott insulator quantum phase transition, indicating precise control over the lattice potential. With  $^{40}\text{K}$  atoms loaded, we are able to observe the transition to a localized state.

Polarization gradient cooling of  $^{40}\text{K}$  in an optical lattice is investigated as a method to achieve single-site imaging resolution. We observe laser cooling of  $^{40}\text{K}$  to  $16 \mu\text{K}$  in free-space, and to  $12 \mu\text{K}$  in a  $200 \mu\text{K}$ -deep optical lattice.

The apparatus described in this thesis lays the groundwork for future investigations into the equilibrium and dynamical behaviour of fermionic quantum systems at the single atom level.

# Contents

<b>1</b>	<b>Introduction</b>	<b>1</b>
1.1	High resolution imaging: a local probe . . . . .	2
1.2	An ultracold gas of atoms . . . . .	4
1.3	Outline of this thesis . . . . .	9
<b>2</b>	<b>Apparatus</b>	<b>11</b>
2.1	Overview of the experimental cycle . . . . .	11
2.2	Laser system . . . . .	13
2.2.1	$^{40}\text{K}$ cooling, optical pumping, and imaging lasers . . . . .	15
2.2.2	$^{87}\text{Rb}$ cooling, optical pumping, and imaging lasers . . . . .	16
2.3	Vacuum system . . . . .	18
2.3.1	Overcoming vacuum problems . . . . .	21
2.3.2	Vacuum system details . . . . .	22
2.3.3	Vacuum clean and bake . . . . .	23
2.4	D2 Laser cooling . . . . .	24
2.4.1	MOT . . . . .	24
2.4.2	cMOT . . . . .	27
2.4.3	Optical molasses . . . . .	27
2.4.4	Optical pumping . . . . .	27
2.4.5	Laser cooling alignment . . . . .	28
2.5	Magnetic trapping and transport . . . . .	28
2.5.1	Transport hardware and electronics . . . . .	30
2.5.2	Trouble-shooting and optimizing transport . . . . .	32
2.6	RF evaporative cooling . . . . .	35
2.7	Plugged quadrupole trap . . . . .	36
2.7.1	Majorana loss . . . . .	36
2.7.2	Plugged-quadrupole evaporation . . . . .	40

2.7.3	Plug beam alignment . . . . .	40
2.8	Optical trap . . . . .	41
2.8.1	Transfer from plugged-quadrupole to crossed dipole trap . . . . .	41
2.8.2	Magnetic field zeroing . . . . .	43
2.8.3	Crossed dipole trap alignment . . . . .	43
2.9	From cold to ultracold . . . . .	44
<b>3</b>	<b>Quantum Degeneracy</b>	<b>47</b>
3.1	Thermodynamics of non-interacting quantum particles . . . . .	47
3.2	$T_F$ for trapped Fermi gases . . . . .	48
3.3	$T_c$ for trapped Bose gases . . . . .	49
3.4	Density distribution . . . . .	50
3.4.1	Density of a trapped Fermi cloud . . . . .	50
3.4.2	Density of a trapped Bose cloud . . . . .	51
3.5	Evaporation to quantum degeneracy . . . . .	52
3.5.1	A quantum gas in a plugged quadrupole trap . . . . .	52
3.5.2	A quantum gas in a crossed dipole trap . . . . .	54
3.6	Imaging and measurement . . . . .	58
3.6.1	Absorption imaging . . . . .	58
3.6.2	Time-of-flight identification of a quantum gas . . . . .	60
<b>4</b>	<b>405 nm MOT for <math>^{40}\text{K}</math></b>	<b>63</b>
4.1	$4S_{1/2} \rightarrow 5P_{3/2}$ Transition . . . . .	64
4.2	Laser and MOT Setup . . . . .	67
4.3	$4S \rightarrow 5P$ MOT of $^{40}\text{K}$ . . . . .	69
4.4	Prospects and Conclusions . . . . .	74
<b>5</b>	<b>Optical Lattices</b>	<b>77</b>
5.1	Gaussian optical lattices . . . . .	78
5.1.1	Lattice oscillation frequency and zero-point corrections . . . . .	79
5.2	Band Structure . . . . .	80
5.3	Wannier functions . . . . .	83
5.4	Fermi-Hubbard model . . . . .	83
5.4.1	Tunnelling and bandwidth . . . . .	85
5.4.2	Analytical expression for $U$ . . . . .	86
5.5	Double-well example . . . . .	86
5.5.1	The Heisenberg model as a limiting case of the Hubbard model . . . . .	88

5.6	Metal-Insulator transition in the $U \rightarrow 0$ limit. . . . .	90
5.7	Experimental creation of an optical lattice . . . . .	94
5.7.1	High power fiber coupling . . . . .	94
5.7.2	Optical lattice alignment . . . . .	97
5.7.3	Diffraction alignment . . . . .	98
5.7.4	Optical lattice heating and switch-off . . . . .	100
5.8	$^{87}\text{Rb}$ SF-MI transition . . . . .	101
5.9	$^{40}\text{K}$ localization . . . . .	105
<b>6</b>	<b>New tools for single-site imaging</b>	<b>107</b>
6.1	Imaging hardware . . . . .	108
6.1.1	Imaging requirements . . . . .	108
6.1.2	405 nm objective and sapphire imaging window . . . . .	113
6.1.3	Objective mounting and alignment . . . . .	116
6.1.4	Prospects for imaging . . . . .	116
6.2	Sub-Doppler cooling . . . . .	116
6.2.1	The Sisyphus cooling mechanism . . . . .	118
6.2.2	The $^{40}\text{K}$ D1 Sisyphus mechanism . . . . .	121
6.2.3	Raman-enhanced cooling . . . . .	122
6.3	D1 cooling observations . . . . .	123
6.3.1	Creation of 770 nm light . . . . .	127
6.3.2	D1 cooling in free space . . . . .	127
6.3.3	D1 cooling in an optical lattice . . . . .	129
<b>7</b>	<b>Conclusion and Outlook</b>	<b>135</b>
<b>A</b>	<b>Atoms in Electromagnetic fields</b>	<b>137</b>
A.1	Atom in a Magnetic field . . . . .	137
A.2	Atom in an Electric field . . . . .	139
	<b>Bibliography</b>	<b>141</b>

# List of Figures

2.1	Extended $^{40}\text{K}$ level diagram . . . . .	14
2.2	$^{40}\text{K}$ laser frequency stabilization . . . . .	16
2.3	$^{40}\text{K}$ optics layout . . . . .	17
2.4	$^{87}\text{Rb}$ laser frequency stabilization . . . . .	17
2.5	$^{87}\text{Rb}$ optics layout . . . . .	18
2.6	Vacuum system . . . . .	20
2.7	Vacuum bake timeline . . . . .	22
2.8	Vacuum bake . . . . .	23
2.9	$^{87}\text{Rb}$ and $^{40}\text{K}$ D2 level diagram . . . . .	25
2.10	MOT optics . . . . .	26
2.11	Dual $^{87}\text{Rb}/^{40}\text{K}$ MOT . . . . .	26
2.12	Magnetic transport coils . . . . .	31
2.13	Quadrupole coil circuit . . . . .	32
2.14	Magnetic transport currents . . . . .	33
2.15	Magnetic transport timing . . . . .	33
2.16	Rf and $\mu\text{wave}$ antenna . . . . .	37
2.17	Transporting atoms to imaging location . . . . .	38
2.18	Number and temperature dependance on plug beam power . . . . .	39
2.19	Plug beam alignment steps . . . . .	41
2.20	Evaporation and transfer . . . . .	42
2.21	Dipole alignment . . . . .	44
3.1	Plugged quadrupole trap potential . . . . .	53
3.2	Evaporation efficiency: plugged quadrupole v.s. quadrupole RF evaporation . . . . .	54
3.3	Crossed-Dipole trap potential . . . . .	56
3.4	A comparison of $^{40}\text{K}$ loss for $^{87}\text{Rb}$ in different hyperfine ground states. . . . .	57
3.5	$^{40}\text{K}$ evaporation in crossed-dipole trap . . . . .	59
3.6	A degenerate cloud of $^{87}\text{Rb}$ and $^{40}\text{K}$ . . . . .	60

4.1	<sup>40</sup> K excited state level diagram . . . . .	65
4.2	405 nm cooling and trapping . . . . .	67
4.3	405 nm MOT experiment . . . . .	68
4.4	405 nm trapped cloud measurements . . . . .	70
4.5	405 nm intensity requirements . . . . .	71
4.6	405 nm MOT lifetime . . . . .	72
4.7	405 nm MOT performance . . . . .	73
4.8	405 nm molasses cooling . . . . .	74
5.1	<sup>40</sup> K Band Structure . . . . .	82
5.2	Energy spectrum of double-well Fermi Hubbard Hamiltonian . . . . .	87
5.3	Eigenvalues and Eigenstates of a 1D Optical lattice . . . . .	91
5.4	Site filling . . . . .	93
5.5	Lattice optics . . . . .	95
5.6	High power fiber coupling . . . . .	96
5.7	Forward lattice beam alignment . . . . .	97
5.8	Kaptiza-Dirac Alignment . . . . .	99
5.9	Kapitza-Dirac diffraction period . . . . .	100
5.10	Lattice heating . . . . .	101
5.11	Mott insulator - superfluid transition . . . . .	103
5.12	<sup>40</sup> K localization . . . . .	105
6.1	Single-site imaging approach . . . . .	109
6.2	3D Intensity distribution from a point source . . . . .	110
6.3	Discerning the presence (or not) of an atom . . . . .	112
6.4	Imaging fidelity . . . . .	112
6.5	Sapphire window brazed to Ti sub-flange . . . . .	114
6.6	Methods for objective characterization . . . . .	115
6.7	Toy atom level diagram . . . . .	118
6.8	<sup>40</sup> K D1 energy levels in $lin \perp lin$ polarization lattice . . . . .	122
6.9	$\Lambda$ -cooling mechanism . . . . .	124
6.10	<sup>40</sup> K D1 level structure and spectroscopy . . . . .	125
6.11	D1 laser table schematic . . . . .	126
6.12	D1 cooling sequence from MOT . . . . .	126
6.13	D1 sub-Doppler cooling time . . . . .	128
6.14	D1 sub-Doppler detuning dependence . . . . .	129

6.15 D1 lattice optics . . . . .	131
6.16 Temperature v.s. lattice depth . . . . .	133
6.17 <i>In situ</i> temperature v.s. repump detuning . . . . .	133

# Preface

I have been fortunate to have worked with some extraordinary graduate students, post-docs, research engineers, undergraduate summer students, exchange students, and professors during my time in graduate school. Chief among them has been Dave McKay. Dave’s contributions to this experiment are partially detailed in his thesis [1]. Specific contributions of note are: the architecture of the MATLAB sequence and acquisition control program, the design of the 405 nm laser optics, vacuum system design and construction, laser frequency stabilization electronics, and interlock electronics. Most importantly, Dave has been a wise voice in the lab and a model researcher. He was the driving force behind the decision to switch from an all- $^{40}\text{K}$  evaporation (which had been unsuccessful due to  $^{40}\text{K}$  source problems) to a dual  $^{87}\text{Rb}$ - $^{40}\text{K}$  evaporation.

Graham Edge has been instrumental in designing the optics layout, and testing the laser source, for the optical dipole and lattice traps. Graham also built the latest (and most successful) iteration of  $^{40}\text{K}$  dispensers for the experiment.

Stefan Trotzky designed the optical lattice intensity servo and provided countless creative solutions and approaches to problems. Alan Stummer designed and built most of the electronics for the magnetic transport system. Karl Pilch designed and constructed the Feshbach current stabilization electronics.

Matthias Scholl, Felix Stubenrauch, Will Cairncross, and Simon Heun have all built and tested lasers for the apparatus. Dan Fine built many frequency stabilization “lock” boxes and helped to evaluate 405 nm laser sources. Josefine Metzkes and Michael Yee were responsible for designing most of the hardware components for the magnetic transport system. Carolyn Kierans designed the high-resolution imaging mounts and, along with Gabriello Presenza-Pitman and Thomas Maier, helped characterize the performance of the imaging system. Ryan Day helped with D1 laser locking and optics setup.

Joseph Thywissen was the lead on many specific projects as well as being responsible for all higher-level lab functions. Joseph had principal roles in the vacuum and transport system design, the decision to build and employ interference filter lasers, the imaging system design and characterization, early lab infrastructure and “plumbing”, the decision to pursue gray molasses

cooling in the optical lattice after 405 nm Doppler cooling had failed, and many others. Joseph imagined this project, and I have found the challenge in trying to make it come to life rewarding.

The publications arising from the apparatus described in this thesis are:

- D. Jervis, J.H. Thywissen (2014). Making an ultra cold gas. arXiv:1401.7659. *To appear in “Quantum gas experiments - exploring many-body states”, edited by P. Törmä and K. Sengstock, Imperial College Press, London.*
- D.C. McKay, D. Jervis, D.J. Fine, J.W. Simpson-Porco, G.J.A. Edge and J.H. Thywissen (2011). Low-temperature high-density magneto-optical trapping of potassium using the open  $4S \rightarrow 5P$  transition at 405 nm. *Physical Review A*. 84 063420.

During my graduate school career, I have also had the opportunity to contribute parts of apparatus and analysis to research groups outside of the Fermi gas microscope lab, resulting in the following publications:

- T.J. Nott, E. Petsalakis, P. Farber, D. Jervis, E. Fussner-Dupas, A. Plochowitz, T. Craggs, D. Bazett-Jones, J. D. Forman-Kay, A. J Baldwin, and T. Pawson. (2014). Phase transition of a disordered Nuage protein generates environmentally responsive membrane-less organelles. *To appear in Molecular Cell Biology.*
- M. K. Ivory, A. R. Ziltz, C. Fancher, A. J. Pyle, A. Sensharma, B. Chase, J. P Field, A. Garcia, D. Jervis, and S. Aubin (2014). Atom chip apparatus for experiments with ultracold rubidium and potassium gases. *To appear in Review of Scientific Instruments.*
- L.J. LeBlanc, A.B. Bardon, J. McKeever, M.H.T. Extavour, D. Jervis and J.H. Thywissen (2011). A tunable bosonic superfluid junction. *Physical Review Letters* 106, 025302.

# Chapter 1

## Introduction

An ultracold gas of atoms is a highly controllable system that allows access to a wide range of quantum behaviour. The fact that a collection of atoms, when cold enough, obeys the same quantum statistics as electrons, protons, photons, and other fundamental particles means that by building a quantum gas apparatus, the experimental physicist has created a playground in which to tinker with and observe universal physics.

In recent years, ultracold gas systems have been used to measure a wide range of behaviour, including: the phase diagram of a two-spin Fermi system [2, 3], Sakharov oscillations analogous to those in the cosmic microwave background radiation [4], an observation of the Higgs mode [5], quantum limited spin transport [6, 7, 8], and magnetic ordering [9, 10, 11].

One of the major areas that ultracold atoms research has directed itself towards is the simulation of strongly correlated condensed matter. A strongly correlated system might be defined as a system in which the behaviour of one constituent part depends on the state of many of the other constituent parts. This makes them especially difficult to theoretically model, and so ripe for experimental investigation. Strongly correlated materials, such as cuprate superconductors, also exhibit interesting phase behaviour which makes them especially attractive as targets for study. Cuprates may superconduct, order themselves anti-ferromagnetically, be pseudo-gapped, or act like a normal metal depending on the temperature, pressure, and doping of the sample [12]. However, these systems are still not well enough understood that there exists a model proven to comprehensively explain all of the observed behaviour. If there were such a model, then one might hope to be able to engineer materials that would superconduct, for example, at ambient temperature and pressure.

In 1981, Richard Feynman proposed using a simple quantum system to simulate a more complex one [13]. His underlying idea was that a better understanding of a certain physical behaviour is demonstrated when one is able to engineer, or simulate, that same behaviour -

from the ground up - with a computer of some kind. This idea has motivated and defined the field of quantum simulation ever since.

Quantum simulation of materials, then, involves the creation of an experimental analogue of a theoretical model that is *thought* to explain the behaviour of electrons in crystals. The theoretical model that this thesis is chiefly concerned with simulating is the Fermi-Hubbard model [14]:

$$\hat{H}_{\text{FH}} = -J \sum_{\sigma} \sum_{\langle i,j \rangle} \hat{b}_{i\sigma}^{\dagger} \hat{b}_{j\sigma} + \frac{U}{2} \sum_{\sigma \neq \sigma'} \sum_i \hat{b}_{i\sigma}^{\dagger} \hat{b}_{i\sigma'}^{\dagger} \hat{b}_{i\sigma'} \hat{b}_{i\sigma}. \quad (1.1)$$

The Fermi-Hubbard model is the simplest Hamiltonian that describes the competition between kinetic and interaction energies of particles trapped in a periodic potential. Here,  $\hat{b}_{i\sigma}^{\dagger}$  ( $\hat{b}_{i\sigma}$ ) are the fermionic creation(annihilation) operators that create(annihilate) a particle with spin  $\sigma$  at site  $i$ . The creation and annihilation operators obey the anti-commutation relationship  $\{\hat{b}_{i\sigma}, \hat{b}_{j\sigma'}^{\dagger}\} = \delta_{i,j} \delta_{\sigma,\sigma'}$ . The first term in Equation 1.1 parametrized by the energy  $J$  describes the hopping of particles between nearest-neighbour sites  $i$  and  $j$ . The term parametrized by  $U$  describes the on-site interaction energy between particles of different spin  $\sigma$  and  $\sigma'$ .

Although the Fermi-Hubbard model is simple to write down, it is very difficult to solve. In general, the description of an  $N$  particle quantum state requires the specification of  $2^N - 1$  complex amplitudes. Thus, describing a 300-particle system - a system barely in the thermodynamic limit - requires the description of as many complex numbers as there are particles in the Universe. In experiments, the precise control of the state of thousands of quantum particles is an increasingly feasible goal. Measurement and readout of these final states with atomic resolution has not been demonstrated, however.

Recent simulations of the Fermi-Hubbard model with ultracold fermionic atoms have demonstrated the ability to observe band insulating physics [15], the Metallic-Mott insulator phase transition [16, 17], the Metallic-Mott insulator phase transition in the presence of disorder [18], and many other phenomena. All of the Fermi-Hubbard quantum simulations to date have made measurements of the final state that were not sensitive to inter-particle distance scales of approximately 500 nm. In this thesis, we describe an apparatus that has the capability of resolving these small distances, thus realizing a position space readout measurement.

## 1.1 High resolution imaging: a local probe

The experiment described in this thesis fills a notable absence in the field of ultracold atoms: a machine that is able to measure the local behaviour of  $\hat{H}_{\text{FH}}$ . A local probe has the capability of

measuring the occupation of single sites of the optical lattice, projecting the measurement onto eigenstates of  $\hat{H}_{\text{FH}}$  itself - in the  $U/J \rightarrow \infty$  limit, at least. A local probe is also able to observe changes in the phase ordering across a sample in which the chemical potential varies due to an underlying harmonic confinement [9, 10]. Sensitive temperature measurements may also be undertaken by measuring the fluctuation in site occupation as a function of lattice depth and confinement [9, 19].

High-resolution imaging has recently been demonstrated for a Bose gas in the strongly correlated regime [20, 9, 10]. In constructing our apparatus, we employ an imaging strategy similar to [9, 10]: collecting the fluorescence from atoms pinned in a deep optical lattice with a high numerical aperture (NA) imaging system. The imaging resolution  $d_r$  is dependent on both the NA and the wavelength  $\lambda$  of the captured fluorescence:

$$d_r = \lambda/2\text{NA}. \quad (1.2)$$

We may minimize the resolvable distance by making the NA large and  $\lambda$  small. The NA is equal to  $n \sin \theta$ , where  $n$  is the index of refraction and  $\theta$  is the half-angle of the light cone allowed to enter the imaging aperture. The NA is increased by using a short focal length objective that is able to capture as much of the solid angle of scattered fluorescence as possible. We accomplish this with a custom designed NA=0.6 microscope placed 2 mm from an ultracold gas of atoms. In between the microscope and the atoms is a 200  $\mu\text{m}$  thick sapphire window that maintains an ultrahigh vacuum around the atoms. We may also minimize  $d_r$  by exciting atoms along the excited 405 nm  $4S_{1/2} \rightarrow 5P_{3/2}$  transition, rather than the standard 767 nm  $4S_{1/2} \rightarrow 4P_{3/2}$  transition. Taken together, this allows for a resolution of  $\approx 350$  nm, a distance smaller than the 527 nm optical lattice site spacing.

In order to detect the site occupation with high fidelity we need not only sufficient imaging resolution, but also to scatter many (of order  $10^4$ ) photons per atom to overcome limitations from shot-noise variation in the detected fluorescence. However, scattering photons will heat the atoms so that they are no longer pinned in place. We must therefore cool the atoms while an image is obtained. We may estimate to what temperature we must cool the atoms using a classical Arrhenius model for thermal hopping [21]. The hopping rate  $\Gamma_{\text{hop}}$  of an atom at temperature  $T$  across a potential with depth  $V_0$  will be proportional to the number of atoms in the sample with energy  $E > V_0$ . That is,

$$\Gamma_{\text{hop}} = \Gamma_{\text{a}} \text{erfc} \left( \sqrt{V_0/k_B T} \right) \quad (1.3)$$

where  $\Gamma_{\text{a}}$  is the attempt rate and  $\text{erfc}(x)$  is the complimentary error function.  $\Gamma_{\text{a}}$  has been

measured for  $^{133}\text{Cs}$  and  $^{87}\text{Rb}$  in an optical lattice to be  $265\text{ s}^{-1}$  [21] and  $222\text{ s}^{-1}$  [22], respectively. Taking the average of these two values, we estimate that the atomic temperature should be kept below  $V_0/7k_B$  in order for us to suppress hopping (to 10 mHz, say) during a 1 s imaging time. Technical constraints limit us to depths below  $V_0/k_B \approx 200\ \mu\text{K}$ , and so we must find a way to cool atoms to temperatures below  $30\ \mu\text{K}$  while they simultaneously scatter many photons. Our proof-of-principle solution to this problem - the sub-Doppler cooling of  $^{40}\text{K}$  using the D1 transition - is presented in this thesis.

Though many aspects of this apparatus have been designed with Fermi-Hubbard physics in mind, our experiment provides access to a wide range of quantum phenomena. In particular, creating the two-dimensional systems required for high-resolution imaging allows for the *in situ* study of pseudo-gapped phases [23], BKT physics [24], scale invariance [25], quantum critical phenomena [26], and Kibble-Zurek physics [27]. In addition, our experimental apparatus cools both fermionic  $^{40}\text{K}$  and bosonic  $^{87}\text{Rb}$ , allowing for the future high-resolution study of Bose-Fermi mixtures [28, 29] and hetero-nuclear molecular physics [30].

## 1.2 An ultracold gas of atoms

In order to apply a gas of ultracold atoms towards the study of condensed matter physics, it is necessary to understand the particularities of the ultracold atom system itself. In the following, we introduce several of the salient features important to understand the behaviour of a gas of ultracold atoms.

- **An ultracold and dilute gas is a quantum gas:** In order for a collection of atoms to behave quantum mechanically, the thermal de Broglie wavelength  $\lambda_{\text{dB}} = \sqrt{2\pi\hbar/mk_B T}$  associated with each atom must be as large or larger than the mean inter particle spacing  $n^{-1/3}$ , where  $n$  is the density and  $m$  is the atomic mass. This condition is met in cold atoms experiments when  $T \approx 100\text{ nK}$  and  $n \approx 10^{19}\text{ m}^{-3}$ , corresponding to a typical inter-particle length scale of 500 nm. The density of quantum gases may be compared with the density of the air we breathe, which at ambient pressures and temperatures has  $n_{\text{air}} \approx 10^{25}\text{ m}^{-3}$ .

If we were to try cooling a sample with higher density - easing the constraint for ultracold temperatures - we would find that the gas becomes a solid. This is because a gas at such low temperature is not in equilibrium. It is instead in a metastable state with a rate of decay equal to  $Ln^2$ , where  $L \approx 10^{-40}\text{ m}^6/\text{s}$  for  $^{87}\text{Rb}$ , for instance. If we wish to be able to study the gas for more than 1 s, we require  $n < 10^{20}\text{ m}^{-3}$ .

Lower densities, however, will reduce the thermalization rate of the gas. The collision

rate is  $\gamma = n\sigma v_T$ , where  $v_T = \sqrt{8k_B T/\pi m}$  is the relative thermal velocity [31, 32]. Constraining the temperature to the quantum regime,  $n\lambda_T^3 = 1$ , the collision rate scales as  $n^{4/3}$ . So if instead of  $n \approx 10^{19} \text{ m}^{-3}$  we had chosen a density a hundred times smaller, the collisional rate would be less than one per second, much too slow for the operation of such an experiment.

- **Energy and time scales:** The density establishes a typical energy scale,  $\epsilon = \hbar^2 n^{2/3}/m$ , at which many-body physics of interest might occur. For weakly interacting bosons, the critical temperature for superfluidity [33, 34] occurs at  $k_B T_c \approx 3.3\epsilon$ . For low-temperature fermions, the Fermi energy [33, 35] is  $E_F \approx 7.6\epsilon$ . The transition to a superfluid of paired fermions occurs at  $0.17 E_F$  for a unitary Fermi gas [36, 3].

The typical time scale is  $\hbar/\epsilon \sim 1 \text{ ms}$ . This is much longer than  $5 \mu\text{s}$  time resolution of our experiment. Therefore, a gas of ultracold atoms is a useful system in which to observe non-equilibrium physics [9, 37, 38, 39].

- **Quantum gases and spin statistics:** When the thermal de Broglie wavelength of an atom becomes as large as the system size, the wave function for the system is no longer a product of the individual atomic wave functions, but rather a single wave function of the whole collection of atoms:

$$\psi(x_1, \dots, x_i, \dots, x_j, \dots, x_N). \quad (1.4)$$

The quantum spin statistics of particles arise from the fact that quantum particles are fundamentally indistinguishable. That is, if we were to describe the many-body state of a collection of  $N$  particles, the probability must be invariant under exchange of any two particles:

$$|\psi(x_1, \dots, x_i, \dots, x_j, \dots, x_N)|^2 = |\psi(x_1, \dots, x_j, \dots, x_i, \dots, x_N)|^2. \quad (1.5)$$

To satisfy this invariance the wave function amplitude can be symmetric (+) or anti-symmetric (-) under exchange:

$$\psi(x_1, \dots, x_i, \dots, x_j, \dots, x_N) = \pm \psi(x_1, \dots, x_j, \dots, x_i, \dots, x_N). \quad (1.6)$$

The symmetry or anti-symmetry of the wave function defines the distinction between bosonic and fermionic particles. Fermionic particles must have an anti-symmetric wave function, and an immediate corollary is that two fermionic particles may never be in the

same state:

$$\psi_a(x_1, \dots, x_i, \dots, x_i, \dots, x_N) = 0. \quad (1.7)$$

This is the famous Pauli exclusion principle [40]. The spin-statistics theorem [41] relates the spin of the particle to the quantum statistics it obeys: a particle, or composite particle, with integer(half-integer) spin will obey bosonic(fermionic) quantum statistics. In our experiment, we may study both bosonic  $^{87}\text{Rb}$  and fermionic  $^{40}\text{K}$ , though our single-site imaging measurement works only for  $^{40}\text{K}$ .

- **Atoms have short-range interactions:** Neutral atoms exhibit a short-range Van der Waals potential caused by the interaction of two dipole moments that colliding atoms induce in one another. This results in a potential energy that scales with the inter-atomic distance  $r$  as:

$$V_{\text{vdW}} = -\alpha/r^6. \quad (1.8)$$

The constant  $\alpha$  must have dimensions of [energy $\times$ length<sup>6</sup>]. We may guess that the length scale is on the order the Bohr radius  $a_0$  and that the energy is a Coulomb potential  $e^2/a_0$  with  $e$  the electron charge. This gives  $\alpha = C_6 e^2 a_0^5$ , where  $C_6$  is a dimensionless constant that is equal to 4698 for  $^{87}\text{Rb}$  and 3925 for  $^{40}\text{K}$  [33].

We find the length scale associated with this potential by equating  $V_{\text{vdW}}$  with the kinetic energy of the atom:

$$\frac{\hbar^2}{m_a r_0^2} = -\frac{\alpha}{r_0^6}. \quad (1.9)$$

Using our expression for  $\alpha$  along with an expression for the electron mass obtained from equating the kinetic and potential energies of the electron  $\hbar^2/m_e a_0^2 = e^2/a_0$ , we find the range of the Van der Waals potential:

$$r_0 = (C_6 m_a / m_e)^{1/4} a_0 \approx 5 \text{ nm}. \quad (1.10)$$

The short-range character of  $V_{\text{vdW}}$  is an important requirement in simulating Fermi-Hubbard physics, for instance [42]. The Van der Waals length  $r_0$  is much smaller than the lattice spacing and so neutral atoms are well-described by the on-site interaction term in  $\hat{H}_{\text{FH}}$ .

- **Ultracold atoms have an  $s$ -wave contact interaction potential:** By being ultra-

cold, colliding atoms may only  $s$ -wave scatter, leading to an effective delta function (i.e. contact) interaction potential. The spatial wave function that describes the relative position of two atoms colliding along the  $\mathbf{z}$  direction is:

$$\psi_s = e^{ikz} + f(\theta) \frac{e^{ikr}}{r}. \quad (1.11)$$

The first term describes the incoming plane wave, the second term describes the scattered wave, and  $k$  is the relative momentum of the particles.  $f(\theta)$  is the scattering amplitude and may be expanded in terms of the partial waves  $l$  [43]:

$$f(\theta) = \sum_{l=0}^{\infty} (2l+1) \left( \frac{e^{2i\delta_l} - 1}{2ik} \right) P_l(\cos\theta) \quad (1.12)$$

with  $P_l(\cos\theta)$  the Legendre polynomials. By equating the temperature of the colliding atoms with the centrifugal and potential energy, we may determine number of partial waves to include in this sum:

$$k_B T = \frac{\hbar^2 l(l+1)}{2mr_0^2} - \frac{\alpha}{r_0^6}. \quad (1.13)$$

Therefore, atoms colder than the  $l = 1$  threshold energy - about  $10 \mu\text{K}$  for  $^{40}\text{K}$  [44] - will have only an  $l = 0$ , or  $s$ -wave, contribution to  $f(\theta)$ . Because  $s$ -wave collisions have only one available scattering state, the Pauli exclusion principle prevents two identical fermions from scattering.

We can also show that two cold alkali atoms will interact as if they were hard spheres. For small enough momentum  $k$ , the  $l = 0$  scattering amplitude becomes isotropic, momentum independent, and equal to a constant  $-a$  with the dimension of length [43]. In this low energy regime, the wavefunction  $\psi_s$  is:

$$\psi_s = 1 - \frac{a}{r}. \quad (1.14)$$

Here,  $a$  is the  $s$ -wave scattering length that gives the intercept of the wavefunction on the  $r$ -axis. It may be either positive or negative, and has the singlet(triplet) values of  $a_{s(t)} = 174(104)a_0$  for  $^{40}\text{K}$  [45] and  $a_{s(t)} = 99(90)a_0$  for  $^{87}\text{Rb}$  [46]. The physical justification for approximating  $\psi_s$  by the simple, non-oscillatory form in Equation 1.14 is that because wavefunction oscillations occur in the region  $r < r_0$  that is small compared with the mean inter-particle distance, they are unimportant for low-energy scattering behaviour and may be neglected.

Using the scattering amplitude, we may compute the scattering cross section  $\sigma$  via the differential cross section:

$$\frac{d\sigma}{d\Omega} = |f(\theta)|^2 \rightarrow \sigma = 4\pi a^2. \quad (1.15)$$

We see that two atoms scatter as if seeing each other as billiard balls with radius  $a$ . Because the de Broglie wavelength is much larger than  $r_0$  for ultracold atoms, we may define an effective *contact* interaction potential  $V_{\text{eff}}$  that is parametrized by the energy  $U_0 = 4\pi\hbar^2 a/m$  [33]:

$$V_{\text{eff}}(r) = U_0\delta(r). \quad (1.16)$$

- **Ultracold atoms in periodic potentials:** A periodic potential can be created for a gas of ultracold atoms by the standing wave intensity pattern resulting from the interference of counter-propagating laser beams. If the laser frequency is tuned just below the frequency of a nearby atomic transition, the induced dipole moment in the atom is able to orient itself so as to lower the ground state atomic energy, thus attracting the atom to high intensity regions of the electric field.

By controlling the intensity of the periodic potential, we control the potential depth and confinement and so control  $J$  and  $U$  in  $\hat{H}_{\text{FH}}$ . When the potential depth is large, the atomic wave function has less overlap with those of neighbouring states and the tunnelling energy  $J$  is reduced. The interaction energy between two atoms in the same well, say, will increase with potential depth since the resulting increase in well confinement will increase the mutual wave function overlap of the atoms. Thus, a change in the potential depth results in a change of the ratio  $J/U$  which is the relevant dimensionless parameter that determines the behaviour of a Fermi-Hubbard system. See Chapter 5 for a more detailed discussion.

- **Strong interactions, disorder, phonons, and synthetic magnetic fields in an ultracold gas:** We would like to be able to simulate a range of physical phenomena in our ultracold atomic system. This means having ways to mimic, for instance, the behaviour of electrons in a magnetic field (made possible in a sample of neutral atoms by transferring angular momentum to atoms using a pair of Raman beams [47]), to controllably introduce disorder (possible by introducing an optical “speckle” beam [48, 49, 50, 51]), and to simulate electron-phonon coupling (perhaps possible to create via a “Polaron dressing” of the sample with another atomic species [52, 53, 54]). The tuning of the interaction

energy  $U$  into the strongly-coupled regime ( $ka > 1$ ) is made possible through the use of a Feshbach resonance [55]. A Feshbach resonance exploits the energy resonance between a dimer and two free atoms at a specific value of the magnetic field  $B_0$ , resulting in an effective change in the scattering length:

$$a(B) = a \left( 1 - \frac{\Delta}{B - B_0} \right). \quad (1.17)$$

In  $^{40}\text{K}$ , the commonly used  $s$ -wave Feshbach resonance between the  $|F, m_F\rangle = |9/2, -9/2\rangle$  and  $|F, m_F\rangle = |9/2, -7/2\rangle$  Zeeman states occurs at a magnetic field  $B_0 = 202.10 \pm 0.07$  G and has a width  $\Delta = 7.8 \pm 0.6$  G [56].

Finally, it is important for the ultracold atom system to be well-controlled and reproducible if we hope to be able to simulate the subtle quantum phenomena present in strongly correlated materials. Addressing this concern is one of the primary achievements of this thesis. We have built a robust apparatus that has demonstrated the ability to coordinate many different ingredients in order to produce a sample of quantum atoms that exhibits, among other things, the behaviour described by  $\hat{H}_{\text{FH}}$ .

### 1.3 Outline of this thesis

The following chapters of this thesis describe an apparatus that is able to cool a gas of  $^{87}\text{Rb}$  and  $^{40}\text{K}$  to quantum degeneracy, control the behaviour of the gas in an optical lattice, and demonstrate a unique proof-of-principle high-resolution measurement approach. Chapter 2 describes the design, construction, and characterization of the parts of the apparatus required to cool a gas of  $^{40}\text{K}$  and  $^{87}\text{Rb}$  atoms from 500 K to a few  $\mu\text{K}$ . Chapter 3 provides a theoretical review of the thermodynamic behaviour of trapped Bose and Fermi gases, as well as the details of the experimental production of a quantum degenerate gas of  $^{87}\text{Rb}$  and  $^{40}\text{K}$ . Chapter 4 is adapted from [57] and presents a theoretical and experimental investigation into the laser cooling of  $^{40}\text{K}$  on the 405 nm  $4S_{1/2} \rightarrow 5P_{3/2}$  transition. Chapter 5 calculates the energies and states for atoms trapped in an optical lattice potential, as well as deriving  $\hat{H}_{\text{FH}}$  for an ultracold atoms system. Chapter 5 also demonstrates our control of the optical lattice potential with an observation of the  $^{87}\text{Rb}$  Superfluid-Mott Insulator transition and the site localization of  $^{40}\text{K}$ . In Chapter 6 we describe our approach to single site imaging, demonstrating the ability to cool  $^{40}\text{K}$  to 12  $\mu\text{K}$  in a  $V_0/k_B = 200 \mu\text{K}$  deep optical lattice using a sub-Doppler cooling mechanism. We offer concluding thoughts in Chapter 7.

# Chapter 2

## Apparatus

### 2.1 Overview of the experimental cycle

Unlike the samples used in condensed matter experiments, an ultracold atom sample is created and destroyed in every experimental cycle. A key component of sample preparation is attaining nanokelvin temperatures, achieved with a succession of two techniques: laser cooling and evaporative cooling. They take place in a sequence of magnetic and optical traps suited to the energy of the atom, and to the internal state of the desired quantum gas. For our choice of  $^{87}\text{Rb}$  and  $^{40}\text{K}$ , the experimental cycle proceeds similarly in several labs around the world [58, 59, 60]. We attempt here to provide a short introduction to the “life cycle” of an ultracold atoms sample in order to provide context for the work described in the following parts of this thesis.

The most widely used laser cooling technique is Doppler cooling, in which lasers are tuned to a frequency just below resonance. Atoms are pushed by the recoil momentum  $\hbar\mathbf{k}$  of photons with wavenumber  $\mathbf{k}$  scattered at a rate  $\Gamma_{\text{sc}}$  given by Equation A.9. In the rest frame of the atom, each laser beam has a frequency  $\Delta - \mathbf{k} \cdot \mathbf{v}$ , where  $\Delta = \omega - \omega_0$  is the detuning of the laser frequency  $\omega$  from the atomic transition frequency  $\omega_0$ , and  $\mathbf{v}$  is the atomic velocity. For  $\Delta < 0$ , atoms are “punished” for moving towards any incoming laser beam, since that beam is shifted towards resonance ( $\Delta = 0$ ). The resultant force is a viscous damping, whose ultimate temperature  $T_D = \hbar\Gamma/2k_B$ , the Doppler temperature [61, 62, 63], is related to the linewidth  $\Gamma$  of the transition.

Once laser cooled, atoms are magnetically transported to the science chamber. As discussed in Section A.1, atoms must have  $m_{FGF} > 0$  to be magnetically trapped.  $^{87}\text{Rb}$  atoms are polarized in the  $|2, 2\rangle$  state and  $^{40}\text{K}$  in the  $|9/2, 9/2\rangle$  using a short optical pumping light pulse.

Evaporative cooling is at work in cooling towers for air conditioning, when we perspire, and

when steam rises from a hot cup of tea. Applied to trapped atoms, the high-energy tail of a thermalized cloud will exceed the trap depth, exit the trap, and leave behind a sample with a reduced energy per particle. After further rethermalization, the temperature of the remaining cloud decreases. Unlike in laser cooling, high densities are advantageous for evaporative cooling, and there is no fundamental lower limit to temperature [64, 31, 65, 32].

Although spin mixtures of  $^{40}\text{K}$  can be evaporatively cooled [66], in our apparatus the initial collision rate would be too low to proceed in a reasonable time. Potassium is instead *sympathetically cooled* through thermalization with  $^{87}\text{Rb}$ . More generally, sympathetic cooling can be used for a species whose sources are weak or whose laser cooling is challenging. The process relies on elastic collisions between the coolant and target atoms, a way to remove the coolant without removing the target, and a sufficient heat capacity of the coolant. We find that inelastic losses are minimized for  $^{40}\text{K}$  atoms in  $|9/2, 9/2\rangle$  when  $^{87}\text{Rb}$  atoms are transferred into the absolute ground state  $|1, 1\rangle$ . This  $^{87}\text{Rb}$  internal state is not magnetically trapped, and thus sympathetic cooling is finished in an optical trap.

A recipe to create a *conservative* optical trapping potential is to use very large detuning.[67, 68] Comparing the dipole potential Equation A.10 and the scattering rate Equation A.9, we see that for large detuning the scattering cross section drops faster ( $\sim 1/\Delta^2$ ) than the dipole potential ( $\sim 1/\Delta$ ). For instance, it is common to use a trapping wavelength several hundred nanometers away from any strong resonance. For us,  $|\Delta|/\Gamma = 1.6 \times 10^7$ .

From the magnetic trap, we transfer atoms into a crossed-beam optical trap at 1054 nm. Two elliptical beams with 4.5 W and 3 W of power that are focused to waists of  $(w_{h1}, w_{v1}) = (161 \mu\text{m}, 38 \mu\text{m})$  and  $(w_{h2}, w_{v2}) = (230 \mu\text{m}, 58 \mu\text{m})$ , respectively, create a potential with a depth of  $\approx 60 \mu\text{K}$ . This is more than sufficient to contain the  $7 \mu\text{K}$  cloud produced by evaporative cooling in the magnetic trap.

After transfer to the optical trap, evaporative cooling is continued. Lowering the beam power forces evaporation, since atoms with an energy higher than the trap depth escape. We transfer  $2 \times 10^6$   $^{87}\text{Rb}$  atoms at into a crossed-beam optical trap. After 20s, we produce a Bose condensate without any discernible thermal diffraction. By sympathetic cooling in the optical trap, we also produce a quantum degenerate cloud of  $^{40}\text{K}$  atoms. We describe the thermodynamics, and our observation of, quantum gases in detail in Chapter 3.

This marks the point in the experimental cycle in which the playground of quantum many-body physics opens up: a quantum sample lies in wait, ready to be studied, manipulated, and probed. In our case, it is the Fermi-Hubbard model that we wish to explore. In order to do so, atoms are adiabatically loaded into a lattice geometry by slowly ramping on the intensity of the optical lattice beams in 200 ms. The atoms will move around and equilibrate on time scales

set by the tunnelling energy  $J$ , the on-site interaction energy  $U$ , and the underlying harmonic confinement energy  $\hbar\omega$ . For our experimental parameters, this corresponds to milliseconds or tens of milliseconds times. The competition between these energies result in a competition between metal and insulating-type behaviour of the system. Furthermore, because the response time of the atomic system is slow compared with the rates with which we are able to control the experimental parameters, we have the ability to observe non-equilibrium physics. We discuss the optical lattice in Chapter 5.

After some time evolution under the Fermi-Hubbard Hamiltonian, the state must be measured and read out. All fermion experiments to date have measured the final state using time-of-flight imaging, a method whereby the cloud is dropped from its confining potential and allowed to expand. The shape and rate of expansion indicate the original momentum distribution of the cloud *in situ*. We describe how to gain quantitative information from this technique in Section 3.6.2. To gain *positional* information, however, requires a high-resolution measurement technique that is able to resolve the 500 nm sized features created by the optical lattice. In Chapter 6, we describe an *in situ* imaging approach whereby the lattice is quickly ramped to very high intensities, freezing the atoms in place, while a 405 nm beam resonant with an excited state transition excites the atoms and causes them to fluoresce. The fluorescence is captured with a microscope objective that is placed less than 3 mm from the atoms, and atoms are kept localized during fluorescence with the simultaneous application of sub-Doppler cooling light.

## 2.2 Laser system

Lasers are the workhorse of the cold atoms physics lab. Typically, a dozen or more lasers are required to access different transitions in order to cool and image atoms, to provide a conservative confinement potential, and to amplify light. Figure 2.1 shows a selection of the different wavelengths of light used for our  $^{40}\text{K}$  and  $^{87}\text{Rb}$  experiment.

It is increasingly possible to purchase laser diodes and other bright sources that emit light at a wavelength of interest, and then integrate them into a feedback cavity that both amplifies and narrows the frequency spectrum of the light. How bright and narrow the linewidth of this light must be is determined by how it will be used. For example, light used for laser cooling must have a linewidth much less than the atomic transition linewidth  $\Gamma$ , and a power that can provide an intensity of order the saturation intensity  $I_{\text{sat}}$ . It can be hard to simultaneously satisfy both linewidth and power requirements with a single laser; an experimentalist would be thrilled to have 30 mW of light frequency stabilized to a few hundred kHz from a ‘‘Master’’ laser. However, many hundreds of mW are needed *after* losses due to optical diode protection, fiber-coupling, and acousto-optic modulator (AOM) frequency shifting are taken into account.

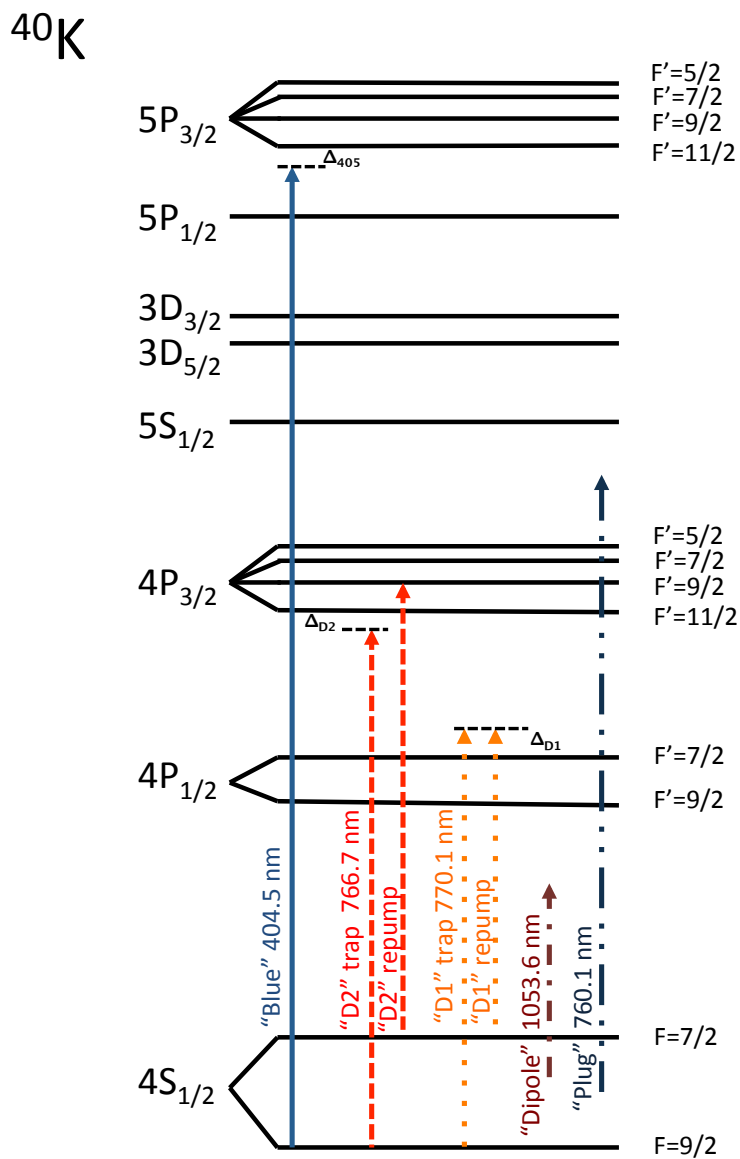


**Figure 2.1: Extended  $^{40}\text{K}$  level diagram** A selection of the wavelengths of light used to address  $^{40}\text{K}$  in the apparatus.

Therefore, the frequency stabilized light from a Master laser is often amplified by either seeding another diode laser (providing typical gains of  $\sim 10$  dB), or by seeding a tapered amplifier laser (which can provide a gains of over 25 dB).

As can be seen from Figure 2.9, cooling and imaging involves lasers tuned to number of different transitions. It is not necessary to have a separate laser for every transition, however, since AOMs are able to shift the frequency of light by many hundreds of MHz. Transitions that are separated by more than a GHz from another transition will typically have a dedicated laser. This is illustrated by comparing the case of  $^{40}\text{K}$  to  $^{87}\text{Rb}$ . Cooling any one of these atoms require both a “trap” and “repump” light, separated in frequency by approximately the hyperfine energy  $\Delta E_{\text{HF}}/\hbar$ . Because the  $^{87}\text{Rb}$  hyperfine splitting is 6.8 GHz, separate lasers are required for trap and repump light.  $^{40}\text{K}$ , on the other hand, has a hyperfine splitting of only 1.3 GHz and so is an intermediate case. In our lab, we have used separate lasers, as well as AOMs, to bridge this frequency difference during different iterations of the experiment.

Creating conservative trapping potentials requires many Watts of laser light in order to hold on to  $\mu\text{K}$ -temperature atoms. This is because of the large detuning with which the laser must operate to minimize light scattering and heating. The large power requirement is compensated, in certain applications, by a relaxed frequency stability requirement: the linewidth has only to be small enough to provide a stable, detuning-dependent potential. However, if an optical lattice potential is to be created, light that is narrow enough in linewidth to provide a stable interference intensity pattern is needed. This is a stringent requirement as the linewidth must be less than 100 kHz, small enough to prevent the accordion-like shaking of the lattice potential. As was the case for the cooling lasers, it can be difficult to produce enough power from such a stable laser. We de-couple these twin demands by using the narrow frequency light from a dedicated master laser to seed a much higher power (40 W) optical amplifier.

### 2.2.1 $^{40}\text{K}$ cooling, optical pumping, and imaging lasers

The  $^{40}\text{K}$  master laser is a Toptica DL pro. It outputs 55 mW of power, 0.5 mW of which is needed for frequency stabilization [69]. The  $^{40}\text{K}$  laser lock optics schematic is presented in Figure 2.2. We lock the frequency to the ground state cross-over feature in  $^{39}\text{K}$  using frequency modulation spectroscopy. The excited state structure of  $^{39}\text{K}$  is unresolved in saturation spectroscopy. Light resonant with the  $F = 9/2 \rightarrow F' = 11/2$  trap transition in  $^{40}\text{K}$  is produced by shifting the frequency-locked light by +700 MHz with a double-passed 170 MHz AOM, and either a single-passed 320 MHz AOM (for MOT trap light), or a double-passed 170 MHz AOM (for probe imaging light). We produce  $F = 9/2 \rightarrow F' = 9/2$  optical pumping light along the same beam path as the probe light by shifting the frequency of the double-passed 170 MHz AOM. This is

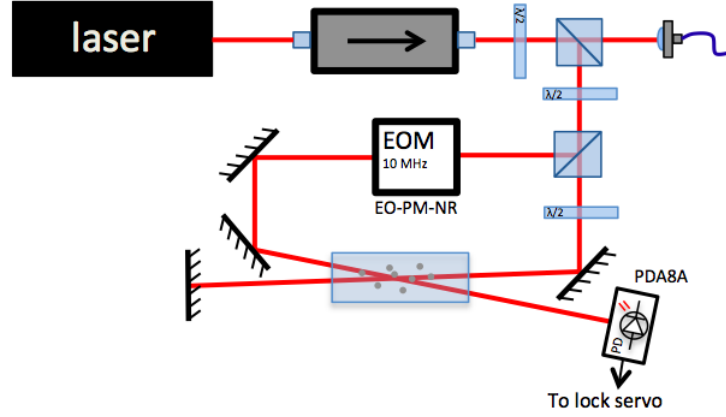


**Figure 2.2:**  $^{40}\text{K}$  laser frequency stabilization: A small amount of light from the  $^{40}\text{K}$  master laser is used for frequency stabilization. Some of this light is passed through an Electro-Optic Modulator (EOM) where it picks up frequency sidebands. This light is passed through a K vapour cell where it interacts with atoms that have been excited by the counter-propagating beam, producing a Doppler-free spectroscopy signal. The photodiode signal is then mixed with a reference oscillator, resulting in an “error” signal that may be used for frequency locking.

possible because optical and probe light are never used simultaneously. Light resonant with the  $F = 9/2 \rightarrow F' = 9/2$  repump transition is produced by shifting the frequency-locked light by  $-700$  MHz with a double-passed  $320$  MHz AOM. A schematic of the optics layout is presented in Figure 2.3.

The trap light is amplified by injection locking a “slave” laser diode after transmission through the AOMs. We use home-built tapered amplifiers (TA) to further amplify the trap and repump light from approximately  $10$  mW to  $600$  mW and  $300$  mW, respectively.

### 2.2.2 $^{87}\text{Rb}$ cooling, optical pumping, and imaging lasers

We have two  $^{87}\text{Rb}$  master lasers: a Vortex ECDL 6013 repump master, and a home-built interference filter external cavity diode trap laser constructed by Matthias Scholl [70], and based on a design described in [71]. The repump master laser is frequency stabilized using frequency modulation spectroscopy to the  $F = 1 \rightarrow F' = 1 - 2$  cross-over absorption feature. The trap master laser is frequency stabilized by beat-locking it  $+6590$  MHz away from the repump light using a reference VCO [1].

Fast control over the frequency and amplitude of the  $^{87}\text{Rb}$  light is accomplished with the help of AOMs. The trap light is shifted by a double-passed  $-110$  MHz AOM to be resonant with the  $F = 2 \rightarrow F' = 3$  transition. The optical pumping light is shifted by a double-passed  $+110$  MHz AOM to be resonant with the  $F = 2 \rightarrow F' = 2$  transition. The beat frequency can also be changed on a  $100 \mu\text{s}$  timescale to allow  $F = 2 \rightarrow F' = 3$  probe light to travel along

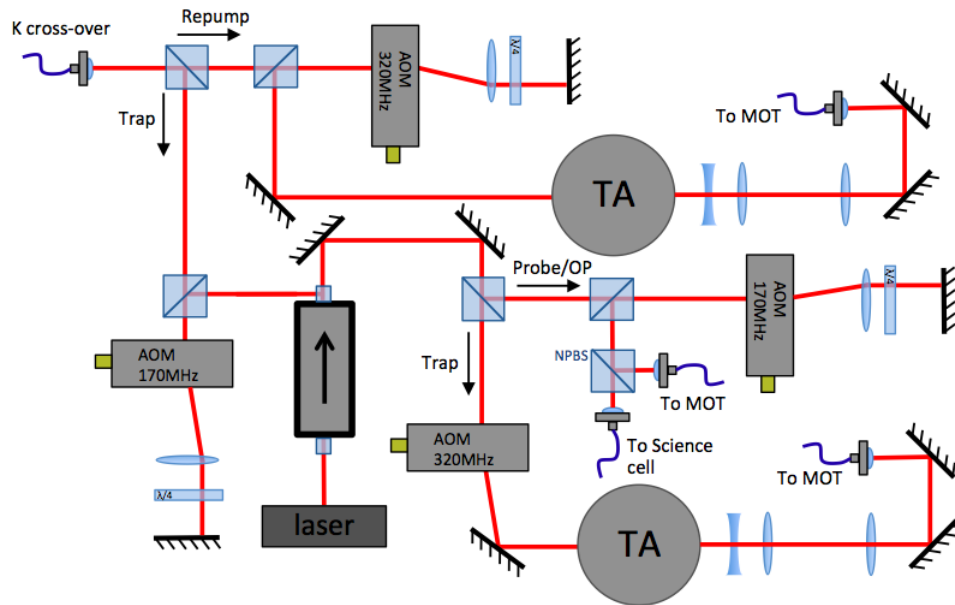


Figure 2.3:  $^{40}\text{K}$  optics layout

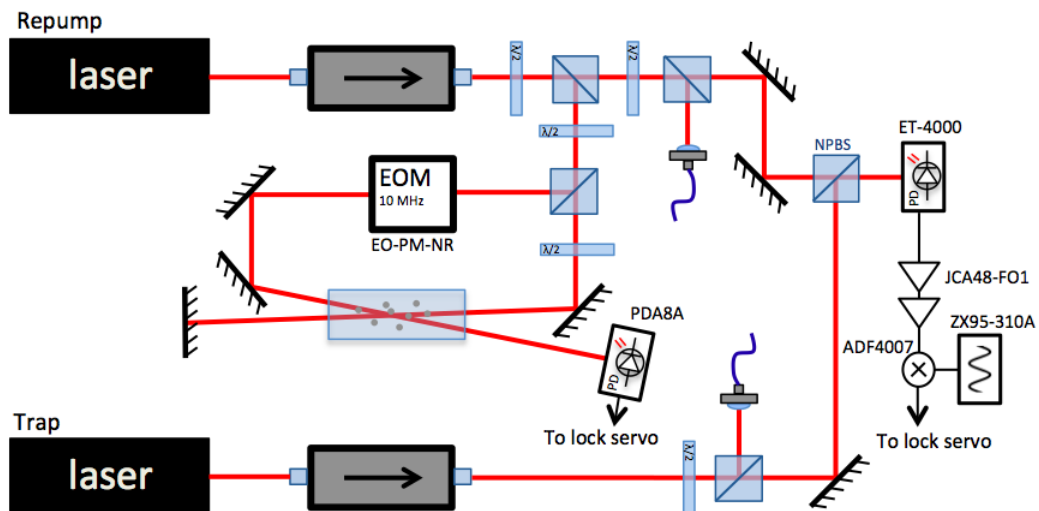


Figure 2.4:  $^{87}\text{Rb}$  laser frequency stabilization: See [1] for a description of the frequency beat lock.

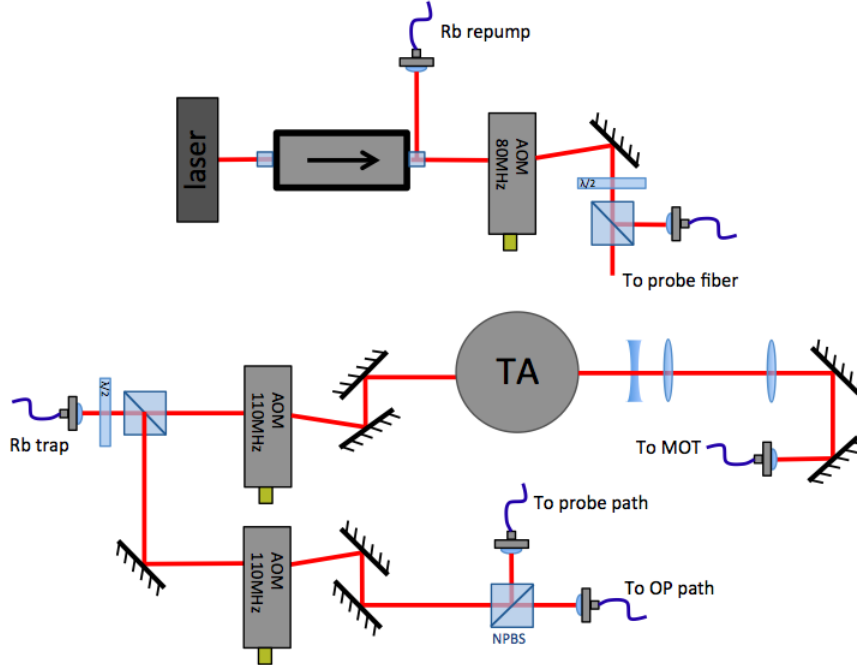


Figure 2.5:  $^{87}\text{Rb}$  optics layout

the optical pumping beam path. Whereas a TA is needed to boost the MOT trap power to 600mW before the fiber, we need only 10 mW of repump power owing to the large excited state hyperfine splitting of  $^{87}\text{Rb}$ . This power is easily achievable with an injection locked slave diode.

## 2.3 Vacuum system

An ultra cold gas of atoms has a density of  $10^{19} \text{ m}^{-3}$ , about a million times more dilute than air at atmospheric pressure and temperature. In order to thermally isolate a sample of cold atoms and protect them from the background collisions that would knock them out of traps created for them, a vacuum must be provided in which to conduct experiments.

A rule of thumb for most cold atoms experiments is that the vacuum should be separated into two regions: a (dirty) atomic source chamber, and a (clean) experimental chamber. The two chambers are connected, but kept at different pressures using either a narrow-diameter, low-conductance tube to join them, or by placing a shutter between them. Atoms are transported between the chambers either by creating a beam of atoms that then needs to be slowed down and trapped, or by first trapping and cooling atoms in the source chamber so that they can be shuttled to the experimental chamber in a well-controlled, if relatively weak, magnetic or optical trap. Zeeman slowers and 2D MOTs are examples of the first method of transport, and vapour cell MOTs plus magnetic or optical conveyor belt transport are examples of the second.

There are some exceptions to this two-chamber rule. Experiments with fast evaporative cooling cycles, for instance, do not have to worry as much about keeping their source and experimental chambers apart. Thus, experiments that use the tight magnetic confinement potential - and correspondingly large collision rate - from a lithographed atom chip, say, often operate using a one chamber design. On the other hand, some experiments find it beneficial to use three or more chambers. Such an experiment might have one chamber that is used as an atomic source oven, another which collects a beam of atoms into a MOT, and a third chamber that atoms are transported to which provides wide open optical access for trapping and imaging beams. The increased optical access can be sufficiently valuable in these experiments to warrant the extra effort required to engineer and build a more complex vacuum and transport system.

Choosing between these different options is very dependent on the atom and physics of interest. In our case, we are interested in investigating the behaviour of fermions in a lattice. Confining ourselves to the alkali atoms, this immediately limits our choice of atom to the two stable fermions  $^{40}\text{K}$  and  $^6\text{Li}$ . Because  $^{40}\text{K}$  is much heavier than  $^6\text{Li}$ , it is well suited for lattice physics because the relevant energy scale, the recoil energy  $E_{\text{R}}$ , is much smaller. A smaller recoil energy means that  $^{40}\text{K}$  is not “kicked” around as much by the light, something we wish to avoid. Having narrowed the choice of atom to  $^{40}\text{K}$ , we must now find a way to produce it. Unfortunately for us,  $^{40}\text{K}$  has a very low natural abundance; only 0.01% of all K isotopes are  $^{40}\text{K}$ . This fact makes an oven source + Zeeman slower design for  $^{40}\text{K}$  unattractive given that ovens consume quite a bit of material during operation. Instead, we opted for a vapour cell MOT design using  $^{40}\text{K}$ -enriched potassium dispenser sources.  $^{40}\text{K}$  atomic vapour is created by heating a dispenser containing Ca and KCl salts enriched with  $^{40}\text{K}$ , producing  $^{40}\text{K}$  according to the reaction [72]:



In opting for a vapour cell MOT over a 2D MOT + MOT, we sacrifice the number of atoms able to be captured during the laser cooling process. This is due to the fact that vapour cell MOTs produce additional “dirty” background gas during dispenser operation. This background gas can collide with atoms in the MOT, knocking them out of the trap at a rate  $\Gamma_{\text{bg}}$ . The rate equation that describes the number of atoms collected into a MOT is:

$$\dot{N} = A - \Gamma_{\text{bg}}N \quad (2.2)$$

where  $A$  is the MOT loading rate which is proportional to the partial pressure of the atom of interest. Equation 2.2 has the steady-state solution  $N = A/\Gamma_{\text{bg}}$ .

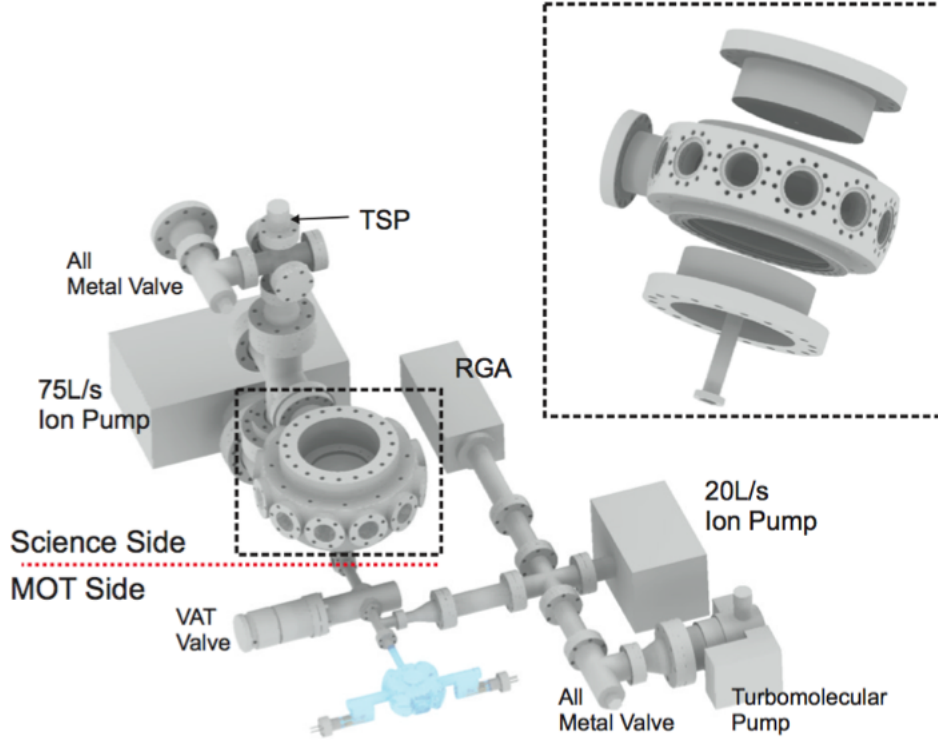


**Figure 2.6: Vacuum system** Image courtesy of Dave McKay [1].

A low MOT number can be catastrophic for a cold atoms experiment as the efficacy of the evaporative cooling stage requires that we be able to throw away hot atoms in order that the rest may thermalize to a lower temperature. We are able to circumvent this problem by simultaneously cooling  $^{87}\text{Rb}$  alongside  $^{40}\text{K}$ .  $^{87}\text{Rb}$  is the most common atom in use in cold atoms experiments around the world owing to its relatively large (28%) natural abundance, as well as its good laser cooling and collisional properties.  $^{87}\text{Rb}$  atomic vapour can be readily produced from commercial dispensers - ours are purchased from SAES. We are able to produce large  $^{87}\text{Rb}$  MOTs of a few billion atoms in our vapour cell MOT, a number that is more than sufficient to evaporatively cool both  $^{87}\text{Rb}$  and  $^{40}\text{K}$ .

A peculiar feature of our vacuum system is that we transport atoms not only *horizontally*, from one chamber to the other, but *vertically* as well. Why do this? After all, having two transport directions would seem (correctly, as it turns out) to involve a greater engineering and construction effort. The payoff is greater optical access. All the optics required for probing and manipulating atoms are allowed to rest on a second optical board, 50 cm above all the optics required for the MOT. Having this definite separation defines a “be careful around here!” space for the finely aligned science chamber beams. Perhaps most importantly, vertically transporting the atoms simplified the design of the science chamber and high-resolution imaging system by

moving the atoms along an axis of symmetry.

One of the costs of implementing our vertical transport design was that the vertical transport coils had to be incorporated into the vacuum *before* the bake. That is, because the vertical transport vacuum nipple must go *through* the coils, there is no way to remove the coils without disassembling the vacuum system. Not only did this fact make baking and assembling this part of the vacuum system especially challenging, but it requires that the vacuum system be opened to air should any damaged vertical transport coil need to be replaced.

### 2.3.1 Overcoming vacuum problems

As presented above, it might seem as if design and construction of the vacuum system advanced smoothly, with constantly increasing progress. In fact, our vacuum system was assembled and baked over a half-dozen different times. Sometimes this had to be done to repair or replace leaks suffered during the baking process. For example, we had to replace the imaging window + sub-flange assembly (pictured in Figure 6.5) due to a leak found in the sapphire-to-titanium brazed connection. A leak in a science chamber port window, however, was able to be patched up with a liberal application of VacSeal vacuum sealant.

Much tougher to diagnose were problems in producing enough  $^{40}\text{K}$  vapour to magneto-optically trap. As mentioned above, producing a ready supply of  $^{40}\text{K}$  is a tough charge. Initial attempts at a  $^{40}\text{K}$  MOT that used home-made Ca + KCl dispensers in a steel MOT chamber resulted in a low MOT atom number - of order  $10^6$  atoms. At this stage in the experiment, we were hoping to implement an all- $^{40}\text{K}$  evaporative cooling procedure, and so this atom number was clearly not sufficient. The next solution was to move to a commercially purchased  $^{40}\text{K}$ -enriched dispenser from Alvatec Alkali Vacuum Technologies. This increased the atom number to a few  $10^7$ , but still far below the number required.

A decision was then made to switch MOT chamber design, from a large steel chamber to a small glass cell, in order to limit the suspected adsorption of alkalis onto the metal surface of the vacuum chamber. This decision came with a consequence - we would not be able to attach the dispensers to leads in the vacuum chamber ourselves, but would instead rely on the glass-blower who was constructing the glass cell to perform this “ship-in-a-bottle” procedure. Unfortunately, a miscommunication between Alvatec and the glass blower resulted in the dispensers becoming too hot during this attachment process, reaching temperatures above the  $156^\circ\text{C}$  melting temperature of the indium seal that protects the K from water vapour. It took many months to diagnose the resulting poor performance of  $^{40}\text{K}$  dispensers as being due to partial water contamination.

The following MOT cell design incorporated back-up  $^{87}\text{Rb}$  dispensers for coolant in case

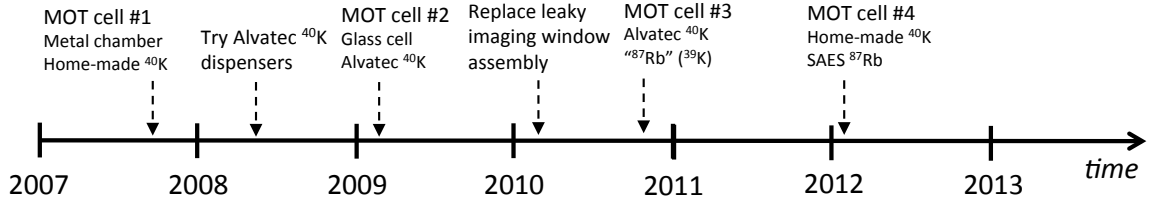


Figure 2.7: Timeline of notable vacuum bakes

the Alvatec  $^{40}\text{K}$  dispensers under-performed. And unfortunately, they did. We were only able to achieve MOT sizes of a few  $10^8$   $^{40}\text{K}$  atoms, an insufficient number for evaporative cooling. Furthermore, the dispensers outgassed a black and yellow residue that stained the dispenser region of the MOT cell. More bad news occurred when, after a few more months of effort in which a new  $^{87}\text{Rb}$  laser system was constructed and tested, we could not produce an  $^{87}\text{Rb}$  MOT with any more than  $10^6$  atoms. We soon learned, to our dismay, that our " $^{87}\text{Rb}$ " dispensers were in fact  $^{87}\text{Rb}$ -contaminated  $^{39}\text{K}$  dispensers. We had fallen victim to another miscommunication, whether the fault of the Rb dispenser vendor, the glass-blower, or ourselves.

It was not until January 2012, over 4 years into my doctoral work, that we conducted the final vacuum bake. The new MOT cell, our fourth, included both home-made  $^{40}\text{K}$  dispensers (courtesy of Graham Edge) and commercially purchased  $^{87}\text{Rb}$  dispensers. The vacuum system has performed very well ever since (knock on wood).

### 2.3.2 Vacuum system details

A rendered image of the vacuum system is shown in Figure 2.6. The MOT chamber is a custom design manufactured by Technical Glass. It features two CF flanges from which dispensers can be attached and removed. The science cell is a 12-port custom stainless steel design manufactured by Kimball Physics.

The MOT chamber is pumped with a 20 L/s ion pump. Magnetically trapped atoms have a lifetime of a few seconds in this chamber when the dispensers are running. The science cell is pumped with a 75 L/s ion pump and a Titanium sublimation pump, producing a pressure below  $10^{-12}$  Torr and an atomic lifetime of over two minutes.

A 365-mm-long horizontal tube with a minimum diameter of 0.43" joins at a right angle with a 174-mm-long 0.6" diameter vertical tube to form the transport section of the vacuum system. The tube has a vacuum conductance of approximately 1 L/s for  $\text{H}_2\text{O}$  and  $\text{H}_2$  and there is an all-metal gate valve (VAT 48124-CE01) that allows the chambers to be isolated from each other when closed. This allows the two chambers to be baked separately, for instance, allowing

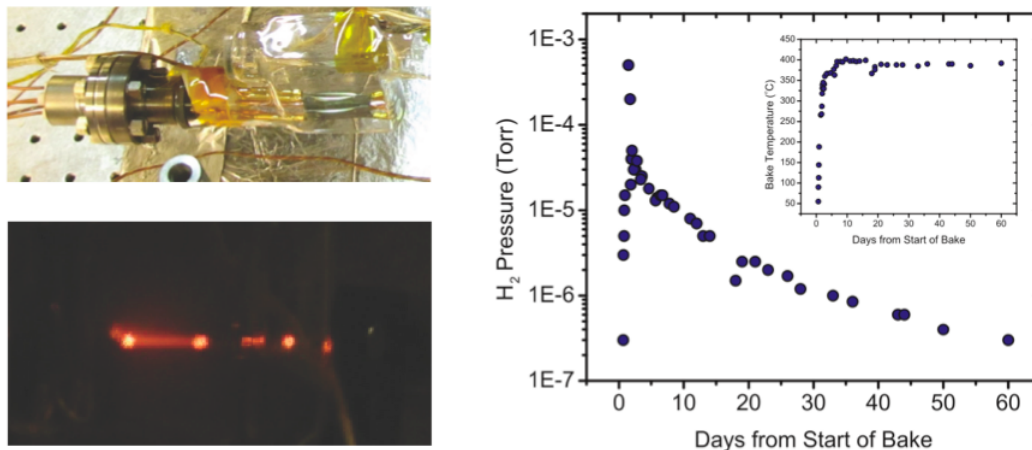


**Figure 2.8: Vacuum bake** Top left:  $^{40}\text{K}$  dispensers mounted in arm of MOT cell. Bottom left: fluorescence from resonant light during successful dispenser testing and outgassing. With  $^{40}\text{K}$  dispensers that produced large MOTs we were able to observe fluorescence with the naked eye when shining in  $\sim 200\text{mW}$  of resonant light. We did not observe fluorescence with poorly performing dispensers, however. Right:  $\text{H}_2$  pressure as a function of all-metal vacuum bake time (Image courtesy of Dave McKay [1]).

for the replacement of dispensers without disturbing the ultra-high vacuum in the science cell.

### 2.3.3 Vacuum clean and bake

Vacuum components must be cleaned and baked before use. The cleaning process (Alconox detergent, acetone, methanol, distilled water, air dry) rids the components of any residual oil resulting from manufacturing or handling. The baking process removes gas from the system, especially  $\text{H}_2$  and  $\text{H}_2\text{O}$ .

We employed a three-stage bake process for the metal components of our vacuum system. In the first stage, the components were assembled and heated to  $400^\circ\text{C}$  while being pumped with a  $60\text{ L/s}$  turbo pump (Pfeiffer TC-600) for 60 days. The goal of this stage was to pump  $\text{H}_2$  away from not just the surface, but the bulk of the metal components. A plot showing how the  $\text{H}_2$  partial pressure decreased with bake time is shown in Figure 2.8. The second bake stage was an airbake where components were heated to  $400^\circ\text{C}$  for a few days at atmospheric pressure in order to produce an oxide layer at the surface that would seal any remaining  $\text{H}_2$  into the bulk. The final bake stage involved assembling all components of the vacuum system (metal, glass, dispensers, valves, pumps, residual gas analyzer (RGA), and other) and heating the system to the maximum possible temperatures, constrained by glass-to-metal connections, dispenser activation temperatures, and the desire for small temperature gradients across the system. This meant a temperature of  $130^\circ\text{C}$  for the glass MOT cell and  $200^\circ\text{C}$  for the science

cell.

The final bake stage proceeded in three parts: a 3-day bake to pump away  $\text{H}_2\text{O}$ , a cool-down of the system in order to test-fire and clean dispensers, followed by another week of baking at temperature. The temperature was never changed by more than  $10^\circ\text{C}$  per hour. Figure 2.8 shows fluorescence from the home-made  $^{40}\text{K}$  dispensers, indicating that we have a robust source of atoms. An RGA analysis of the gases detected during dispenser out-gassing can be seen in Dave McKay’s thesis [1].

## 2.4 D2 Laser cooling

### 2.4.1 MOT

We capture and cool  $^{40}\text{K}$  and  $^{87}\text{Rb}$  atoms from a room-temperature vapour into a retro-reflected magneto-optical trap. We run both the  $^{40}\text{K}$  and  $^{87}\text{Rb}$  dispensers continuously at low currents (2.2A for  $^{87}\text{Rb}$  and 5.25A for  $^{40}\text{K}$ ) to produce a steady supply of atoms. The windows of the MOT cell are heated to  $45^\circ\text{C}$ , and the dispenser arms of the MOT cell to  $55^\circ\text{C}$ , by passing current through thin counter-wound magnetic wire in order to prevent adsorption and increase  $^{87}\text{Rb}$  and  $^{40}\text{K}$  vapour pressure.

Atoms are cooled using light that is red-detuned from the D2  $F = F_{\text{max}} \rightarrow F' = F_{\text{max}} + 1$  cycling transition. A second beam resonant with the  $F = F_{\text{max}} - 1 \rightarrow F' = F_{\text{max}}$  transition is also present to “repump” atoms that have been off-resonantly coupled into the  $F = F_{\text{max}} - 1$  state by the cooling beam. See Figure 2.9 for a  $^{87}\text{Rb}$  and  $^{40}\text{K}$  D2 level diagram and relevant optical beams. A schematic illustrating how frequency stabilized  $^{87}\text{Rb}$  and  $^{40}\text{K}$  light is amplified and shifted in frequency is presented in Figure 2.5 and Figure 2.3.

In our experiment, a typical MOT operates with 275 mW of  $^{87}\text{Rb}$  trap light and 10 mW of  $^{87}\text{Rb}$  repump light; 200 mW of  $^{40}\text{K}$  trap light and 100 mW of  $^{40}\text{K}$  repump light. This power is spread among three, 4-cm diameter, retro-reflected beams.  $^{87}\text{Rb}$  and  $^{40}\text{K}$  light is combined on a polarizing beam splitter. The polarization of the  $^{40}\text{K}$  light is aligned to the polarization of the  $^{87}\text{Rb}$  light using a 27-order waveplate (Lensoptics) that has  $\lambda/2$  retardance for 767 nm and  $\lambda$  retardance for 780 nm. Trap and repump light are combined on a non-polarizing beam splitter so that both may have the proper “cooling” polarizations in the 10 G/cm magnetic gradient. The  $^{87}\text{Rb}$  and  $^{40}\text{K}$  trap light is detuned by -30 MHz. The  $^{40}\text{K}$  repump light is detuned by -20 MHz in order to help with trapping, whereas the  $^{87}\text{Rb}$  repump light is tuned to resonance. We simultaneously collect  $3 \times 10^9$   $^{87}\text{Rb}$  and  $1 \times 10^8$   $^{40}\text{K}$  atoms at 200  $\mu\text{K}$ , a typical number for these atoms. Figure 2.11 shows the effect that the presence of  $^{87}\text{Rb}$  has on the  $^{40}\text{K}$  MOT number.

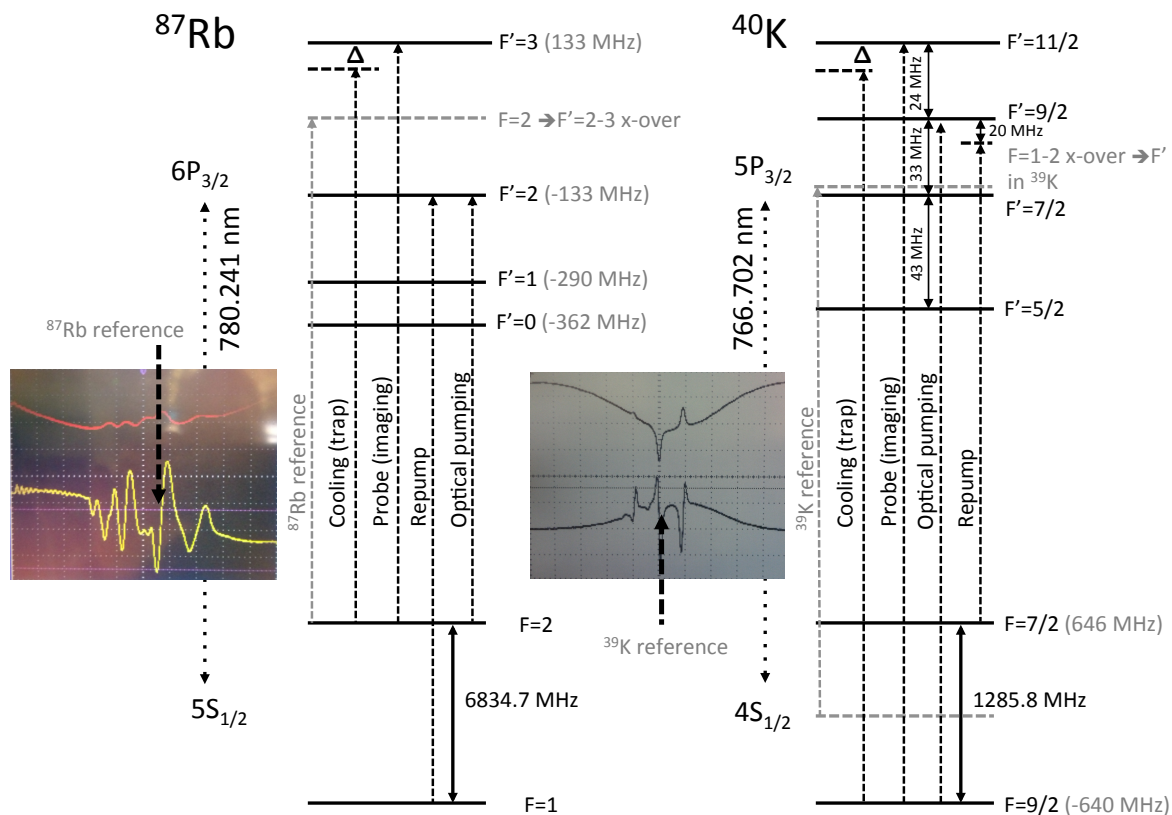


**Figure 2.9:**  $^{87}\text{Rb}$  and  $^{40}\text{K}$  D2 level diagram The optical beams used for laser cooling, optical pumping and imaging  $^{87}\text{Rb}$  and  $^{40}\text{K}$  atoms. Upper oscilloscope traces show the saturation spectroscopy signal, and lower traces show the error signal that the laser frequency is locked to.

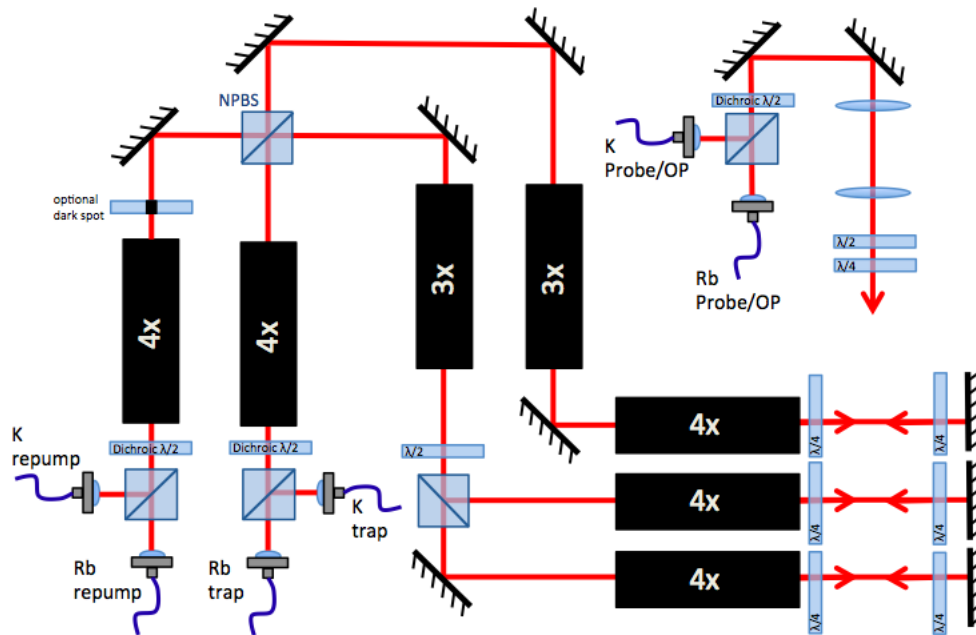


Figure 2.10: MOT optics

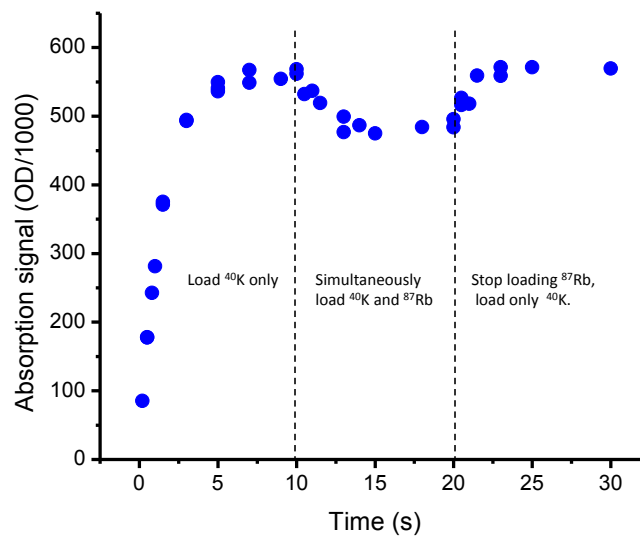


Figure 2.11: Dual  $^{87}\text{Rb}/^{40}\text{K}$  MOT

### 2.4.2 cMOT

In order to better mode-match the MOT cloud with the magnetic quadrupole trap, we employ a compressed-MOT (cMOT) stage. For  $^{87}\text{Rb}$ , the cloud is compressed by simultaneously detuning farther from resonance with the trap light, and reducing the power of the repump light. Both of these actions result in a reduction of the density-limiting radiation pressure from rescattered photons by allowing atoms to spend more time in the dark  $F = 1$  state. Our  $^{87}\text{Rb}$  cMOT stage last 30 ms, with a trap light detuning of -40 MHz and a repump power that is 20% of its MOT value. Empirically, we find that the best  $^{40}\text{K}$  cMOT parameters involve a detuning of -20 MHz and reduction of the repump power to 20% of its MOT value, similar to what was found in [73]. Note that this is a detuning *closer* to resonance. We speculate that this may be beneficial due to the fact that because  $^{40}\text{K}$  is already readily repumped to the dark  $F = 7/2$  state, it benefits more from the stiffer effective spring constant of the cMOT that detuning closer to resonance provides, rather than a further reduction in scattering. Our  $^{40}\text{K}$  cMOT stage lasts 20 ms and the magnetic gradient remains unchanged from that of the MOT.

### 2.4.3 Optical molasses

We significantly lower the temperature of  $^{87}\text{Rb}$  atoms by momentarily switching off the magnetic quadrupole field and allowing atoms time to be cooled in an optical molasses. We find that a optical molasses cooling stage is also beneficial for  $^{40}\text{K}$  when measuring the number and temperature after evaporative cooling, though we cannot measure a discernible change immediately after the MOT. Our optical molasses cooling stage lasts 10 ms for both  $^{87}\text{Rb}$  and  $^{40}\text{K}$ , with the same powers used as in the cMOT, and trap detunings of -20 MHz and -15 MHz, respectively.

### 2.4.4 Optical pumping

Atoms must have  $m_F g_F > 0$  to be magnetically trapped. Optical pumping is used to collect atoms in a single ground-state sublevel [74, 75]. For instance, by scattering light that is circularly polarized along the local field direction, atoms increase their magnetic quantum number  $m_F$  by one during an average scattering event. Optical pumping is a quick process that requires only 200  $\mu\text{s}$  of our experimental cycle time.

We optically pump using light that is resonant with the  $F = 2 \rightarrow F' = 2$  transition in  $^{87}\text{Rb}$ , and  $F = 9/2 \rightarrow F' = 9/2$  in  $^{40}\text{K}$ . This choice ensures that once atoms have been pumped to the  $m_F = F$  “stretched” state, they become transparent to the optical pumping light and do not heat.

The experimental cycle is very sensitive to the efficiency of the optical pumping stage. If atoms are not well polarized in the stretched state, they are not as tightly magnetically trapped. This leads to a reduced magnetic transport efficiency through the small diameter sections of the differential pumping tube. Moreover, loose confinement from poor atomic polarization leads to a much reduced evaporation efficiency due to the associated reduction in collision rate. Practically speaking, an anomalous drop in atom number after evaporation can often be traced to a misaligned or blocked optical pumping beam.

### 2.4.5 Laser cooling alignment

The MOT is aligned in a series of steps that seek to isolate the individual trapping effects of beam power, alignment, magnetic gradient, and “shim” magnetic bias fields. The main constraint is that the MOT must be aligned to the centre of the quadrupole magnetic field so that the magnetic trapping stage is able to maintain the phase-space density of the MOT. The first alignment step is to coarsely align the beams to the mechanical centre of the MOT cell. The quadrupole centre is then identified by imaging the fluorescence of magneto-optically trapped atoms on two orthogonally oriented cameras in a strong (50 G/cm) magnetic gradient. Once identified, the shim bias coils are adjusted in order to align the fluorescence of trapped atoms to the quadrupole centre in a very weak (2 G/cm) gradient.

The MOT alignment procedure is inherently iterative as the magneto and optical effects can never be fully decoupled. Optical alignment is fine-tuned by centering irises on the beams and maximizing the fluorescence signal at the quadrupole trap centre with progressively smaller and smaller iris apertures. The cancellation of stray magnetic fields can be fine-tuned by looking at the expansion of the cloud in an optical molasses. The quadrupole field is turned off during optical molasses, making this alignment step dependent only on beam powers and polarization (both easily measured without atoms), and any remnant magnetic fields. The shim bias fields are adjusted to optimize the isotropy and expansion time of the cloud in the light field. When the magnetic field is properly cancelled, the fluorescence from  $^{87}\text{Rb}$  atoms can be seen for many tens of seconds after shut-off of the magnetic gradient.

## 2.5 Magnetic trapping and transport

The field of a cylindrically symmetric quadrupole trap is  $\mathbf{B}(\mathbf{r}) = \beta/2\mathbf{x} + \beta/2\mathbf{y} - \beta\mathbf{z}$  [34]. As trapped atoms move through the field, their magnetic moment follows the direction of  $\mathbf{B}$  adiabatically, such that the trapping potential is  $m_{FGF}\mu_B|\mathbf{B}|$ .

Immediately after optically pumping the  $^{87}\text{Rb}$  and  $^{40}\text{K}$  atoms into the  $|2, 2\rangle$  and  $|9/2, 9/2\rangle$

states, respectively, the MOT quadrupole field is switched on to 100 G/cm in less than 2 ms. We transfer approximately 75% of the atoms without much evident heating. We immediately begin transferring the atoms to the science chamber.

The magnetic transfer scheme in use was designed by Josefine Metzkes [76] and Michael Yee [77]. Michael Yee also helped with initial assembly and characterization. It is based on the design described in [78], relying on the smooth variation of current through three quadrupole coil pairs at any one time in order to produce a moving quadrupole trap. The three currents are determined by solving a set of three independent equations:

$$\mathbf{B}(\mathbf{r}_{\text{pos}}) = 0 \quad (2.3)$$

$$\beta_z|_{\mathbf{r}_{\text{pos}}} = 100 \text{ G/cm} \quad (2.4)$$

$$\beta_x/\beta_y|_{\mathbf{r}_{\text{pos}}} = A_0. \quad (2.5)$$

The first equation makes sure that the cloud position  $\mathbf{r}_{\text{pos}}$  is at the trapping centre. The second equation sets the magnetic trapping gradient. The third equation sets the aspect ratio  $A_0$ . For the horizontal transport section, a choice of  $A_0 = 1.72$  allows the aspect ratio to remain constant throughout most of the transfer, with the exceptions occurring at the beginning of transport when atoms are transferred out of the MOT cell, and at the end of horizontal transport when atoms are transferred into the 6-way cube that joins the horizontal and vertical transport nipples: see Figure 2.14. During the vertical transport section, atoms are transported along the axial direction of the coils and so  $A_0 = 1$  due to symmetry.

The consequences of solving these three equations are that there are three independent currents through three coil pairs in the horizontal transport section, and two independent currents through four coils during the vertical section: two coils below the atoms that push, and two coils above the atoms that pull, the atoms upwards. When atoms move through a coil vertically, the coil has to switch from “pushing” to “pulling” and thus the current has to change polarity. This requires bi-polar electronics. We find that the atoms are especially sensitive to heating and loss at precisely the point where the current changes polarity. This is due to both the difficulty in managing a low-noise bi-polar transition, and the close proximity of atoms to the coils at precisely the same point, resulting in an increased amplitude of magnetic field noise seen by the atoms.

## 2.5.1 Transport hardware and electronics

### Hardware

The coils used for magnetic transport and quadrupole evaporation were designed in-house and constructed by Oswald GmbH, with the exception of the “push” coil, which was constructed by Michael Yee [77]. The coils are attached to brass cooling mounts using thermal epoxy. The brass mounts are cooled with 12°C distilled water that is cycled in a closed loop through a chiller (ThermoCube) that is cooled by the university chilled water system.

### Electronics

The electronics used for current control were built primarily by Alan Stummer, and a thorough description may be found on his website [79]. The transport system is powered by a single 30V/200A power supply (Delta SM 30-200). The current is feedback-controlled by comparing a reference voltage with the voltage from a Hall probe (FW Bell CLN-50) measuring the current. The feedback voltage is fed into the gate of a high power MOSFET (APT10M07JVFR) which is able to conduct currents up to 225A. The voltage of the power supply is set remotely and chosen to minimize the MOSFET drain-source voltage. See Figure 2.13.

While the uni-polar current control is replicated for all horizontal coil pairs, and the bi-polar current control is replicated for many of the vertical coils, the current control for coils 15 and 16 - the final two vertical coils that provide the quadrupole trap in which evaporation takes place - is non-obvious and so deserves explanation. The constraints driving the control design are that 1) coil 15 is bi-polar, 2) coil 16 is uni-polar, 3) we wish to be able to independently control the currents through both coils (though with the simplifying constraint that the current in coil 15 never exceeds that of coil 16), and 4) coils 15 and 16 are able to be run in series. The last condition ensures that current noise results only in common-mode magnetic field noise and not a shift of the trap position. This is especially important for a plugged quadrupole trap, where the trap position must be stable to within 1  $\mu\text{m}$ . The current through coils 15 ( $I_{c15}$ ) and 16 ( $I_{c16}$ ) are determined by choosing the currents through the channels  $I_{15}$ ,  $I_{16}$ , and  $I_{15/16}$ , and the switch  $I_{15\text{sw}}$ :

$$I_{c15} = \begin{cases} I_{15}; (I_{15\text{sw}} = \text{open}, I_{15/16} = \text{short circuit}, I_{16} = \text{open}) & : I_{c15} < 0 \\ I_{16} - I_{15/16}; (I_{15} = \text{open}, I_{15\text{sw}} = \text{short circuit}) & : I_{c15} > 0 \end{cases}$$

$$I_{c16} = I_{16}.$$

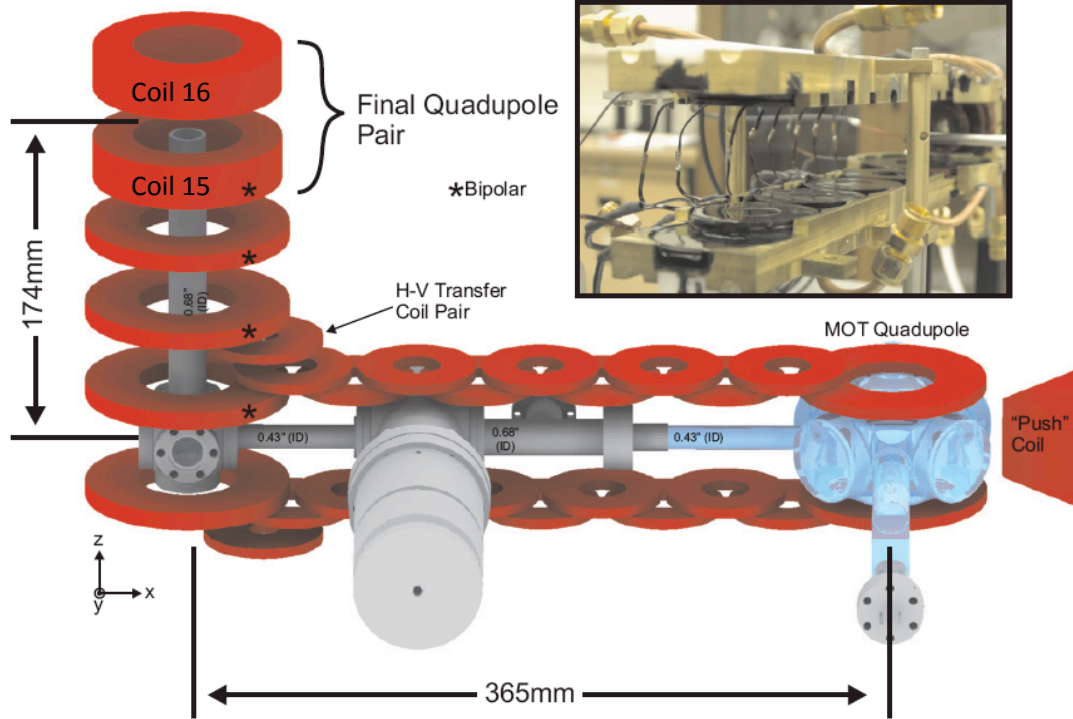


Figure 2.12: Magnetic transport coils Image courtesy of Dave McKay [1].

### Notable modifications

There are a few notable modifications to the design described in [79]. An additional coil pair has been added to the end of the horizontal transport section due to the slightly longer (5 mm) differential pumping tube section of the most recent version of the glass MOT cell. The current through this “H-V transfer” coil is controlled with the same servo electronics as the first horizontal coil pair, with current directed to one or the other coil pair using a double-throw relay. We are able to do this because these two specific coil pairs are never on at the same time.

We have also implemented a fast-off for coils 15 and 16 that form the quadrupole field. A fast-off is required for precise time-of-flight measurements. For coils of inductance  $L$  with a voltage  $V$  over them, the current  $I$  changes at the rate

$$\frac{dI}{dt} = V/L. \quad (2.6)$$

For our quadrupole coils and operating voltage, it can take between 5 and 10 ms for the current

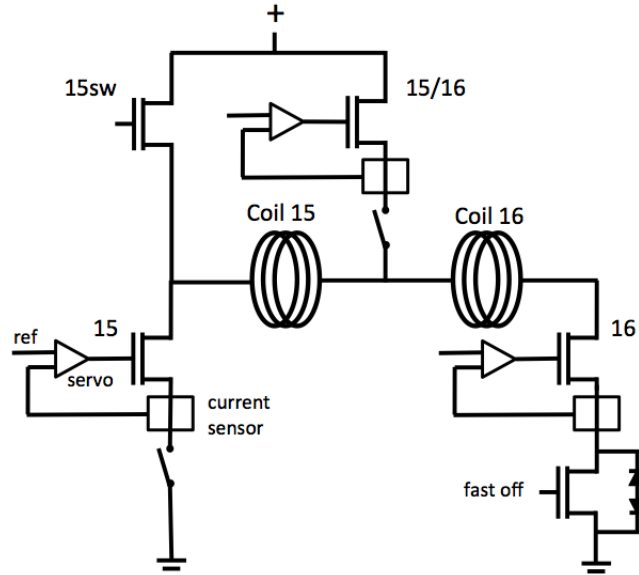


Figure 2.13: Quadrupole coil circuit

to shut off. This is comparable with time-of-flight times, and therefore not quick enough for our purposes. By adding an additional high-power MOSFET with a 56V TVS across it, the current is able to be shut-off in less than  $100 \mu\text{s}$ .

Relays have also been added in order to hard shut off  $I_{15}$  and  $I_{15/16}$  when the coils are being run in series.

### 2.5.2 Trouble-shooting and optimizing transport

The magnetic transport system operates very reliably once optimized and is able to transport 20% of the atoms collected in the MOT to the science chamber. However, getting the transport system optimized in the first place is no small feat. Here we detail some of the techniques and procedures that have been helpful.

The first thing to check when trouble-shooting the transport system is that the measured currents correspond to the set currents. The currents are plotted in Figure 2.14. While the absolute current may be checked with a current probe, many standard probes have bandwidths limited to 10 kHz and so are not able to detect higher frequency noise that atoms are sensitive to. In order to detect this noise, the voltage over the coils, as well as the gate voltage on the high-power MOSFETs, should be checked. Much of this noise can be avoided with proper choice of the capacitance and resistance of the PID feedback circuit. We have also noticed that voltage noise on the current supply leads to atom loss. This noise can be suppressed by dynamically choosing the voltage to match the overall power consumption of the transport system.

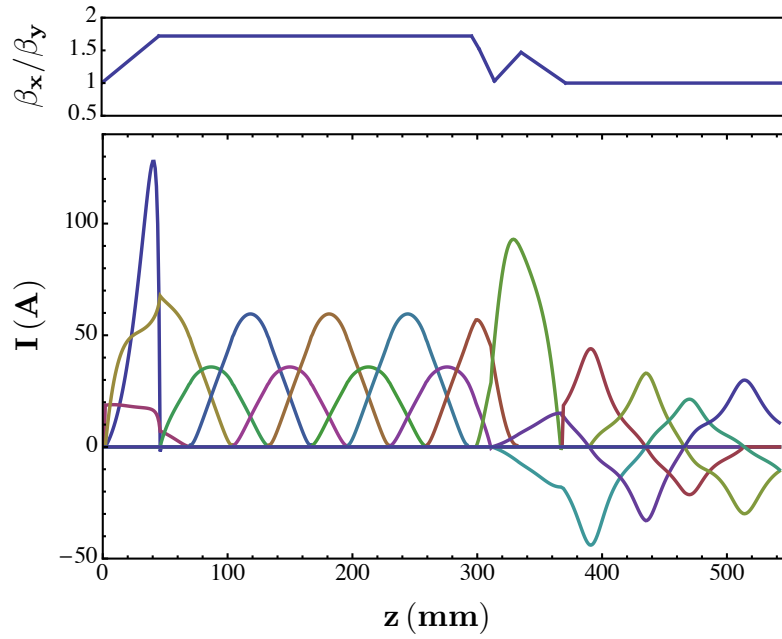


Figure 2.14: Magnetic transport currents

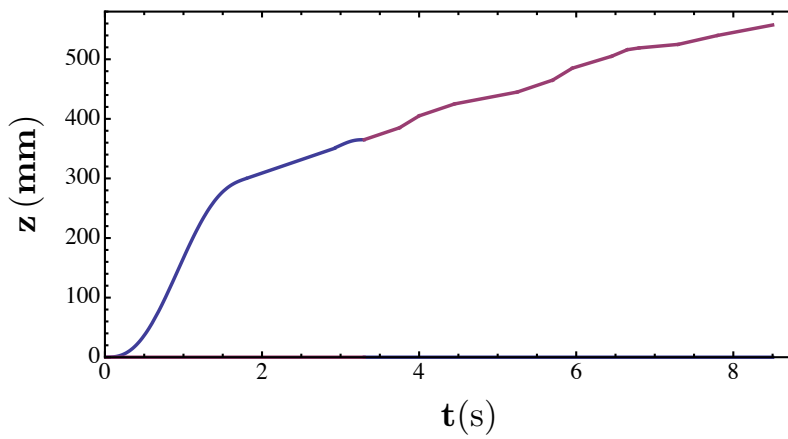


Figure 2.15: Magnetic transport timing

When testing the transport system with atoms, different sections of the transport system can be isolated by transporting the atoms some distance, and then back to the MOT cell. If a trouble section is identified, possible remedies such as changing the velocity, cloud aspect ratio, current amplitude, translating the point at which the current turns on and off, identifying and suppressing electrical noise, etc. can be attempted. In particular, the final number and temperature of the atoms transported to the science chamber is very sensitive to the rate and acceleration with which the cloud is transported. Clearly, we would like the transport to be as smooth as possible, with minimal jerk  $j = d^3x(t)/dt^3$ . Mathematically, then, we are searching for a solution for the distance as a function of time  $x(t)$  that minimizes the magnitude of the jerk between the start time  $t = 0$ , and the end time  $t = t'$ . Thus, we want to minimize:

$$\int_0^{t'} \left( \frac{d^3x}{dt^3} \right)^2 dt. \quad (2.7)$$

For the appropriate initial and final conditions ( $\dot{x}(0) = \ddot{x}(0) = 0$  and  $\dot{x}(t') = \ddot{x}(t') = 0$ ), the solution that minimizes Equation 2.7 is:

$$x(t) = x_i + (x_f - x_i) \left( 10 \left( \frac{t}{t'} \right)^3 - 15 \left( \frac{t}{t'} \right)^4 + 6 \left( \frac{t}{t'} \right)^5 \right) \quad (2.8)$$

where  $x_i$  is the starting point and  $x_f$  is the final point. In the experiment, atoms are horizontally transported 365 mm in 3.3 s using a minimum jerk distance versus time function that includes a constant velocity section - which, of course, is “jerk-free” - during the final few millimetres when the cloud aspect ratio is changing rapidly. Atoms are vertically transported 174 mm using a piecewise linear distance versus time function. This function is helpful in navigating through the sensitive polarity-switching regions by slowing down the transport every time the atoms pass through a coil. While in principle a piecewise linear curve should contain regions with infinite jerk, in practice the coils filter and smooth this motion out. We find that the empirically optimized piecewise linear curve far outperforms any other distance versus time function during the vertical transport section, minimum jerk or otherwise. See Figure 2.15 for the combined horizontal + vertical distance versus time function.

A final note about transport system alignment. The magnetic transport is not mechanically constrained by, or attached to, the vacuum system. It is aligned first by eye, then by imaging the *in situ* cloud position using a probe beam propagating through either the horizontal or vertical pumping tube. Final alignment is determined by maximizing the number of atoms that are transported to the science chamber.

## 2.6 RF evaporative cooling

In a successful evaporative cooling, temperature decreases with atom number as  $T \propto N^\alpha$ , where  $\alpha$  characterizes the evaporation efficiency. For instance, for  $\alpha = 1$ , the temperature is reduced by a factor of ten for each factor of ten reduction in atom number. Such a scaling would mean that at least  $10^8$  atoms are needed after laser cooling (at approximately  $100 \mu\text{K}$ ), if one would like to have  $10^5$  atoms left at quantum degenerate temperatures (on the order of  $100 \text{nK}$ ). In this section, Section 2.7 and Section 2.8, we discuss evaporatively cooling in a quadrupole, plugged quadrupole, and crossed-dipole trap, respectively.

As the ensemble cools, cloud size decreases as  $T^p$  in a D-dimensional trapping potential whose strength is proportional  $r^{D/p}$ , where  $r$  is the distance from the trap minimum [65]. This could increase the density and thus the collision rate  $\gamma = n\sigma v_T$ , however atom number decreases during evaporation, and  $v_T$  decreases at lower temperature. These three combined effects produce an increasing collision rate for a sufficiently efficient evaporation, such that  $\alpha(p - 1/2) > 1$  [31]. This *runaway evaporation* condition is typically a prerequisite for a successful quantum gas experiment. In that case, it is the initial stages of evaporative cooling that are the slowest, motivating continued research on laser cooling techniques to achieve high density at sub-Doppler temperatures.

Buried within the efficiency  $\alpha$  are the details of the forced evaporation trajectory, losses due to background collisions, efficiency of energy removal, and the elastic collision rate. At the lowest temperatures, evaporative cooling ceases to be effective either when spatial selection no longer selects the highest energy atoms, or when heat transport is slow. Both of these issues are encountered in optical lattices, for which alternative cooling approaches have been proposed. [80, 81, 82]

The highest-energy atoms will reach the largest magnetic fields during their trajectory, and those that can roll over the maximum potential leave the trap. Evaporation is forced with a RF field that couples trapped  $g_F m_F > 0$  states to untrapped  $g_F m_{F'} < 0$  states.

### Antenna and sources

An RF magnetic field is generated from a direct digital synthesizer (DDS) constructed by Alan Stummer [79]. The field is transmitted to the atoms using thin wire (30 AWG tinned Cu) that forms 3/4 of a 4 mm diameter loop. It is important that the antenna wire have line-of-sight to the atoms through the sapphire imaging window. If not, the Rabi rate all but vanishes for both RF (tens of MHz) and  $\mu$ -wave (few GHz) frequencies. It is also important that the antenna be as flat as possible in order for the imaging objective to be positioned a focal distance (2.43 mm) away from the atoms. The antenna should also obscure as little of the window as

possible. Figure 2.16 shows a picture of the antenna properly positioned over the sapphire imaging window.

We use the same antenna to transmit RF and  $\mu$ -wave frequencies to the atoms. Because RF and  $\mu$ -wave fields are not used simultaneously in our experiment, we are able to connect one or the other to the antenna using a transfer switch (Mini-circuits MTS-18-12B+). We stub-tune the antenna for 6.8 GHz *ex situ* by optimizing the field coupled to a nearby pick-up coil.

### Two-stage evaporation

We force evaporation on a cloud of approximately  $5 \times 10^8$   $^{87}\text{Rb}$  atoms at a few hundred  $\mu\text{K}$  in the science chamber. A cloud of  $5 \times 10^7$   $^{40}\text{K}$  atoms is sympathetically cooled by  $^{87}\text{Rb}$ . Sympathetic cooling of  $^{40}\text{K}$  by  $^{87}\text{Rb}$  is possible because the Landé g-factor of  $^{87}\text{Rb}$  in  $|2, 2\rangle$  is larger than that of  $^{40}\text{K}$  in  $|9/2, 9/2\rangle$ :  $g_2 = 1/2 > g_{9/2} = 2/9$ . Consequently,  $^{87}\text{Rb}$  atoms in the quadrupole trap that are resonant with a given RF frequency will be a factor of  $g_2/g_{9/2} = 9/4$  hotter than the  $^{40}\text{K}$  atoms resonant with the same field. Assuming we have thermal equilibrium between the two species, this results in a method to selectively remove  $^{87}\text{Rb}$  without affecting  $^{40}\text{K}$ .

We evaporatively cool in two locations in the science chamber. The first stage of cooling occurs 7.4 mm away from the imaging window in order to prevent atoms in the large, hot cloud from being lost due to contact with a nearby surface. In a 230 G/cm quadrupole field we apply a 45 MHz Rf knife and slowly sweep the frequency to 12 MHz in 25 s. Once atoms have been cooled below 140  $\mu\text{K}$ , they are transported to the imaging position 800  $\mu\text{m}$  away from the surface of the imaging window. RF evaporation is finished in a quadrupole trap that is “plugged” with a blue-detuned optical beam. Figure 2.17 shows the atoms in different stages of transport between the two evaporation positions.

## 2.7 Plugged quadrupole trap

### 2.7.1 Majorana loss

Evaporation in a quadrupole magnetic field occurs efficiently compared with a Ioffe-Pritchard [83] or TOP [84] trap owing to the linear trapping potential. However, at the center of a quadrupole trap, the magnetic field vanishes and atoms are no longer able to adiabatically follow the field direction, becoming lost from the trap. This *Majorana* loss is extremely detrimental to evaporative cooling as it disproportionately affects the atoms that spend most of their time near the trap centre, i.e. the coldest atoms. In the following, we outline a simple model for Majorana loss first articulated in [84], and then extend it to account for depolarization, which is important for large  $F$  atoms.

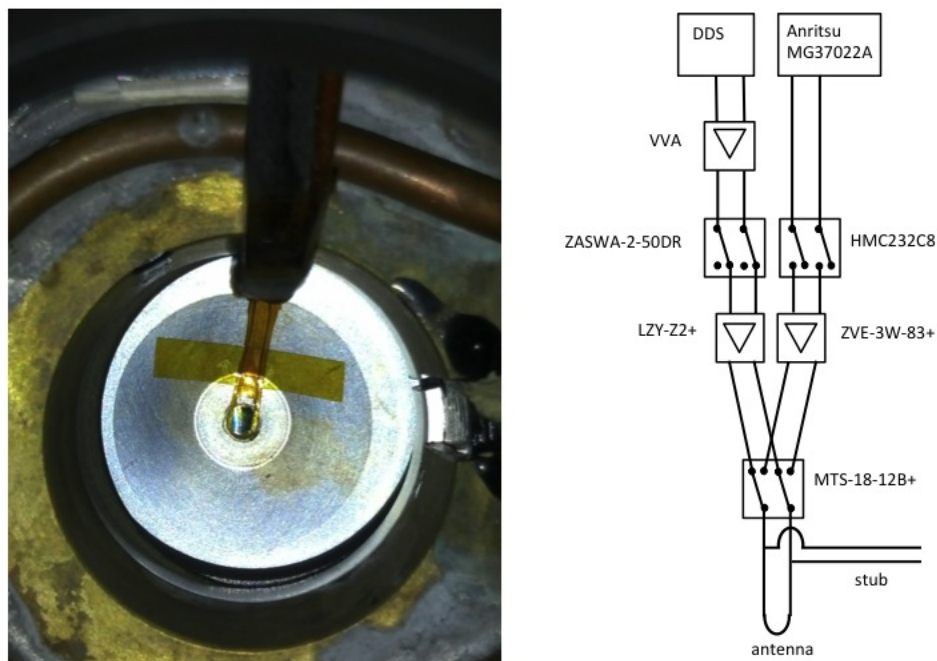


**Figure 2.16: RF and  $\mu$ wave antenna** Left: Antenna positioned over imaging window. The brass quadrupole coil cooling mounts can also be seen. Right: Schematic detailing how RF and  $\mu$ -wave frequencies are coupled into the antenna. The amplitude of the RF signal is controlled with a voltage-variable attenuator (VVA) and switched on and off with a Mini-Circuits ZASWA-2-50DR switch. The RF signal is then amplified by a 30W amplifier (Mini-Circuits LZY-Z2). The  $\mu$ -wave signal is switched with a Hittite HMC232C8 switch and amplified by a 3W amplifier (Mini-Circuits ZVE-3W-83). The stub is made from co-axial cable and an SMA tee connector.

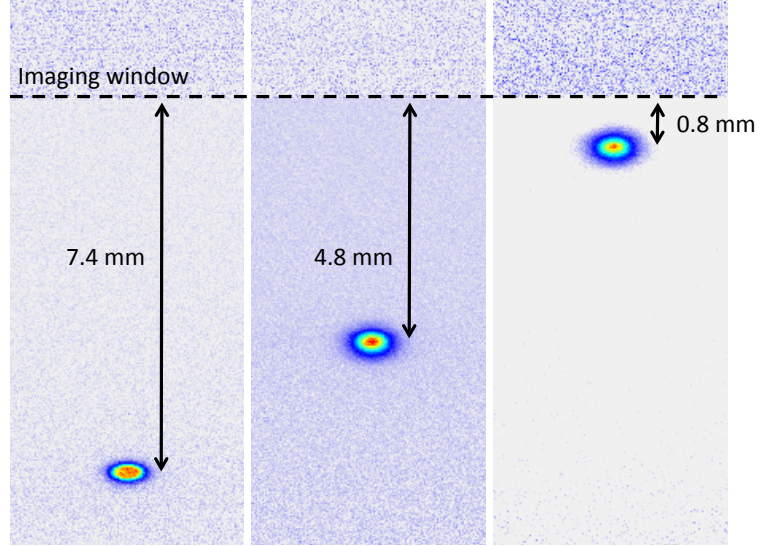


**Figure 2.17: Transporting atoms to imaging location** Left: *In situ* image of atoms at  $140\ \mu\text{K}$  at the first RF evaporation location. Middle: Atoms mid-way during transport between evaporation locations. Right: Atoms at  $100\ \mu\text{K}$  at the imaging, and second evaporation, location.

Assume that we have an atom travelling with some velocity  $v$  near the centre of a quadrupole magnetic trap with a distance of closest approach  $b_0$ . The atom is able to adiabatically follow the change in magnetic field direction so long as the rate of change  $v/b_0$  is less than the Larmor frequency  $\omega_F = \mu B' b_0 / \hbar$ . We can write this condition as an inequality:

$$\frac{\mu B' b_0^2}{\hbar v} > 1 \quad (2.9)$$

We can define a loss rate per atom  $\Gamma_M$  as equal to the flux of particles lost through the ellipsoid  $b_0^2$ :

$$\Gamma_M = n b_0^2 v / N \quad (2.10)$$

where  $n = N/l^3$  is the density and  $l$  is the extent of the cloud in the quadrupole trap. We can make use of both Equation 2.9, as well as the virial theorem which connects the kinetic energy  $mv^2$  with the potential energy  $\mu B' l$ , to give:

$$\Gamma_M = \frac{\hbar}{m l^2}. \quad (2.11)$$

Then, using the equipartition theorem  $k_B T = \mu B' l$ , we can show  $\Gamma_M$  to be temperature depen-

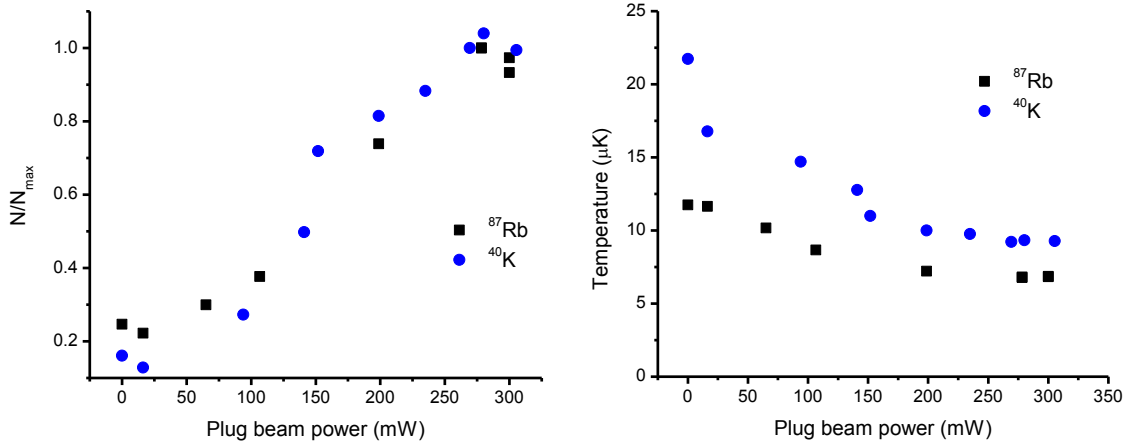


**Figure 2.18: Number and temperature dependence on plug beam power** A  $^{87}\text{Rb}$  and  $^{40}\text{K}$  cloud has been RF evaporatively cooled to  $10 \mu\text{K}$  in a plugged quadrupole trap, corresponding to a final RF frequency of  $0.8 \text{ MHz}$ . Left) The  $^{87}\text{Rb}$  and  $^{40}\text{K}$  atom number decrease in a similar fashion for plug powers less than  $275 \text{ mW}$ . The atoms number at full plug beam power  $N_{\max}$  is  $3 \times 10^6$  for  $^{87}\text{Rb}$  and  $3 \times 10^5$  for  $^{40}\text{K}$ . Right) The temperature increases with decreasing plug power. However, the temperature increase is more severe for  $^{40}\text{K}$  due to its larger angular momentum  $F$ .

dent:

$$\Gamma_M = \frac{\hbar}{m} \left( \frac{\mu B'}{K_B T} \right)^2. \quad (2.12)$$

The argument thus far has assumed that when atoms pass too close to the quadrupole trap centre at too great a velocity, they are immediately lost from the trap. In fact, they are first de-polarized, which amounts to the same thing as loss for  $F = 1$  atoms. However, for atoms like  $^{40}\text{K}$  with large  $F$ , de-polarization can be just as pernicious as it happens even more quickly, resulting not only in loss but weaker confinement and poor thermalization as well. We can define a Majorana de-polarization rate  $\Gamma_{MP}$  from the stretched state  $|m_F| = F$  by modifying the inequality in Equation 2.9, replacing the 1 with  $\ln \pi \sqrt{F}$  [85]. Repeating the same arguments used to define  $\Gamma_M$ , we find:

$$\Gamma_{MP} = \frac{\hbar}{m} \left( \frac{\mu B'}{K_B T} \right)^2 \ln \pi \sqrt{F}. \quad (2.13)$$

This is the same expression as for  $\Gamma_M$  but for the inclusion of the logarithmic factor. Equation 2.13 states that de-polarization happens more quickly for atoms with larger total angular momentum  $F$ . This can be heuristically understood for  $g_F F = 1$  atoms as being due to the

increased number of partially polarized states that atoms may become de-polarized through. Consequently, we would expect  $^{40}\text{K}$  in  $|9/2, 9/2\rangle$  to de-polarize 30% more quickly than  $^{87}\text{Rb}$  in  $|2, 2\rangle$ . This is corroborated experimentally through the observation that  $^{40}\text{K}$  requires more plug beam power to be evaporatively cooled to low temperatures than does  $^{87}\text{Rb}$ .

### 2.7.2 Plugged-quadrupole evaporation

Our plug beam uses approximately 300 mW of 760 nm light that is focused to  $30\ \mu\text{m}$ . The plug beam propagates along the radial direction of the 150 G/cm quadrupole field. We use a lower magnetic gradient, compared with the first stage of evaporation, in order to protect against inelastic 3-body loss during the final stages of evaporation. A lower gradient also effectively increases the repulsive barrier from the plug beam at the magnetic trap centre. Furthermore, the lower gradient results in an adiabatic cooling of the cloud from  $140\ \mu\text{K}$  to  $100\ \mu\text{K}$  after transfer between the two evaporation locations. Consequently, this second stage of Rf evaporation begins with an Rf knife at 8 MHz, sweeping exponentially to 0.8 MHz in 5 s, resulting in a  $7\ \mu\text{K}$  cloud.

### 2.7.3 Plug beam alignment

It is helpful for alignment to be able to couple resonant light along the plug beam path. It is also helpful to have a camera imaging along an axis  $< 30^\circ$  from the plug beam propagation direction. The resonant light is useful for coarse alignment, positioned to best heat atoms of the quadrupole trap. The initial alignment stage can be reduced to a one-dimensional problem by positioning the beam far below the trap centre, keeping it on while the atoms are being magnetically transferred upwards.

Once the beam has been aligned by optimizing the loss signal with shorter and less intense light pulses, the *in situ* position of the trapped cloud is imaged and identified: see Figure 2.19a.. The resonant light is then used to excite fluorescence: see Figure 2.19b. The beam is aligned so that its image coincides with the identified *in situ* position.

At this point, the wavelength used for the plugged quadrupole trap is coupled along the beam path. If the cloud is evaporated below 2 MHz, corresponding to an energy less than the dipole potential of the plug beam, an *in situ* absorption image taken on the  $< 30^\circ$  positioned camera should be able to observe a “hole” in the cloud: see Figure 2.19c. The plug beam can be aligned so that the hole is centred, or slightly ( $10\ \mu\text{m}$ ) above, the quadrupole trap centre for reasons to do with the potential shape articulated in Section 3.5.1.

The final plug alignment is done by maximizing the number and optical density while simultaneously minimizing the width of the cloud after some fixed time-of-flight. We find that we are sensitive to mis-alignments of a few  $\mu\text{m}$ .

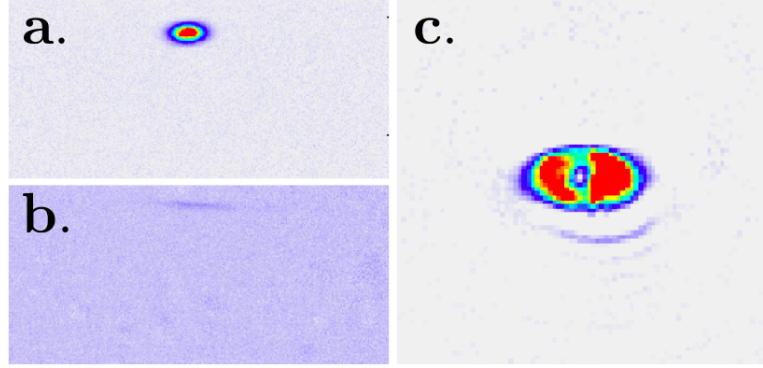


**Figure 2.19: Plug beam alignment steps** a) The position of the cloud is identified in the quadrupole trap by taking an *in situ* image. b) The fluorescence from a resonant light along the plug beam path is overlapped with the *in situ* position. c) An *in situ* image of the cloud in the plugged quadrupole is taken. The “hole” in the cloud is caused by the plug beam.

## 2.8 Optical trap

In order to produce large quantum gases and load them efficiently into the optical lattice, we find that it is best to finish evaporation in a crossed optical dipole trap. Cold clouds of  $2 \times 10^6$   $^{87}\text{Rb}$  and  $2 \times 10^5$   $^{40}\text{K}$  atoms are loaded from the plugged quadrupole trap into the crossed dipole trap using the procedure illustrated in Figure 2.20 and described below. The crossed-dipole trap is created from two elliptically-shaped beams with wavelength 1053.6 nm and horizontal and vertical waists  $(w_{h1}, w_{v1}) = (161 \mu\text{m}, 38 \mu\text{m})$  and  $(w_{h2}, w_{v2}) = (230 \mu\text{m}, 58 \mu\text{m})$ . We use elliptical beams in order to provide tight confinement against gravity. Because we are ultimately interested in 2D lattice physics, loading from an elliptical crossed dipole trap into a 3D lattice has the additional benefit of minimizing the number of atoms that we must “throw away” when preparing a single lattice plane of atoms. The dipole light is generated from a 100mW master laser (NP photonics “The Rock”) that seeds a 40 W fiber amplifier (NuFern).

### 2.8.1 Transfer from plugged-quadrupole to crossed dipole trap

Atoms are transferred from the plugged quadrupole trap to the crossed dipole in a series of intermediate step illustrated in Figure 2.20. We ramp on a single dipole beam, dipole 1, to 4.5 W during the last 3 s of plugged quadrupole evaporation in order to evaporate atoms into the dipole potential minimum. The quadrupole trap is then slowly ramped down from 150 G/cm to 12 G/cm in 500 ms, a gradient that is slightly below the levitation gradient for  $^{87}\text{Rb}$  in  $|2, 2\rangle$ . Simultaneously, the magnetic shim coils ramp to a value that keeps the plugged-quadrupole minimum stationary. The plug beam is kept on during this process in order to protect against Majorana loss and heating. Only after the quadrupole gradient has been reduced to 12 G/cm

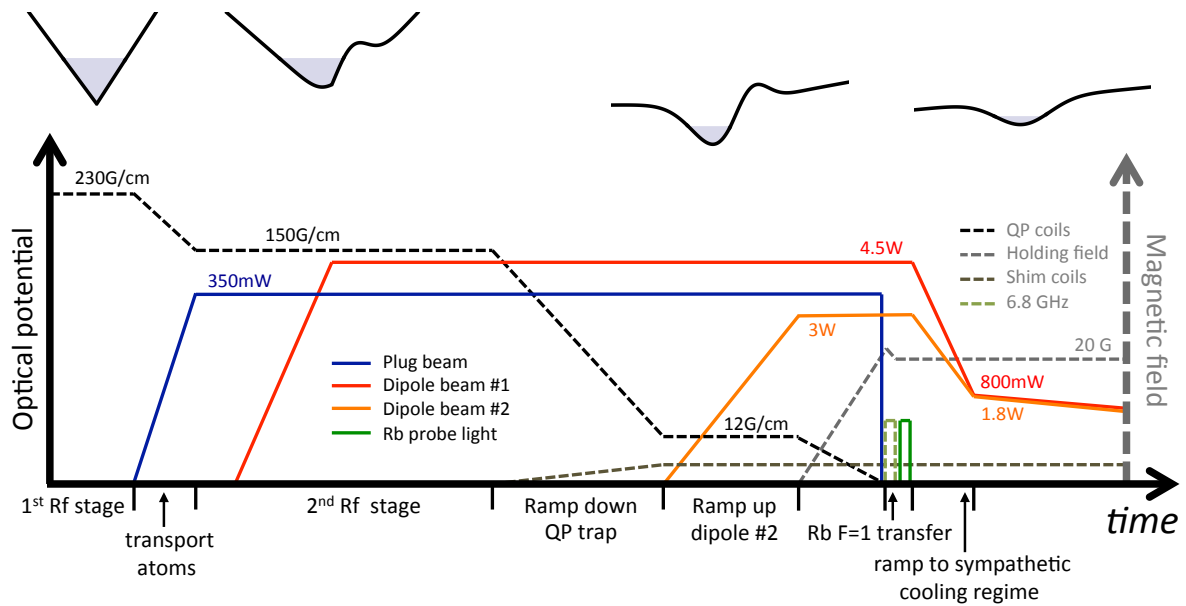


**Figure 2.20: Evaporation and transfer:** Plots above show a cross-section of the potential seen by the atoms along the vertical direction.

is the second dipole beam, dipole 2, ramped on. We have found that loading directly into a crossed dipole trap from the plugged-quadrupole trap results in a significant amount of 3-body loss due to too-tight confinement.

### 2.8.2 Magnetic field zeroing

In order to perform efficient sub-Doppler cooling in the science chamber and select a single plane of a 3D lattice using a magnetic gradient, we need to be able to cancel any stray magnetic fields using the magnetic shim coils.

The magnetic field is zeroed by varying the currents in each shim coil so that the difference between the resonant  $\mu$ -wave transition frequency and the bare hyperfine splitting  $\Delta E_{\text{HF}}/\hbar$  (see Section A.1) is minimized. After iterating through the 3 orthogonal shim coils, we determine that we have zeroed the magnetic field to better than 5 mG.

### 2.8.3 Crossed dipole trap alignment

The alignment of the crossed dipole trap is sensitive to alignment errors of a few microns, a distance equal to a fraction of the plug and dipole beam waists. Here we present the series of alignment steps used to efficiently align the crossed dipole trap in our system.

In the first alignment step, a dipole beam is turned on for the last few seconds of RF evaporation in the plugged quadrupole trap. The beam is also allowed to remain on during time-of-flight, after the plugged quadrupole trap has been turned off, and even through the absorption image. The motivation behind this method is that even if atoms do not find their way into the dipole beam during evaporation, they might after release and expansion. This broadens the target radius from  $100 \mu\text{m}$ , to 1 mm. The first alignment signal will be that time-of-flight cloud has been altered by the presence of the dipole beam - the spherical symmetry interrupted by perturbation looking like a thin pencil: see Figure 2.21. Alignment is optimized by maximizing the number of atoms trapped in this “pencil” trap. This alignment step is done individually for both beams.

We find that the best loading into the crossed dipole trap is accomplished when we first load into dipole 1, a beam almost perfectly co-linear with the plug beam. Loading into dipole 1 - versus dipole 2, or dipole 1 plus dipole 2 - seems to help due to its better spatial mode overlap with the plugged quadrupole trap. Because of this, the next alignment step involves following the loading procedure illustrated in Figure 2.20 while keeping dipole 2 off, and simultaneously maximizing the number and density of atoms in the single beam trap. Because of the elliptical dipole beam profile, we are especially sensitive to changes in the vertical alignment.

Dipole 2 can now be aligned by first maximizing the number and density of atoms transferred

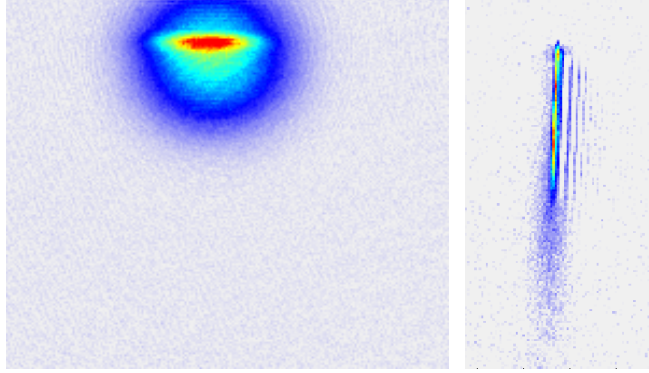


**Figure 2.21: Dipole Alignment** The image on the left shows a dipole beam having been aligned by turning it on during the last few seconds of RF evaporation, and then having it remain on during time of flight. One can notice the deformation of the cloud caused by the beam. The image on the right shows a BEC that has been allowed to fall out the bottom of the crossed dipole trap, resulting in a coherent beam of atoms. The crossed dipole trap alignment can be fine-tuned by shortening this atomic beam.

to the crossed dipole trap, again using the transfer procedure illustrated in Figure 2.20. Because a well-aligned crossed dipole trap corresponds to the deepest possible trap depth at a given optical power, fine alignment of dipole 2 can be done by maximizing the number of atoms present after crossed dipole evaporation.

A final check on the alignment of the dipole beams is done by creating an atom laser. This is done by ramping down the beam powers in 5 ms after creation of a BEC in a crossed dipole trap. The quantity to optimize in this procedure is the length - or rather, shortness - of the atom laser after some fixed time of flight: see Figure 2.21. A well-aligned crossed dipole trap will hold on to the atoms later until later times in the power ramp, producing a coherent beam of atoms with the shortest possible length.

## 2.9 From cold to ultracold

In this chapter we have described the apparatus and experimental procedures responsible for cooling a gas of  $^{87}\text{Rb}$  and  $^{40}\text{K}$  at room temperature down to a few  $\mu\text{K}$ . Though cold, this still corresponds only to a phase space density  $n\lambda_{\text{dB}}^3$  of roughly 0.01. At phase-space densities greater than 1, the gas will start to behave in fundamentally different ways. In this quantum regime, atoms are no longer able to be described by classical Maxwell-Boltzmann statistics because they are sensitive to the underlying discreteness of available states. The spin-statistics theorem [41] governs how composite boson and fermion atoms are able to occupy these states, with observable consequences for the density and momentum distributions.

In the next chapter, we develop a thermodynamic description of the transition from a

classical to *quantum* gas. We also describe the experimental procedures used to cool a gas to degeneracy in a magnetic and optical trap. Finally, we explain the measurement procedure used to identify the transition between a gas described by classical versus quantum statistics.

## Chapter 3

# Quantum Degeneracy

### 3.1 Thermodynamics of non-interacting quantum particles

A gas of cold atoms is an isolated system: atoms are held in a conservative optical or magnetic trap in a vacuum, with energy  $E$ , volume  $V$ , and atom number  $N$  fixed. In statistical mechanics, such a system is described by the micro canonical ensemble. However, it is convenient to make calculations using the grand canonical ensemble - an ensemble which allows for the exchange of  $E$  and  $N$  with a reservoir at temperature  $T$ . This is valid in the limit  $N \rightarrow \infty$ , where energy and number fluctuations become vanishingly small [86].

In the grand canonical ensemble, an ideal gas of  $n_i$  non-identical particles in state  $i$  with energies  $E_i$ , the partition function is defined as:

$$Z = \prod_i \text{Tr}_i e^{-\beta(E_i - \mu)\hat{n}_i} = \prod_i \sum_n \left( e^{-\beta(E_i - \mu)} \right)^n, \quad (3.1)$$

where  $\beta = 1/k_B T$  and the chemical potential  $\mu$  is the energy required to add an atom to the system. The partition function is a Boltzmann weighted sum of all possible micro-states in the system. Because of this, it may be used to determine all thermodynamic quantities via the grand canonical potential:

$$\Omega(T, V, \mu) = -\frac{1}{\beta} \ln Z. \quad (3.2)$$

As we have seen in Section 1.2, any integer number of bosons may occupy state  $i$ , so the partition function for bosons is:

$$Z_B = \prod_i \sum_n \left( e^{-\beta(E_i - \mu)} \right)^n = \prod_i \frac{1}{1 - e^{-\beta(E_i - \mu)}}. \quad (3.3)$$

Fermions, on the other hand, may never occupy the same state as another Fermion, and so:

$$Z_F = \prod_i \sum_{n=0,1}^{\infty} \left( e^{-\beta(E_i - \mu)} \right)^n = \prod_i \left( 1 + e^{-\beta(E_i - \mu)} \right). \quad (3.4)$$

Using  $Z_B$  and  $Z_F$ , the grand canonical potential is then:

$$\Omega(T, V, \mu) = \pm \frac{1}{\beta} \sum \left( 1 \mp e^{\beta(E_i - \mu)} \right), \quad (3.5)$$

where the upper sign refers to bosons, and the lower sign to fermions. Knowing the grand canonical potential allows us to calculate the the mean total atom number:

$$\langle N \rangle = - \frac{\partial \Omega}{\partial \mu} = \sum_i \langle n_i \rangle. \quad (3.6)$$

The argument in the sum is the average occupancy of site  $i$ :

$$\langle n_i \rangle = f(E_i) = \frac{1}{e^{\beta(E_i - \mu)} \mp 1}, \quad (3.7)$$

with the upper sign again referring to bosons, and the lower sign to fermions.  $f(E_i)$  is the famous Bose-Einstein and Fermi-Dirac distribution function.

## 3.2 $T_F$ for trapped Fermi gases

We may use the Fermi-Dirac distribution function to calculate the temperature at which the quantum statistics of the atoms become important. This transition temperature  $T_F$  is called the Fermi temperature. Recalling the heuristic that a quantum gas is one in which the deBroglie wavelengths of neighbouring atoms overlap, it becomes apparent that  $T_F$  must be depend on density or number. In principle, we can use Equation 3.6 to determine the relationship between  $T_F$  and  $N$ . However, this becomes cumbersome for a large number of particles and so it is easier to take the continuum limit of this sum, integrating with respect to the energy and including the density of states factor  $g(E)$  to properly count the number a states within the energy range  $E$  to  $E + dE$ . In a harmonic trap, the density of states is:

$$g(E) = \frac{E^2}{2(\hbar\bar{\omega})^3}. \quad (3.8)$$

where  $\bar{\omega}^3 = \omega_x \omega_y \omega_z$ . The number of fermions in the trap is then:

$$N = \int_0^\infty dE \frac{g(E)}{e^{\beta(E-\mu)} + 1} = - \left( \frac{k_B T}{\hbar \bar{\omega}} \right)^3 \text{Li}_3 \left( -e^{\beta\mu} \right) \quad (3.9)$$

where  $\text{Li}_s(z) = \sum_{k=1}^\infty \frac{z^k}{k^s}$  is the polylogarithm function. A look at the  $T \rightarrow 0$  behaviour of Equation 3.9 provides us with a definition for  $T_F$ :

$$N \underset{T \rightarrow 0}{=} \int_0^\mu dE g(E) = \frac{1}{6} \left( \frac{\mu}{\hbar \bar{\omega}} \right)^3. \quad (3.10)$$

That is, at zero temperature, atoms will fill all states up to the chemical potential  $\mu$ . The  $T = 0$  chemical potential defines the Fermi energy  $E_F$ , and so the Fermi temperature is:

$$T_F = \frac{\hbar \bar{\omega}}{k_B} (6N)^{1/3}. \quad (3.11)$$

For  $10^5$  atoms in a  $\bar{\omega} = 2\pi \times 100$  Hz trap,  $T_F \approx 400$  nK.

### 3.3 $T_c$ for trapped Bose gases

We may determine the transition temperature for a harmonically trapped gas of bosons,  $T_c$ , in a similar way as we did  $T_F$ . However, in making the continuum approximation, let us also make the approximation that the ground state has  $E = 0$  rather than  $E = \hbar/2(\omega_x + \omega_y + \omega_z)$ . We can then define  $T_c$  as the temperature at which there is a macroscopic occupation of this  $E = 0$  ground state. The number of atoms condensed in this ground state is  $N_0 = N - N_{\text{ex}}$  where  $N$  is the total number of atoms in the system and  $N_{\text{ex}}$  is the number of atoms in excited states, defined as:

$$N_{\text{ex}} = \int_0^\infty dE \frac{g(E)}{e^{\beta(E-\mu)} - 1} = \left( \frac{k_B T}{\hbar \bar{\omega}} \right)^3 \text{Li}_3 \left( e^{\beta\mu} \right). \quad (3.12)$$

The critical temperature is determined by setting  $N_0 = 0$  and  $\mu = 0$ . That is,

$$T_c = \frac{\hbar \bar{\omega}}{k_B} \left( \frac{N}{\text{Li}_3(1)} \right)^{1/3} \approx \frac{\hbar \bar{\omega}}{k_B} 0.94 N^{1/3}. \quad (3.13)$$

For  $10^5$  atoms in a  $\bar{\omega} = 2\pi \times 100$  Hz trap,  $T_c \approx 200$  nK. Below  $T_c$ , the number of condensed atoms grows. We can see this by inserting the implicit expression for  $N$  in Equation 3.13 into

Equation 3.12:

$$N_0(T) = N \left( 1 - \left( \frac{T}{T_c} \right)^3 \right). \quad (3.14)$$

### 3.4 Density distribution

In order to determine the density distribution of a trapped quantum gas it is helpful to work with a semi-classical phase space distribution:

$$f(\mathbf{r}, \mathbf{p}) = \frac{1}{e^{\beta(\mathbf{p}^2/2m+V(\mathbf{r})-\mu)} \mp 1}. \quad (3.15)$$

This distribution is semi-classical because although the form of the distribution function  $f(\mathbf{r}, \mathbf{p})$  is derived from quantum statistics, the energy is a continuous function of position  $\mathbf{r}$  and momentum  $\mathbf{p}$ . This approximation is valid so long as we are not worried about variations in  $\mathbf{r}$  and  $\mathbf{p}$  close to the uncertainty limit. Equivalently, this is valid for large atom numbers where the gas may be treated locally as if it was a bulk gas. This constitutes the local density approximation.

#### 3.4.1 Density of a trapped Fermi cloud

In order to calculate the density, we need to integrate  $f(\mathbf{r}, \mathbf{p})$  over the momentum, normalizing by the average phase space volume  $(2\pi\hbar)^3$  occupied by a single quantum state. For fermions, the density is:

$$n_F(\mathbf{r}) = \frac{1}{(2\pi\hbar)^3} \int d\mathbf{p} f_F(\mathbf{r}, \mathbf{p}) = -\frac{1}{\lambda_{\text{dB}}^3} \text{Li}_{3/2} \left( -e^{\beta(\mu-V(\mathbf{r}))} \right). \quad (3.16)$$

It is interesting to look at the high and low temperature results for  $n_F(\mathbf{r})$ . When  $T \rightarrow \infty$ , we can use the fact that  $\text{Li}_s(z) \xrightarrow{z \ll 1} z$ , and so:

$$n_F(\mathbf{r})|_{T \rightarrow \infty} = n_T(\mathbf{r}) = \frac{N}{\pi^{3/2} \sigma_x \sigma_y \sigma_z} e^{-x^2/2\sigma_x^2 - y^2/2\sigma_y^2 - z^2/2\sigma_z^2} \quad (3.17)$$

where  $\sigma_i = \sqrt{k_B T / m \omega_i^2}$  and we have taken the small factor  $\beta\mu$  to be negligible. We can see that fermions have a Gaussian density distribution at high temperature, exactly what one would calculate for an ideal gas. On the other hand, if we look at  $T \rightarrow 0$  behaviour, and make use of the limit  $\text{Li}_s(z) \xrightarrow{z \rightarrow \infty} \ln^s(z) / \Gamma(s+1)$ , where  $\Gamma(s)$  is the Gamma function, then:

$$n_F(\mathbf{r})|_{T \rightarrow 0} = \frac{8}{\pi^2} \frac{N}{R_{F_x} R_{F_y} R_{F_z}} \text{Re} \left( \left( 1 - \frac{x^2}{R_{F_x}^2} - \frac{y^2}{R_{F_y}^2} - \frac{z^2}{R_{F_z}^2} \right)^{3/2} \right). \quad (3.18)$$

Here, we have used the result from Section 3.2 that at zero temperature,  $\mu = E_F = \hbar\bar{\omega} (6N)^{1/3}$ . Equation 3.18 is written in terms of the Thomas-Fermi radius  $R_{F_i} \equiv \sqrt{2E_F/m\omega_i^2}$ , defined as the farthest *in situ* extent of a Fermi cloud at zero temperature. For  $10^5$   $^{40}\text{K}$  atoms in a  $\bar{\omega} = 2\pi \times 100\text{Hz}$  trap,  $R_F \approx 20\mu\text{m}$ .

### 3.4.2 Density of a trapped Bose cloud

We may follow the same approach as in Section 3.4.1 in order to find the density of *excited* bosons in a harmonic trap:

$$n_{\text{ex}}(\mathbf{r}) = \frac{1}{(2\pi\hbar)^3} \int d\mathbf{p} f_B(\mathbf{r}, \mathbf{p}) = \frac{1}{\lambda_{\text{dB}}^3} \text{Li}_{3/2} \left( e^{\beta(\mu - V(\mathbf{r}))} \right). \quad (3.19)$$

In the  $T \rightarrow \infty$  limit,  $n_{\text{ex}}(\mathbf{r}) = n(\mathbf{r})$  reduces to the same Gaussian distribution as Equation 3.17. We also know from Equation 3.14 that  $n_{\text{ex}}(\mathbf{r}) = 0$  in the  $T \rightarrow 0$  limit since all atoms will be in the condensed state. However, properly determining the density distribution of the condensed atoms  $n_0(\mathbf{r})$  requires that we include the effect of interactions. We can do this using the Gross-Pitaevski (G-P) equation [33]:

$$-\frac{\hbar^2}{2m} \nabla^2 \psi(\mathbf{r}) + V(\mathbf{r})\psi(\mathbf{r}) + U_0 |\psi(\mathbf{r})|^2 \psi(\mathbf{r}) = \mu \psi(\mathbf{r}). \quad (3.20)$$

The G-P equation describes the time evolution of the order parameter  $\psi(\mathbf{r}) = \sqrt{n_0(\mathbf{r})} e^{-i\mu t/\hbar}$  under the effects of an external potential  $V(\mathbf{r})$  and the mean-field contact interaction  $U_0 = 4\pi\hbar^2 a/m$  from Section 1.2. The equation is valid in the limit where the scattering length  $a$  is much less than the inter-particle spacing. When the number of atoms is large and interactions are repulsive, the kinetic energy term can be ignored. This is the Thomas-Fermi approximation, as applied to the G-P equation. Using this approximation, it is easy to solve for the density  $n_0(\mathbf{r}) = |\psi(\mathbf{r})|^2$ :

$$n_0(\mathbf{r}) = \frac{\mu - \frac{m}{2} (\omega_x^2 x^2 - \omega_y^2 y^2 - \omega_z^2 z^2)}{U_0}. \quad (3.21)$$

We can see that  $n_0(\mathbf{r})$  has an inverted parabolic shape, different from  $n_F(\mathbf{r})|_{T \rightarrow 0}$ . We may use Equation 3.21 along with the normalization condition  $N = \int d\mathbf{r} n_0(\mathbf{r})$  to solve for the chemical potential:

$$\mu = \frac{\hbar\bar{\omega}}{2} \left( \frac{Na}{\sigma} \right)^{2/5} \quad (3.22)$$

where  $\sigma = \sqrt{\hbar/m\bar{\omega}}$  is the ground state harmonic oscillator length. In analogy with the fermionic Thomas-Fermi radius  $R_{F_i}$ , we may define the bosonic Thomas-Fermi radius:

$$R_{B_i} = \sqrt{\frac{2\mu}{m\omega_i^2}} = \sigma \left( \frac{15Na}{\sigma} \right)^{1/5}. \quad (3.23)$$

For  $10^5$   $^{87}\text{Rb}$  atoms in a  $\bar{\omega} = 2\pi \times 100$  Hz trap,  $R_B \approx 6\mu\text{m}$ . This is more than a factor of 3 smaller than the  $R_F$  calculated for an equivalent number of  $^{40}\text{K}$  fermions at zero temperature.

## 3.5 Evaporation to quantum degeneracy

In our experiment, we bring atoms to quantum degeneracy by evaporative cooling. This is done, successively, in a magnetic and optical trap, as described in Section 2.6 and Section 2.8. In this section, we show the onset of quantum behaviour for a gas of  $^{87}\text{Rb}$  in a plugged quadrupole trap, and for both  $^{87}\text{Rb}$  and  $^{40}\text{K}$  in a crossed dipole trap.

### 3.5.1 A quantum gas in a plugged quadrupole trap

The first BEC of Na atoms was created in a plugged magnetic quadrupole trap [87]. It was observed that a trap that combined the linear potential of a quadrupole field with a repulsive optical potential offered both a large volume trap that allowed for efficient evaporative cooling, and protection against Majorana loss and heating. Here we describe the plugged quadrupole trap potential and demonstrate the evaporative cooling of  $^{87}\text{Rb}$  to degeneracy in it, noting that  $^{40}\text{K}$  may be sympathetically cooled simultaneously.

Our plugged quadrupole trap is a combination of a magnetic, optical, and gravitational potential:

$$V_{\text{PQ}}(\mathbf{r}) = V_{\text{mag}}(\mathbf{r}) + V_{\text{dip}}(\mathbf{r}) + V_{\text{grav}}(\mathbf{r}) \quad (3.24)$$

where  $V_{\text{mag}}(\mathbf{r}) = \mu_{\text{BGF}} m_{\text{F}} |\mathbf{B}(\mathbf{r})|$ ,  $\mathbf{B}(\mathbf{r}) = \beta/2\mathbf{x} + \beta/2\mathbf{y} - \beta\mathbf{z}$  is the quadrupole field with  $\beta$  the magnetic gradient in the vertical  $\mathbf{z}$  direction.  $V_{\text{dip}}(\mathbf{r})$  is defined in Equation A.10, and  $V_{\text{grav}}(\mathbf{r}) = mgz$  is the gravitation potential. If we choose the plug beam to travel along the  $\mathbf{y}$  direction and through the centre of the quadrupole field, as depicted in Figure 3.1, then we may define the effective harmonic trapping frequencies of  $V_{\text{PQ}}(\mathbf{r})$  [87]:

$$\omega_{\text{PQ}y}^2 = \frac{\mu_{\text{BGF}} m_{\text{F}} \beta}{2mx_0}, \quad \omega_{\text{PQ}z}^2 = 3\omega_{\text{PQ}y}^2, \quad \omega_{\text{PQ}x}^2 = \omega_{\text{PQ}y}^2 (4x_0^2/w_0^2 - 1). \quad (3.25)$$

The oscillation frequencies are written in terms of the plug beam waist  $w_0$ , as well as  $x_0$ ,

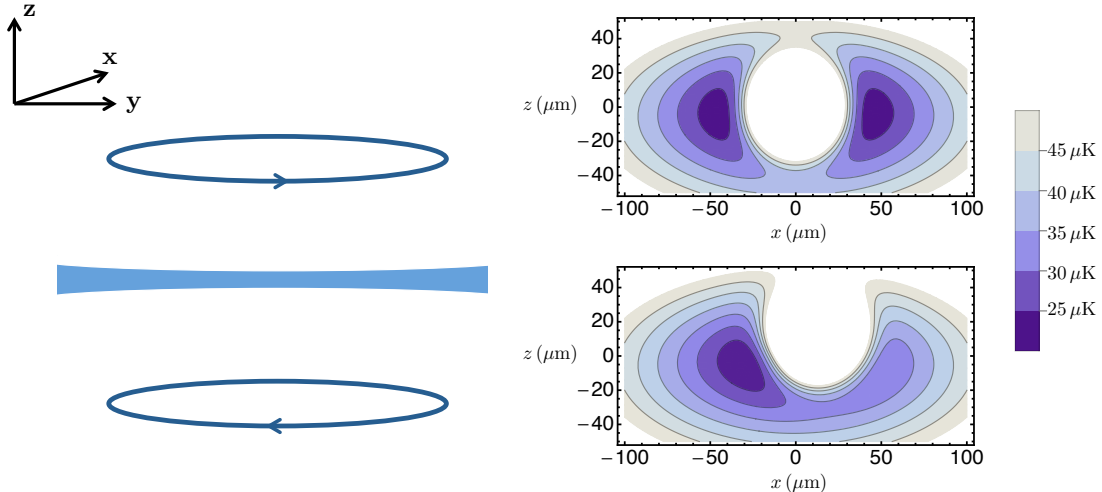


**Figure 3.1: Plugged quadrupole trap potential** Left, a cartoon illustration of the hardware ingredients that constitute our plugged quadrupole trap: a blue-detuned beam propagates horizontally through the centre of a magnetic quadrupole field formed from two sets of coils. The plot on the top right shows a calculation of  $V_{\text{PQ}}(\mathbf{r})$  when the plug beam is exactly aligned to the centre of the magnetic field. Notice the two minima that are produced. We may modify the trap so as to produce only one potential minimum by slightly mis-aligning the plug beam. The plot on the bottom right shows  $V_{\text{PQ}}(\mathbf{r})$  when the plug beam is positioned  $12\mu\text{m}$  above, and  $12\mu\text{m}$  in the positive  $\mathbf{x}$  direction of the magnetic field centre,

the distance of the plugged quadrupole trap minima from the magnetic field centre.  $x_0$  is a solution to the equation  $\partial V_{\text{PQ}}(\mathbf{r})/\partial \mathbf{r}|_{x_0} = 0$ . For our chosen parameters (a plug beam with 300mW of 760nm light focused to  $w_0 = 30\mu\text{m}$  combined with a  $\beta=150\text{G/cm}$  magnetic gradient),  $x_0 \approx 40\mu\text{m}$ , and so  $\{\omega_{\text{PQ}y}, \omega_{\text{PQ}z}, \omega_{\text{PQ}x}\} = 2\pi \times \{175, 302, 432\}\text{Hz}$ .

We can see from Figure 3.1 that a plug beam aligned to the centre of the magnetic field produces a trap with two minima. This is undesirable as it splits the cloud in two when the gas becomes as cold, or colder than, the plug height  $\approx V_{\text{dip}}(0)/k_B$ . This makes the production of a BEC more difficult, as well making the subsequent loading of atoms into the crossed dipole trap less efficient. To circumvent these issues, we slightly mis-align the plug beam by a distance roughly equal to  $w_0/3$ . This destroys the symmetry, resulting in slightly modified trap frequencies  $\omega_{\text{PQ}}$  from those defined in Equation 3.25 [88], but only one potential minimum. We have found that it is best to align the plug beam equal parts above and to one horizontal side of the magnetic trap zero. Doing so results in larger BECs, and more efficient loading into the crossed dipole trap. Loading into the crossed dipole trap involves ramping down the magnetic field, gently “dropping” the cloud into the optical potential formed by elliptical beams while keeping the plug beam on. Aligning the plug beam above the trap centre allows for better mode matching between traps.

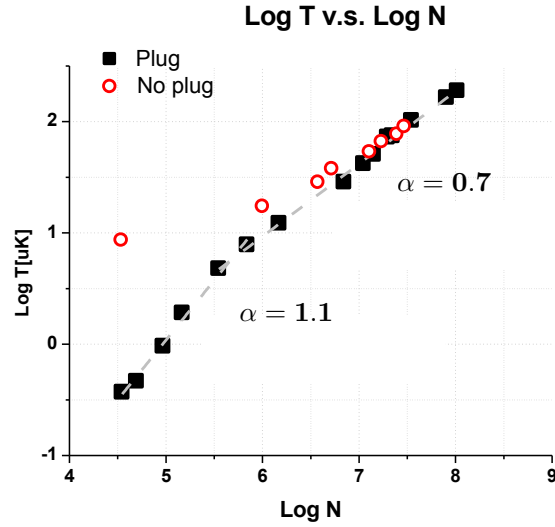


**Figure 3.2:**  $^{87}\text{Rb}$  Evaporation efficiency A comparison of the  $^{87}\text{Rb}$  evaporation efficiency with and without the plug beam on. The parameter  $\alpha$  is defined implicitly through the proportionality  $T \propto N^\alpha$ , and discussed in Section 2.6.

Figure 3.2 shows the evaporation efficiency of  $^{87}\text{Rb}$  in a plugged and un-plugged quadrupole trap. We can see the dramatic effect that the plug beam has on the ability to cool a large number of atoms below  $1\mu\text{K}$ . Using the definition for  $T_c$  in Equation 3.13 alongside the derived oscillation frequencies  $\omega_{\text{PQ}}$ , we would predict that  $T_c = 10.78(N)^{1/3}\text{nK}$ , equal to  $500\text{nK}$  for  $10^5$  atoms. This is commensurate with what we observe. We note that in a plugged quadrupole trap, the trap bottom is positioned at non-zero magnetic field. This means that the end frequency of the RF sweep is very sensitive to plug beam alignment.

### 3.5.2 A quantum gas in a crossed dipole trap

In order to sympathetically cool a large cloud of  $^{40}\text{K}$ , it is useful to perform evaporation in an crossed dipole trap. Optical evaporation can be preferable to magnetic evaporation for a number of reasons: the absence of current through a large inductance coil means that the potential may be changed quickly without residual eddy current potentials; the possibility of loose confinement in optical traps results in lower 3-body loss rates; optical trapping allows atoms to be transferred into their lowest hyperfine ground states, mitigating 2-body losses; Feshbach resonances may be used to increase the thermalization rate. Furthermore, evaporation in an optical dipole trap results in a cloud of atoms that may be adiabatically loaded into a mode-matched optical lattice potential.

Our optical dipole trap is produced from two orthogonally propagating elliptical dipole

beams, resulting in the potential:

$$V_{\text{XDT}}(\mathbf{r}) = V_{\text{dip1}}(\mathbf{r}) + V_{\text{dip2}}(\mathbf{r}) + V_{\text{grav}}(\mathbf{r}). \quad (3.26)$$

Keeping the same axes as in Figure 3.1, we have  $V_{\text{dip1}}(\mathbf{r})$  propagating along the  $\mathbf{y}$  direction and  $V_{\text{dip2}}(\mathbf{r})$  propagating along the  $\mathbf{x}$  direction:

$$V_{\text{dip1}}(\mathbf{r}) = V_{\text{dip1}} e^{-2\frac{x^2}{w_{x1}^2(y)} - 2\frac{z^2}{w_{z1}^2(y)}}, \quad V_{\text{dip2}}(\mathbf{r}) = V_{\text{dip2}} e^{-2\frac{y^2}{w_{y2}^2(x)} - 2\frac{z^2}{w_{z2}^2(x)}} \quad (3.27)$$

where  $w_{x1}(y) = w_{x1}\sqrt{1 + (y/y_{\text{Rx},1})^2}$  is the  $1/e^2$  radius (or ‘‘waist’’) of dipole 1 in the  $\mathbf{x}$  direction,  $y_{\text{Rx}} = \pi w_{x1}^2/\lambda$  is the Rayleigh length of the focus in the  $\mathbf{x}$  direction, and all other waists and Rayleigh lengths may be likewise obtained by a suitable substitution of indices. It is convenient to define a new Rayleigh length for each beam:

$$y_{\text{R}} = \frac{y_{\text{Rx}}y_{\text{Rz}}}{\sqrt{(y_{\text{Rx}}^2 + y_{\text{Rz}}^2)/2}}, \quad x_{\text{R}} = \frac{x_{\text{Ry}}x_{\text{Rz}}}{\sqrt{(x_{\text{Ry}}^2 + x_{\text{Rz}}^2)/2}}. \quad (3.28)$$

When the dipole potentials are strong enough that the gravitational potential may be ignored, we may approximate  $V_{\text{XDT}}(\mathbf{r})$  as a harmonic trap with frequencies:

$$\omega_{\text{XDT},x}^2 = \frac{1}{m} \left( \frac{4V_{\text{dip1}}}{w_{x1}^2} + \frac{2V_{\text{dip2}}}{y_{\text{R}}^2} \right) \quad (3.29)$$

$$\omega_{\text{XDT},y}^2 = \frac{1}{m} \left( \frac{4V_{\text{dip1}}}{w_{y1}^2} + \frac{2V_{\text{dip2}}}{x_{\text{R}}^2} \right) \quad (3.30)$$

$$\omega_{\text{XDT},z}^2 = \frac{4}{m} \left( \frac{V_{\text{dip1}}}{w_{z1}^2} + \frac{V_{\text{dip2}}}{w_{z2}^2} \right). \quad (3.31)$$

Noting from Equation A.10 that  $V_{\text{dip1}} \propto I(0) = 2P/\pi w_{x1}w_{z1}$ , and similarly for  $V_{\text{dip2}}$ , we can make the potential contributed by each beam equal by an appropriate scaling of the powers to the waists. By doing this,  $V_{\text{dip1}} = V_{\text{dip2}}$  for all powers and we conserve the aspect ratio of the trap. That is,  $\omega_{\text{XDT},x} : \omega_{\text{XDT},y} : \omega_{\text{XDT},z}$  remains fixed. For our trap parameters,  $^{40}\text{K}$  has the trap frequencies  $\omega_{\text{XDT},\text{K}} \equiv \{\omega_{\text{XDT},x}, \omega_{\text{XDT},y}, \omega_{\text{XDT},z}\} = 2\pi \times \{76, 53, 510\} \text{Hz} \times \sqrt{P(W)}$  and  $^{87}\text{Rb}$  has the frequencies  $\omega_{\text{XDT},\text{Rb}} = \kappa \omega_{\text{XDT},\text{K}}$ , where the factor  $\kappa$  is equal to  $\sqrt{V_{\text{dip,Rb}}/V_{\text{dip,K}}} \sqrt{m_{\text{K}}/m_{\text{Rb}}} \approx 0.73$ . Comparing the mean trap frequency at the end of plugged quadruple evaporation  $\bar{\omega}_{\text{PQ}} = 2\pi \times 420 \text{Hz}$  with the mean trap frequency immediately after loading into the crossed dipole trap  $\bar{\omega}_{\text{XDT}} = 2\pi \times 180 \text{Hz}$  indicates that we should expect adiabatic cooling during transfer by a factor  $\bar{\omega}_{\text{XDT},\text{K}}/\bar{\omega}_{\text{PQ},\text{K}}$ . This is indeed what we observe: the  $^{40}\text{K}$  cloud cools from  $7 \mu\text{K}$  in the plugged quadruple trap to  $3 \mu\text{K}$  in the crossed dipole trap.

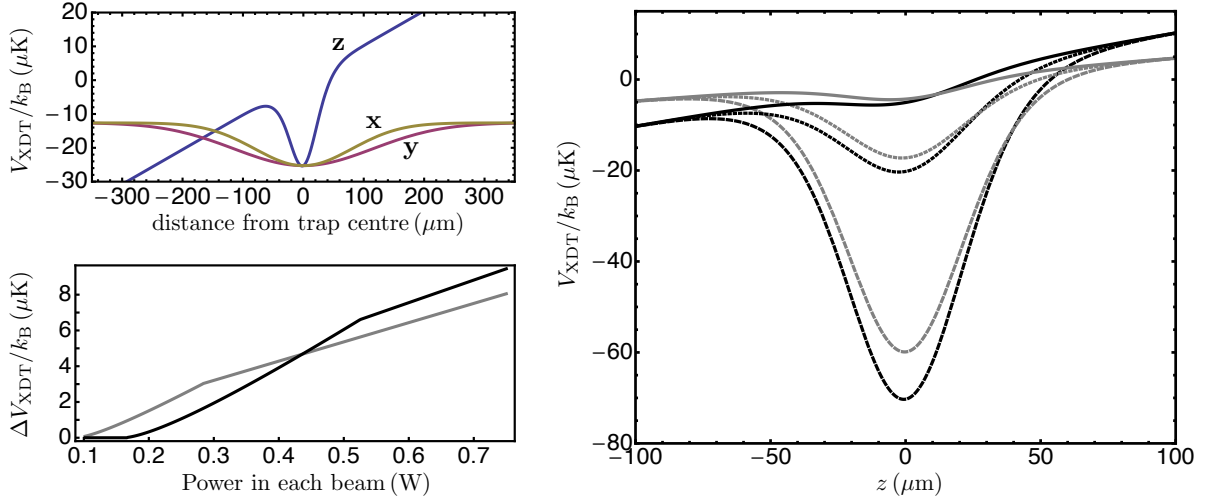


**Figure 3.3: Crossed-Dipole trap potential** Top left, the  $V_{\text{XDT}}(\mathbf{r})$  potential profile for  $^{40}\text{K}$  along  $x$ ,  $y$ , and  $z$  for 1W of power in each beam. For comparison, the thermal width of a  $3\mu\text{K}$  cloud of  $^{40}\text{K}$  in this trap is  $\{\sigma_x, \sigma_y, \sigma_z\} = \{52, 75, 8\}\mu\text{m}$ . Bottom left, the crossed-dipole trap potential depth for  $^{87}\text{Rb}$  (black) and  $^{40}\text{K}$  (grey) as a function of optical power. Note the “kinks”, marking the point at which the potential depth becomes smaller in the vertical direction rather than the horizontal direction. Right, the trap profiles along the vertical direction for  $^{87}\text{Rb}$  (black) and  $^{40}\text{K}$  (grey) immediately after loading the crossed-dipole trap (dashed), after ramping to the sympathetic cooling regime (dotted), and at the end evaporation power (solid).

For dipole powers below a few hundred mW, the gravitational potential becomes important. In fact, the gravitational potential is essential for evaporation - and specifically, for sympathetic evaporation of  $^{40}\text{K}$  using  $^{87}\text{Rb}$  - to work. This is because the gravitational potential provides a selective way of ejecting the heavier  $^{87}\text{Rb}$  atoms from the optical trap. This only works in the sympathetic cooling regime of crossed dipole potential, where the power is below the threshold value - 420 mW in our experiment - where the potential has a greater depth for  $^{40}\text{K}$  rather than for  $^{87}\text{Rb}$ . See the plot of  $\Delta V_{\text{XDT}}$  in Figure 3.3 for an illustration. Above this value,  $^{87}\text{Rb}$  is held more tightly due to the closer detuning of the 1054 nm light.

Gravity has the additional effect of reducing the effective oscillation frequencies in Equation 3.29, Equation 3.30, and Equation 3.31, and offsets the trap minimum. Because gravity affects  $^{87}\text{Rb}$  and  $^{40}\text{K}$  differently, there will be a “sag” between the clouds which reduces their spatial overlap. This is to be avoided: sympathetic cooling requires that we maintain good thermal contact between clouds since the inter-species scattering rate  $\Gamma_{\text{Rb-K}}$  is proportional to the density overlap  $\langle n_{\text{K}} \rangle_{\text{Rb}}$  in the vertical direction [89]:

$$\langle n_{\text{K}} \rangle_{\text{Rb}} = \frac{1}{N_{\text{Rb}}} \int d^3z n_{\text{K}}(z - z_{0\text{K}}) n_{\text{Rb}}(z - z_{0\text{Rb}}) \quad (3.32)$$

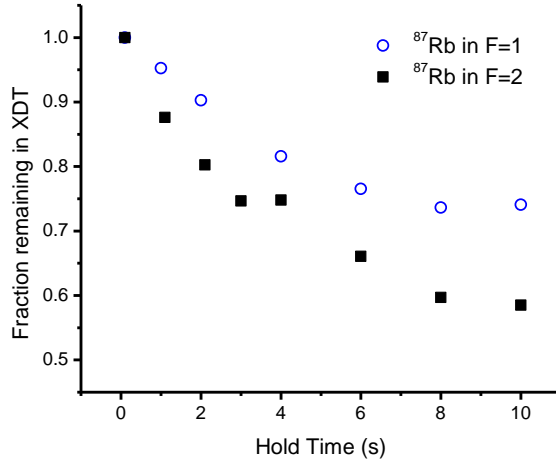


**Figure 3.4: A comparison of  $^{40}\text{K}$  loss for  $^{87}\text{Rb}$  in different hyperfine ground states.**  $^{40}\text{K}$  and  $^{87}\text{Rb}$  atoms at  $3\ \mu\text{K}$  are loaded into a crossed dipole trap. For the blue circles,  $^{87}\text{Rb}$  atoms are adiabatically transferred into  $|F = 1, m_F = 1\rangle$  and the remaining  $|F = 2, m_F = 2\rangle$  are removed with a short pulse of resonant light.

where  $n(z - z_0) = N\sqrt{m\omega^2/2\pi k_B T} e^{-\frac{m\omega^2(z-z_0)^2}{2k_B T}}$  is the 1D density, and  $z_{0\text{K}} = -g/\omega_{\text{K}}^2$  and  $z_{0\text{Rb}} = -g/\omega_{\text{Rb}}^2$  are the offsets in the potential minima due to gravitational sag. The fraction by which gravity reduces the density overlap is:

$$f_{\text{sag}} \equiv \frac{\langle n_{\text{K}} \rangle_{\text{Rb}}}{\langle n_{\text{K}} \rangle_{\text{Rb}}|_{g \rightarrow 0}} = e^{-\frac{(\kappa^2 - 1)^2}{2\kappa^2(\kappa^2 + m_{\text{K}}/m_{\text{Rb}})^2} \frac{m_{\text{K}} g^2}{\omega_{\text{K}}^2 k_B T}}. \quad (3.33)$$

We see that gravitational sag reduces the density overlap, especially near the end of evaporation when the temperature is low and the trap frequencies are reduced. We may see this qualitatively by looking at the vertical profile of  $V_{\text{XDT}}(z)$  for different optical powers. However, we note that choosing elliptical beams with tight confinement in the vertical direction, and thus large  $\omega_{\text{K}}$ , counter-acts this problem.

### $^{87}\text{Rb}$ state transfer from $\mathbf{F} = 2$ to $\mathbf{F} = 1$

Evaporation in an optical trap allows us the freedom to access the manifold of internal magnetic states of the atoms as they are no longer simply needed for trapping. In particular, for a two-species evaporation, this allows us to transfer atoms into states that stabilize the mixture, protecting it against relaxation processes that can transfer energy from internal to external states. Hyperfine relaxation, dipolar relaxation, and spin exchange are examples of these types of processes.

If we are able to place  $^{87}\text{Rb}$  and  $^{40}\text{K}$  atoms into their respective absolute ground states ( $|F = 1, m_F = 1\rangle$  and  $|F = 9/2, m_F = -9/2\rangle$ ) then a cloud of  $^{87}\text{Rb}$  and  $^{40}\text{K}$  will be protected against relaxation processes since there is no other state for a colliding Rb-K pair to relax into [90]. However, we can make our job even simpler by noting that if we put  $^{87}\text{Rb}$  into  $|F = 1, m_F = 1\rangle$ , it doesn't matter what state in the  $F = 9/2$  manifold is in since the Landé g-factor of  $^{87}\text{Rb}$  in  $F = 1$  is greater than that of  $^{40}\text{K}$  in  $F = 9/2$ . That is, the mixture will be stable because even if  $^{40}\text{K}$  would relax via a hypothetical collision with  $^{87}\text{Rb}$  to an adjacent and lower  $m_F$  state, the resulting energy is less than is required to excite  $^{87}\text{Rb}$  to an adjacent and higher  $m_F$  state, and so the process is forbidden in the first place.

In Figure 3.4 we compare the loss rate of  $^{40}\text{K}$  in the crossed-dipole trap when  $^{87}\text{Rb}$  is placed in a state that protects against Rb-K loss ( $|F = 1, m_F = 1\rangle$ ), against the loss rate when  $^{87}\text{Rb}$  is placed in a state that does not protect against loss ( $|F = 2, m_F = 2\rangle$ ).

We transfer  $^{87}\text{Rb}$  from  $F = 2$  to  $F = 1$  by applying a 50 ms long 6.8756 GHz  $\mu$ -wave pulse while sweeping the magnetic field from 20.1 to 20.0 G. We are able to transfer over 95% of the atoms in  $F = 1$ , and we remove any atoms remaining in  $F = 2$  with a short pulse of resonant probe light.

### Evaporation trajectory

We begin evaporation in the crossed-dipole trap by quickly reducing the dipole powers to a regime where  $^{87}\text{Rb}$  can sympathetically cool  $^{40}\text{K}$ . Empirically, we find that ramping dipole 1 and 2 to 800 mW and 1.8 W, respectively, optimizes the phase space density of gas at the end of evaporation. Note that this value is above the calculated sympathetic cooling threshold powers of 420 mW and 920 mW calculated using Equation A.10.

We proceed with evaporation by simultaneously reducing the powers in the two dipole beams in such a way that each beam provides equivalent potential depth. The powers are reduced exponentially in 22 s, until we produce a degenerate Fermi gas of  $1 \times 10^5$   $^{40}\text{K}$  in  $|9/2, 9/2\rangle$  at 300 nK: see Figure 3.6b. We can also make a BEC of  $1 \times 10^5$   $^{87}\text{Rb}$  in  $|2, 2\rangle$  by evaporating in the crossed-dipole trap in the same manner, save for the transfer from  $F = 2$  to  $F = 1$ : see Figure 3.6a.

## 3.6 Imaging and measurement

### 3.6.1 Absorption imaging

The first images of quantum degenerate gases were obtained by releasing the cloud from the trap, allowing the density to decrease, and then measuring the absorption of a probe beam passing

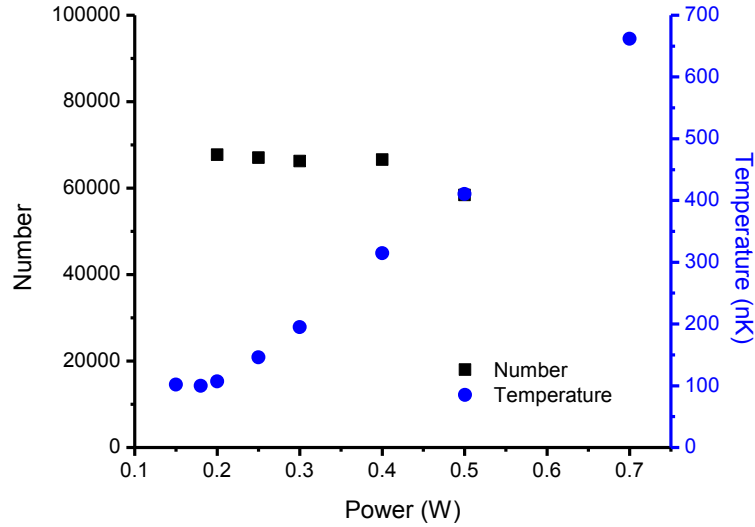


**Figure 3.5:**  $^{40}\text{K}$  evaporation in crossed-dipole trap  $1.2 \times 10^5$   $^{40}\text{K}$  atoms are initially loaded into the crossed dipole trap. The power in the crossed dipole trap is lowered exponentially in 22 s with a time constant of 7 s from 800 mW in dipole 1 to the power indicated on the horizontal axis. The power in dipole 2 is reduced according to the scaling mentioned in Section 3.5.2.

through the cloud. Absorption imaging uses the Lambert-Beer Law, that the attenuation of light is a simple exponential function of the *column density*. The resultant intensity  $I_a(y, z)$  is recorded with a camera, where we take  $x$  to be the optical axis of the probe beam and imaging system. A second image,  $I_0(y, z)$ , without the atoms, is taken to calibrate the intensity of light incident on the cloud. The divided image can be related to the atomic density via the scattering cross-section  $\sigma_{SC}$  through

$$\ln \left( \frac{I_0(y, z)}{I_a(y, z)} \right) = \sigma_{SC} \int n(x, y, z) dx \equiv \text{OD}(y, z) \quad (3.34)$$

This measured quantity is the *optical density* (OD).

Free-flight expansion is typically required to reduce the OD to a measurable level, optimally near unity [34]. Since the resonant cross-section is roughly  $\lambda^2$ , a typical density of  $n \sim 10^{19} \text{ m}^{-3}$  would give an attenuation length of  $1/n\sigma_{SC} \sim 100 \text{ nm}$ . This is on the order of the inter-particle spacing, and thus only a cloud that was one atom thick can be imaged with resonant absorption. For typical three-dimensional clouds of  $10^5$  atoms, the average radius is several microns, which would give an  $\text{OD} > 10$  in the trap. Instead, the cloud is released, allowed to expand for 10–20 ms, before imaging.

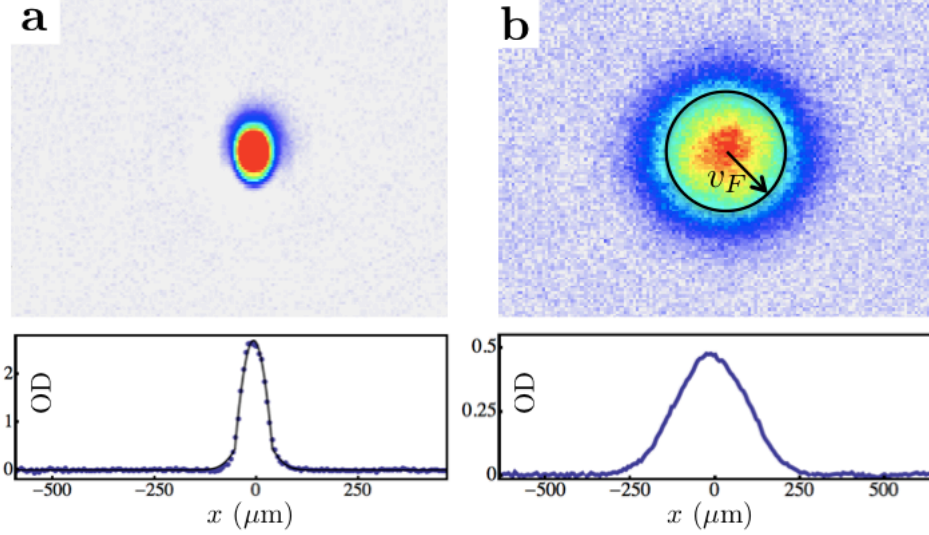


**Figure 3.6: A degenerate cloud of  $^{87}\text{Rb}$  and  $^{40}\text{K}$ .** (a) A quasi-pure BEC of  $5 \times 10^4$   $^{87}\text{Rb}$  atoms after evaporation in both a plugged-quadrupole magnetic trap and a crossed-dipole trap, 15 ms after release from the trap. (b) A quantum degenerate cloud of  $1.1 \times 10^5$   $^{40}\text{K}$  atoms at 320 nK, 12 ms after release from the trap. Color represents the integrated column density, or optical density (OD).

### 3.6.2 Time-of-flight identification of a quantum gas

The temperature and degeneracy of a gas of atoms are usually identified by taking an absorption image and fitting the optical density after some time of flight. In this section, we describe how the in-trap density evolves under time of flight, studying the specific examples of a thermal, Fermi, and Bose gas.

#### Degenerate Fermi gas

We have seen in Section 3.4.1 that the density of fermions in a cylindrically symmetric harmonic trap is  $n_F(\rho) = -\frac{1}{\lambda_{\text{dB}}^3} \text{Li}_{3/2}(\zeta e^{-\beta V(\rho)})$ , where  $\zeta = e^{\beta\mu}$  is the fugacity and  $\rho = x^2 + y^2 + \lambda^2 z^2$  is the scaled coordinate. We can then use the result from [91] that for an ideal gas in the Thomas-Fermi limit released from a harmonic trap, time of flight expansion is equivalent to a re-scaling of the coordinates  $x_i \rightarrow \frac{x_i}{\sqrt{1+(\omega_i t)^2}}$ , resulting in a density  $n(\rho) \rightarrow \frac{n(\rho)}{(1+(\omega_r t)^2)\sqrt{1+(\omega_z t)^2}}$ . Making this substitution in Equation 3.34, we get:

$$\text{OD}_F(y, z) = -\frac{\sigma_{SC}}{2\sqrt{1+(\omega_r t)^2}\sqrt{1+(\omega_z t)^2}} \frac{m(k_B T)^2}{\pi \hbar^3 \omega_r} \text{Li}_2\left(-\zeta e^{-\frac{y^2}{2\sigma_r^2} - \frac{z^2}{2\sigma_z^2}}\right) \quad (3.35)$$

where  $\sigma_r^2 = \frac{k_B T}{m\omega_r^2} \sqrt{1 + (\omega_r t)^2}$  and  $\sigma_z^2 = \frac{k_B T}{m\omega_z^2} \sqrt{1 + (\omega_z t)^2}$ . In the long time limit,  $\omega_r t, \omega_z t \gg 1$ , the cloud expands isotropically and the optical density loses its explicit dependence on the trapping frequencies  $\omega_r$  and  $\omega_z$ :

$$\text{OD}_F(y, z) |_{\omega t \gg 1} = -\frac{3N\sigma_{SC}m}{\pi t^2} \left(\frac{T}{T_F}\right)^2 \frac{1}{k_B T} \text{Li}_2\left(-\zeta e^{-(y^2+z^2)m/2k_B T t^2}\right). \quad (3.36)$$

### Thermal gas

As in Section 3.4.1, we may take the high temperature limit of the density  $n_F(\rho)$  to find the thermal distribution  $n_T(\rho) = \frac{N}{\pi^{3/2}\sigma_r^2\sigma_z} e^{-\beta V(\rho)}$ . We may again re-scale the coordinates and density as above, finding the optical density:

$$\text{OD}_T(y, z) = -\frac{2\pi N}{\pi^{3/4}} \frac{\sigma_{SC}}{\sqrt{1 + (\omega_r t)^2} \sqrt{1 + (\omega_z t)^2}} \frac{m\omega_r\omega_z}{k_B T} e^{-\frac{y^2}{2\sigma_r^2} - \frac{z^2}{2\sigma_z^2}}. \quad (3.37)$$

In the long time limit, the cloud expands isotropically:

$$\text{OD}_T(y, z) |_{\omega t \gg 1} = -\frac{2\pi N}{\pi^{3/4}} \frac{\sigma_{SC}m}{k_B T t^2} e^{-(y^2+z^2)m/2k_B T t^2}. \quad (3.38)$$

We can see that the width of the cloud after time of flight is an explicit measure of the temperature.

### Degenerate Bose gas

We saw in Section 3.4.2 that in the Thomas-Fermi approximation, a BEC has the density distribution  $n_0(\rho) = (\mu - V(\rho))/U_0$  which, for a harmonic trap  $V(\rho) = \frac{1}{2}m\omega_r^2\rho^2$ , results in a density with an inverted parabolic distribution. Upon sudden release from the trap, potential energy is converted into kinetic energy  $\frac{1}{2}mv_i^2 = \frac{1}{2}m\omega_i^2x_i^2$ , and so the final position  $x'_i$  after some time-of-flight time  $t$  is related to the initial position  $x_i$  via:

$$x'_i = \sqrt{x_i^2 + (v_i t)^2} = x_i \sqrt{1 + (\omega_i t)^2} \quad (3.39)$$

For longer time-of-flight times, the imaged position is just the scaled initial position,  $x'_i = x_i\omega_i t$ , and thus the cloud retains its inverted parabolic density distribution save for an inversion of the aspect ratio.

Figure 3.6 shows absorption images of quantum gases. The different nature of Bose and Fermi statistics is evident when comparing images of  $^{87}\text{Rb}$  and  $^{40}\text{K}$ : the bosonic  $^{87}\text{Rb}$  cloud

expands less than the fermionic  $^{40}\text{K}$  cloud. Whereas bosons “condense” into low-momenta states of the trap, Fermi pressure forces fermions apart and into higher-momenta states.

## Chapter 4

# Optical Lattices

The behaviour of atoms in periodic optical lattice potentials has been of interest since the first investigations of atoms diffracting [131] and scattering [132] off of standing light waves. During the hunt for a fast, laser-cooling approach to quantum degeneracy, optical lattices were employed due to the protection they provided against density and temperature limiting photon re-absorption process [133]. They have found uses in optical atomic clock experiments where they suppress interaction broadening of a narrow linewidth transition [134]. Optical lattices have been used in cavities to couple to macroscopic mechanical oscillators [135] and realize exotic phase transition [136]. They have even been proposed as system for cluster state quantum information [137].

Perhaps the most prevalent use of optical lattices in the past decade has been as a platform for the quantum simulation of condensed matter materials. Ever since the observation of the Superfluid-Mott insulator phase transition by Greiner *et al.* [138], optical lattices have been an area of concentration for investigating the behaviour of strongly correlated many-body systems.

We begin this chapter with a review of optical lattice potentials, using as a starting point the optical dipole potential  $V_{\text{dip}}(\mathbf{r})$  derived in Section A.2. The next sections are devoted to calculating the relevant states and energies of atoms in these potentials. We discuss the experimental implementation and characterization of our optical lattice system in Section 5.7. The final sections of this chapter describe our observations of the  $^{87}\text{Rb}$  superfluid-Mott insulator transition and the localization of  $^{40}\text{K}$  atoms in Section 5.8 and Section 5.9, respectively.

## 4.1 Gaussian optical lattices

If a linearly polarized optical beam travelling along the  $\mathbf{z}$  direction is retro-reflected upon itself, a standing-wave intensity pattern is formed:

$$V_{\text{latt}_{1\text{D}}}(\mathbf{r}) = 4V_{\text{dip}}(\mathbf{r}) \cos^2(kz), \quad (4.1)$$

with  $k = 2\pi/\lambda$  the spatial frequency and  $\lambda$  the wavelength of the optical beam. Equation 5.1 describes an *optical lattice* potential, with  $V_{\text{dip}}(\mathbf{r})$  defined in Equation A.10. Because  $V_{\text{dip}}(\mathbf{r})$  is produced from a beam with a Gaussian intensity profile, the optical lattice potential depth will vary in space with the underlying harmonic intensity envelope. In the following, we derive what the effective harmonic trap frequencies are as a function of beam parameters.

A Gaussian beam travelling in the  $\mathbf{z}$  direction has the intensity profile:

$$I(r, z) = \frac{2P}{\pi w^2(z)} e^{-2\frac{r^2}{w^2(z)}} \quad (4.2)$$

where  $P$  is the the power of the beam,  $w(z) = w_0 \sqrt{1 + (z/z_R)^2}$  is the  $1/e^2$  radius of the beam, and  $z_R = \pi w_0^2/\lambda$  is the Rayleigh length. Optical beams along the  $\mathbf{x}$  and  $\mathbf{y}$  directions may also be added to produce a three-dimensional standing-wave pattern:

$$V_{\text{latt}}(\mathbf{r}) = V_x e^{-2\frac{y^2+z^2}{w_x^2(x)}} \cos^2(kx) + V_y e^{-2\frac{x^2+z^2}{w_y^2(y)}} \cos^2(ky) + V_z e^{-2\frac{x^2+y^2}{w_z^2(z)}} \cos^2(kz) \quad (4.3)$$

where  $V_{x,y,z}$  collects the pre-factors from Equation A.10 and Equation 5.2. Because of their low kinetic energy, cold atoms will only sample the bottom regions of the potential, and so the Gaussian intensity envelope may be expanded to second order in  $\mathbf{r}$  about the potential minimum:

$$V_{\text{latt}}(\mathbf{r}) = V_x \cos^2(kx) + V_y \cos^2(ky) + V_z \cos^2(kz) + \frac{m}{2} (\omega_x^2 x^2 + \omega_y^2 y^2 + \omega_z^2 z^2) \quad (4.4)$$

where  $\omega_{x,y,z}$  are the trapping frequencies of the effective harmonic trap:

$$\omega_x^2 = \frac{4}{m} \left( \frac{V_y}{w_y^2} + \frac{V_z}{w_z^2} \right) \quad (4.5)$$

and  $\omega_{y,z}^2$  are similarly obtained through cyclic permutation.

### 4.1.1 Lattice oscillation frequency and zero-point corrections

For sufficiently deep lattice depths we may define a lattice oscillation frequency at  $\mathbf{r} = 0$  by expanding the cosinusoidal terms in Equation 5.4 to second order:

$$\omega_{\text{latt},x} = \sqrt{V_x \frac{2k^2}{m}}, \quad (4.6)$$

and similarly for  $\omega_{\text{latt},y}$  and  $\omega_{\text{latt},z}$ . Away from  $\mathbf{r} = 0$ , the lattice oscillation frequency is reduced by the square root of the Gaussian intensity profile:

$$\omega_{\text{latt},z}(\mathbf{r}) = \omega_{\text{latt},z} e^{-\frac{x^2+y^2}{w_z^2(z)}} \quad (4.7)$$

$$\approx \omega_{\text{latt},z} \left( 1 - \frac{x^2+y^2}{w_z^2(z)} \right). \quad (4.8)$$

This causes a reduction in the ground state energy  $E_{\text{GS}} = \hbar/2(\omega_{\text{latt},x} + \omega_{\text{latt},y} + \omega_{\text{latt},z})$  away from the centre of the beam, with a corresponding reduction in the squared effective harmonic trap oscillation frequency  $\omega_x^2$  defined in Equation 5.5 by an amount:

$$\omega_{\text{anti},y}^2 + \omega_{\text{anti},z}^2 = \frac{2}{mw_y^2} \sqrt{V_y E_R} + \frac{2}{mw_z^2} \sqrt{V_z E_R}, \quad (4.9)$$

where  $E_R = (\hbar k)^2/2m$  is the recoil energy. The squared - and corrected - effective trap oscillation frequencies for a red-detuned optical lattice are then:

$$\omega_x^2 = \frac{2}{m} \left( \frac{2V_y - \sqrt{V_y E_R}}{w_y^2} + \frac{2V_z - \sqrt{V_z E_R}}{w_z^2} \right) \quad (4.10)$$

and  $\omega_{y,z}^2$  are obtained through cyclic permutation of indices.

The underlying harmonic confinement is unavoidable when creating optical lattices from red-detuned Gaussian beams. This may at first appear to present a problem for cold atom simulations of condensed matter materials where harmonic confinement is absent. In fact, the harmonic confinement is another parameter that may be tuned in order to observe different phases of the Hubbard model *in a single sample*. This is possible owing to the local variation of the chemical potential:

$$\mu_{\text{LDA}} = \mu - \frac{m}{2} (\omega_x^2 x^2 + \omega_y^2 y^2 + \omega_z^2 z^2). \quad (4.11)$$

Equation 5.11 expresses the local density approximation (LDA), valid when the kinetic energy may be ignored and the the harmonic energy varies slowly. Tuning of  $\mu_{\text{LDA}}$  is possible using a

combination of both red and blue Gaussian beams [17], Hermite-Gauss beams [139], and with spatial light modulators [140]. We will see in Section 5.6 the role that the harmonic confinement plays in determining the system behaviour. However, we first examine the Eigenstates and Eigenvalues of an atom in a homogenous lattice potential.

## 4.2 Band Structure

The Schrödinger equation that governs the behaviour of an atom in a one dimensional periodic potential along  $\mathbf{x}$  is given by:

$$\hat{H}_0 \phi_q^{(n)} = E_q^{(n)} \phi_q^{(n)}, \quad (4.12)$$

where the Hamiltonian is:

$$\hat{H}_0 = \frac{\hat{p}^2}{2m} + V_{\text{latt}}(x). \quad (4.13)$$

Because the lattice is separable along the three spatial directions, we are justified in considering the one-dimensional case and combining solutions in order to obtain the three-dimensional case. The solutions to Equation 5.12 are the Bloch functions [141], which can be written as the product of a function  $u_q^{(n)}$  that has the same periodicity as the lattice potential  $V_{\text{latt}}(x)$ , and the phase factor  $e^{iqx/\hbar}$ :

$$\phi_q^{(n)} = e^{iqx/\hbar} u_q^{(n)}. \quad (4.14)$$

Here,  $q$  labels the quasi-momentum and  $n$  is the band index. What these two quantities represent will become apparent below. First, we insert  $\phi_q^{(n)}$  into Equation 5.12 in order to find a Schrödinger equation for the periodic function  $u_q^{(n)}$ . Doing so, we find:

$$\hat{H}'_0 u_q^{(n)} = E_q^{(n)} u_q^{(n)} \quad (4.15)$$

with

$$\hat{H}'_0 = \frac{(\hat{p}^2 + q^2)^2}{2m} + V_{\text{latt}}(x). \quad (4.16)$$

As  $\hat{H}'_0$  is a functional of the momentum operator  $\hat{p}$ , it is useful to Fourier transform the position dependent functions  $u_q^{(n)}$  and  $V_{\text{latt}}(x)$ . Because these functions are periodic with the

fundamental spatial frequency  $2k$ , this may be done as a discrete series:

$$V_{\text{latt}}(x) = \sum_r V_r e^{i2rkx} \quad (4.17)$$

$$u_q^{(n)} = \sum_l c_l^{(n,q)} e^{i2lkx}. \quad (4.18)$$

We can easily evaluate Equation 5.17 for the lattice potential given that  $V_{\text{latt}}(x) = V_{\text{latt}} \cos^2(kx) = V_{\text{latt}}(e^{i2kx} + e^{-i2kx} + 2)/4$ . That is, there are only three non-zero Fourier amplitudes  $V_r$ :

$$V_1 = V_{-1} = V_{\text{latt}}/4, \quad V_0 = V_{\text{latt}}/2. \quad (4.19)$$

Furthermore, since  $V_0$  represents only a constant energy offset, we may set it equal to zero to simplify matters. We may now substitute the Fourier representations of  $u_q^{(n)}$  and  $V_{\text{latt}}(x)$  into the Schrödinger equation for  $\hat{H}'_0$  using Equation 5.16:

$$\sum_l \frac{(2\hbar kl + q)^2}{2m} c_l^{(n,q)} e^{i2lkx} + \frac{V_{\text{latt}}}{4} \sum_{l'} c_{l'}^{(n,q)} \left( e^{i(l'+1)2kx} + e^{i(l'-1)2kx} \right) = E_q^{(n)} \sum_l c_l^{(n,q)} e^{i2lkx} \quad (4.20)$$

Because  $e^{i2lkx}$  forms an orthogonal basis of plane waves, we can create a set of linear equations for the coefficients  $c_l^{(n,q)}$  by collecting all terms in front of plane waves that have the same spatial frequency  $2lk$ . Inspecting Equation 5.20, we can see that this sets a constraint on what the index  $l'$  can be, specifically  $l' = l \pm 1$ . With this substitution, we can rewrite Equation 5.20 as:

$$\sum_l \left( (2l + q/\hbar k)^2 E_R - E_q^{(n)} \right) c_l^{(n,q)} + V_{\text{latt}}/4 \left( c_{l-1}^{(n,q)} + c_{l+1}^{(n,q)} \right) = 0. \quad (4.21)$$

The index  $l$  represents the contributions from  $2lk$  spatial frequency waves. Inspecting Equation 5.21, we can see that higher  $|l|$  terms only add to an energy offset, and are thus unimportant when  $(2l + q/\hbar k)^2 E_R \gg V_{\text{latt}}/4$ . Most interesting lattice physics occurs below  $V_{\text{latt}} = 50 E_R$ , meaning that we may truncate the sum in Equation 5.21 at  $|l| = 5$ . When imaging, the lattice depth approaches  $V_{\text{latt}} = 500 E_R$ , and so we must sum all indices up to  $|l| = 15$ .

We have plotted solutions of  $E_q^{(n)}$  as a function of the quasi-momentum  $q$  in Figure 5.1 for different lattice depths  $V_{\text{latt}}$ . We see that for  $V_{\text{latt}} = 0$ , the dispersion relation is quadratic, just as one would expect for free particles. Thus, the quasi-momentum maps to the momentum  $p$ . For larger lattice depths, however, multiple gaps open up between the band energies, indexed by  $n$ , at the edge of the first Brillouin zone,  $q = \pm\hbar k$ . For lattice depths greater than  $V_{\text{latt}} = 20 E_R$ , the lowest energy bands begin to flatten, becoming harmonic oscillator-like with energies  $n\hbar\omega_{\text{latt}}$ .

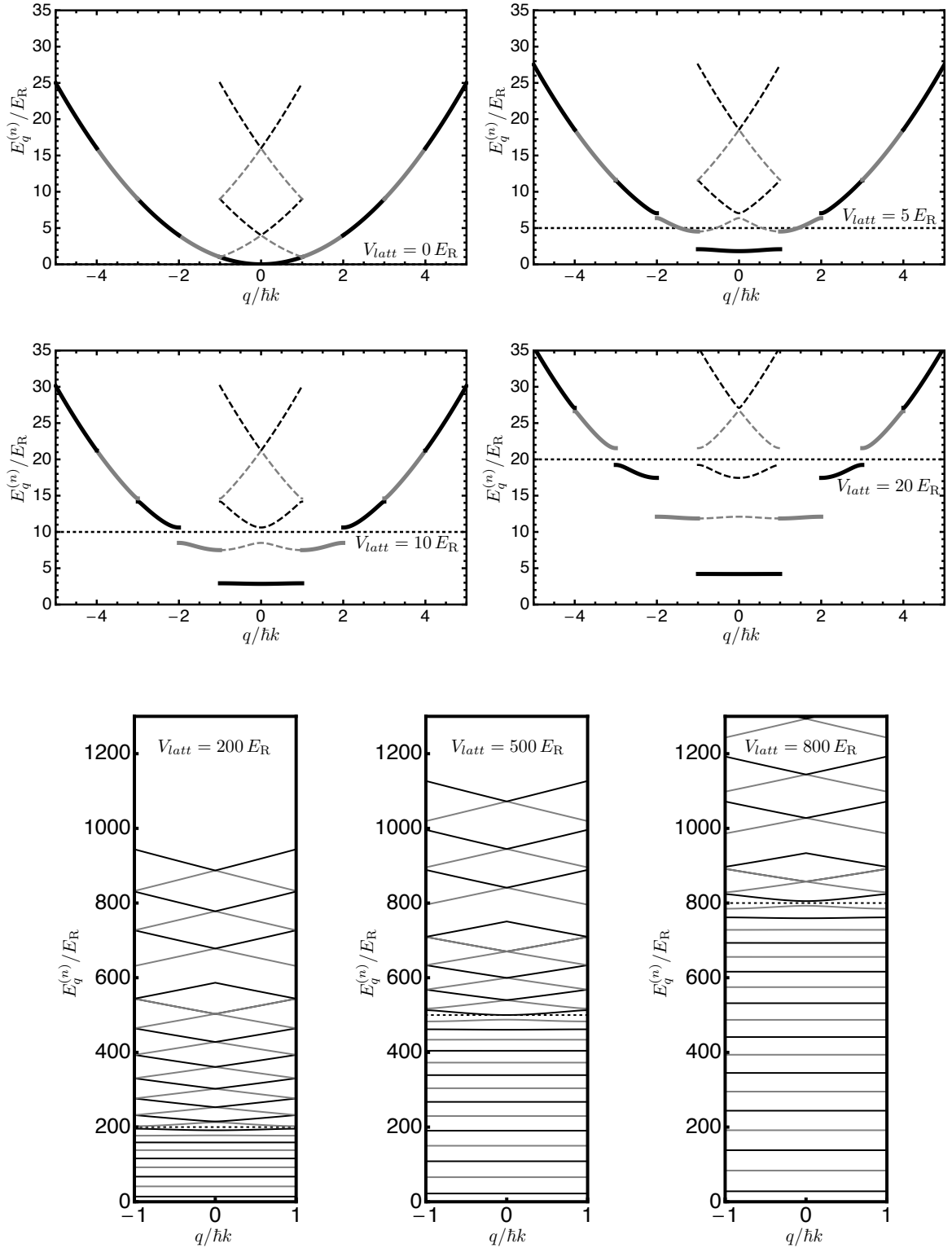


**Figure 4.1:**  $^{40}\text{K}$  Band Structure The top four plots show the band energies of an atom in a scientifically interesting range of optical lattice potential depths. The dashed lines show the band energies in the reduced zone scheme. The horizontal dotted line indicates the optical lattice depth for each plot. The bottom three plots show the calculated band energies in a very deep lattice.

### 4.3 Wannier functions

For deeper lattices, tunnelling between sites is suppressed and atoms become more and more localized. In this case, it is helpful to work in a basis of orthogonal, localized *Wannier* states. The Wannier states are made up of a superposition of Bloch states, and are given by:

$$w^{(n)}(x - x_i) = \frac{1}{\sqrt{M}} \sum_q e^{-iqx_i/\hbar} \phi_q^{(n)} \quad (4.22)$$

$$= \frac{1}{\sqrt{M}} \sum_q e^{-iq(x-x_i)/\hbar} u_q^{(n)}, \quad (4.23)$$

where  $M$  is the number of lattice sites, and the phase factor  $e^{-iq(x-x_i)/\hbar}$  ensures that we have constructive interference at the lattice site  $x_i$ . Recalling the Fourier representation of  $u_q^{(n)}$  presented in Equation 5.18, we may write  $w^{(n)}(x - x_i)$  in terms of the coefficients  $c_l^{(n,q)}$  that we solved for in Equation 5.21:

$$w^{(n)}(x - x_i) = \frac{1}{\sqrt{M}} \sum_q e^{-iq(x-x_i)/\hbar} \sum_l c_l^{(n,q)} e^{i2lkx}. \quad (4.24)$$

The quasi-momentum takes on discrete values between  $q = \pm\hbar k$  with a step-size determined by the number of lattice sites. The Wannier states become approximate Eigenstates of the system in the deep-lattice limit when the lowest bands flatten, becoming harmonic oscillator-like. In this case, Wannier functions approach the Gaussian ground-state harmonic oscillator functions.

### 4.4 Fermi-Hubbard model

In 1998, it was proposed that atoms loaded into the lowest band of an optical lattice could realize the Hubbard model [42]. The Hubbard model is the simplest model that describes the competition between kinetic and interaction energies of particles in a lattice potential. In the field of cold atoms, it has been used to explain the transition between superfluid and insulating states of bosons in an optical lattice [138], the analogous metallic-insulator transitions in fermions [16, 17], as well as providing a starting point for investigating the effect of disorder [51] and spin interaction effects [142, 11]. Cold atoms are able to faithfully emulate the Hubbard model owing to the short-range, contact nature of atom-atom interactions. In the following, we derive the Hubbard model starting from a second quantized form of the Hamiltonian and by then applying the simplifications that our cold atoms system allows.

The Hamiltonian for our system is:

$$\hat{H} = \hat{H}_0 + \hat{H}_{\text{int}} + \hat{H}_{\text{trap}}, \quad (4.25)$$

where

$$\hat{H}_0 = \sum_{\sigma} \int d^3r \hat{\psi}_{\sigma}^{\dagger}(\mathbf{r}) \left( -\frac{\hbar^2}{2m} \nabla^2 + V_{\text{latt}}(\mathbf{r}) \right) \hat{\psi}_{\sigma}(\mathbf{r}) \quad (4.26)$$

$$\hat{H}_{\text{int}} = \frac{U_0}{2} \sum_{\sigma\sigma'} \int d^3r \hat{\psi}_{\sigma}^{\dagger}(\mathbf{r}) \hat{\psi}_{\sigma'}^{\dagger}(\mathbf{r}) \hat{\psi}_{\sigma'}(\mathbf{r}) \hat{\psi}_{\sigma}(\mathbf{r}) \quad (4.27)$$

$$\hat{H}_{\text{trap}} = \sum_{\sigma} \int d^3r \hat{\psi}_{\sigma}^{\dagger}(\mathbf{r}) V_{\text{trap}}(\mathbf{r}) \hat{\psi}_{\sigma}(\mathbf{r}). \quad (4.28)$$

In these equations,  $U_0 = 4\pi\hbar^2 a/m$  parametrizes the interaction energy and

$$V_{\text{trap}}(\mathbf{r}) = \frac{m}{2} (\omega_x^2 x^2 + \omega_y^2 y^2 + \omega_z^2 z^2) \quad (4.29)$$

is the underlying harmonic confinement discussed in Section 5.1.1. The Hamiltonian has been written in terms of field operators  $\hat{\psi}_{\sigma}^{\dagger}(\mathbf{r})$  ( $\hat{\psi}_{\sigma}(\mathbf{r})$ ) that create(annihilate) a particle with spin  $\sigma$  at position  $\mathbf{r}$ . We are interested in the localized states of the system and so it is helpful to expand the field operators in terms of the Wannier functions:

$$\hat{\psi}_{\sigma}(\mathbf{r}) = \sum_n \sum_i \hat{b}_{i\sigma} w^{(n)}(\mathbf{r} - \mathbf{r}_i). \quad (4.30)$$

If we restrict ourselves to the lowest band of the optical lattice, Equation 5.30 becomes:

$$\hat{\psi}_{\sigma}(\mathbf{r}) = \sum_i \hat{b}_{i\sigma} w(\mathbf{r} - \mathbf{r}_i), \quad (4.31)$$

where  $w(\mathbf{r} - \mathbf{r}_i) = w^{(1)}(\mathbf{r} - \mathbf{r}_i)$  in order to simplify notation. The tunnelling energy can be written in terms of the Wannier functions:

$$J_{ij} \equiv - \int d^3r w^*(\mathbf{r} - \mathbf{r}_i) \left( -\frac{\hbar^2}{2m} \nabla^2 + V_{\text{latt}}(\mathbf{r}) \right) w(\mathbf{r} - \mathbf{r}_j). \quad (4.32)$$

We can make some additional simplifications. The tight-binding limit, valid when the lattice depth is greater than a few recoil energies, allows us to neglect tunnelling to all but nearest-neighbour sites. Also, we may neglect inter-site interactions due to the energy dominance of on-site interactions between neutral atoms. With these simplifications, the Hamiltonian in

Equation 5.25 may be written in terms of the parameters  $J$ ,  $U$ , and  $\epsilon_i$ :

$$J \equiv - \int d^3r w^*(\mathbf{r}) \left( -\frac{\hbar^2}{2m} \nabla^2 + V_{\text{latt}}(\mathbf{r}) \right) w^*(\mathbf{r} - a\hat{\mathbf{x}}) \quad (4.33)$$

$$U \equiv U_0 \int d^3r |w^*(\mathbf{r} - \mathbf{r}_i)|^4 \quad (4.34)$$

$$\epsilon_i \equiv \int d^3r |w^*(\mathbf{r} - \mathbf{r}_i)|^2 V_{\text{trap}}(\mathbf{r}) \approx V_{\text{trap}}(\mathbf{r}_i), \quad (4.35)$$

where  $a$  is the lattice constant, and we have made the approximation in Equation 5.35 due to the slow variation of  $V_{\text{trap}}(\mathbf{r})$  compared with  $w^*(\mathbf{r} - \mathbf{r}_i)$ . The Hamiltonian is then:

$$\hat{H} = -J \sum_{\sigma} \sum_{\langle i,j \rangle} \hat{b}_{i\sigma}^{\dagger} \hat{b}_{j\sigma} + \frac{U}{2} \sum_{\sigma\sigma'} \sum_i \hat{b}_{i\sigma}^{\dagger} \hat{b}_{i\sigma'}^{\dagger} \hat{b}_{i\sigma'} \hat{b}_{i\sigma} + \sum_{\sigma} \sum_i \epsilon_i \hat{b}_{i\sigma}^{\dagger} \hat{b}_{i\sigma}. \quad (4.36)$$

We have used the notation  $\langle i, j \rangle$  to refer to nearest neighbour tunnelling between sites  $i$  and  $j$ . A competition amongst the tunnelling  $J$ , interaction  $U$ , and harmonic  $\epsilon_i$  energies will determine the behaviour of the system. For instance, when  $U$  is large compared with  $J$ , the Hamiltonian is diagonalized in the number-state (Fock) basis - i.e. atoms tend to be localized.

#### 4.4.1 Tunnelling and bandwidth

There is an intimate connection between the tunnelling energy  $J$  and the width of a Bloch energy band  $E_q$ . This becomes evident when substituting the representation of the Wannier function in terms of Bloch states described in Equation 5.22 into Equation 5.32, the equation defining  $J_{ij}$ . We do this in order to make use of the Eigenvalue equation for  $\hat{H}_0$ , described in Equation 5.12, which is diagonal in the Bloch states. With this substitution, we get an equivalent expression for the tunnelling energy:

$$J_{ij} = -\frac{1}{M} \sum_q e^{-i(\mathbf{r}_j - \mathbf{r}_i)q} E_q, \quad (4.37)$$

where the quasi-momentum sum is taken over the first Brillouin zone. We can then write  $J_{ij}$  as a Fourier series:

$$\sum_i J_{ij} e^{i(\mathbf{r}_j - \mathbf{r}_i)q} = -\frac{1}{M} \sum_{q'} \sum_i e^{i(\mathbf{r}_j - \mathbf{r}_i)q} e^{-i(\mathbf{r}_j - \mathbf{r}_i)q'} E_{q'}. \quad (4.38)$$

Making use of the identity  $\sum_i e^{i(q' - q)\mathbf{r}_i} = M\delta_{q,q'}$ , and working in the tight-binding limit  $(\mathbf{r}_i - \mathbf{r}_j) = \pm a$ , we can solve for the energy  $E_q$ :

$$E_q = -2J \cos(qa). \quad (4.39)$$

Inspecting Equation 5.39, we can see that  $J$  is related to the energy bandwidth:

$$J = \frac{|E_{\pm\hbar k} - E_0|}{4}. \quad (4.40)$$

Within the tight-binding limit, an analytical expression for  $J$  may be calculated by solving the one-dimensional Mathieu equations [143]:

$$J = \frac{4E_R}{\sqrt{\pi}} \left( \frac{V_{\text{latt}}}{E_R} \right)^{3/4} e^{-2\sqrt{V_0/E_R}}. \quad (4.41)$$

#### 4.4.2 Analytical expression for $U$

An analytical expression may also be calculated for  $U$  in the tight-binding limit when Wannier functions may be approximated as Gaussians. Using the additional fact that the 3D Wannier functions are separable along the three spatial dimensions:

$$w(\mathbf{r}) = w(x)w(y)w(z), \quad (4.42)$$

we may write Equation 5.34 as

$$U = U_0 \left( \int_{-\infty}^{\infty} dx |w^*(x - x_i)|^4 \right)^3. \quad (4.43)$$

Then, using the harmonic oscillator ground state function  $(m\omega_{\text{latt}}/\pi\hbar)^{1/4} e^{-m\omega_{\text{latt}}x^2/2\hbar}$  in place of the Wannier function, the interaction energy is:

$$U = U_0 \left( \frac{m\omega_{\text{latt}}}{\hbar} \right)^{3/2} = U_0 \left( \frac{k^2}{2\pi} \sqrt{\frac{V_{\text{latt}}}{E_R}} \right)^{3/2}. \quad (4.44)$$

## 4.5 Double-well example

We can gain insight into the behaviour of the the Fermi-Hubbard model by looking at double-well system with two atoms: one with spin up  $|\uparrow\rangle$ , and one with spin down  $|\downarrow\rangle$ . This minimal model has an analytic solution, yet is not too trivial to capture the basic features of the Fermi-Hubbard model. Note that we exclude the harmonic contribution to the Hamiltonian  $\epsilon_i$  in this example. We start by making use of the anti-commutation relations between the fermionic field operators  $\{\hat{b}_{i\sigma}, \hat{b}_{j\sigma'}^\dagger\} = \delta_{\sigma,\sigma'}\delta_{i,j}$  and write Equation 5.36 as:

$$\hat{H}_{\text{FH}} = -J \sum_{\sigma} \sum_{\langle i,j \rangle} \hat{b}_{i\sigma}^\dagger \hat{b}_{j\sigma} + U \sum_i \hat{n}_{i\uparrow} \hat{n}_{i\downarrow} + \sum_i \epsilon_i (\hat{n}_{i\uparrow} + \hat{n}_{i\downarrow}). \quad (4.45)$$

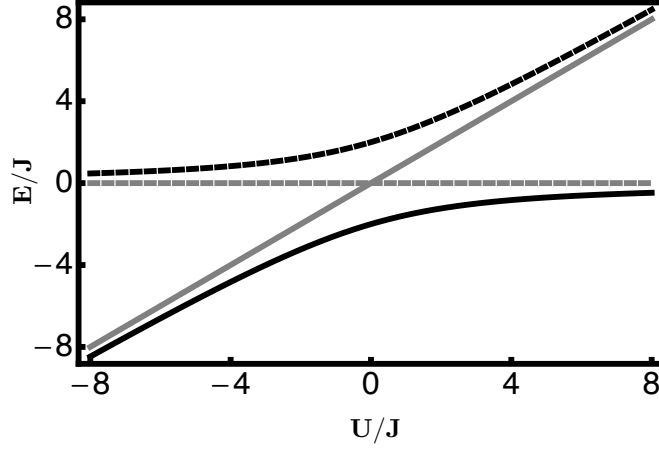


**Figure 4.2: Energy spectrum of double-well Fermi Hubbard Hamiltonian** The Eigenenergies are plotted versus the dimensionless interaction parameter  $U/J$ :  $E_1$  (gray, dashed),  $E_2$  (gray, solid),  $E_3$  (black, dashed),  $E_4$  (black, solid). It is evident that the ground state of the system is  $|\psi_4\rangle$ .

where  $\hat{n}_{i\uparrow(\downarrow)}$  is the number operator for up(down) spin atoms at site  $i$ . Then, restricting ourselves to two sites ( $i = 1, 2$ ), we can write down the double-well Fermi-Hubbard model:

$$\hat{H}_{\text{DW}} = -J \left( \hat{b}_{1\uparrow}^\dagger \hat{b}_{2\uparrow} + \hat{b}_{1\downarrow}^\dagger \hat{b}_{2\downarrow} + \hat{b}_{2\uparrow}^\dagger \hat{b}_{1\uparrow} + \hat{b}_{2\downarrow}^\dagger \hat{b}_{1\downarrow} \right) + U (\hat{n}_{1\uparrow} \hat{n}_{1\downarrow} + \hat{n}_{2\uparrow} \hat{n}_{2\downarrow}). \quad (4.46)$$

The Hamiltonian  $\hat{H}_{\text{DW}}$  may be cast in matrix form if we work in the basis of the Fock states  $\{|\uparrow\downarrow, 0\rangle, |\uparrow, \downarrow\rangle, |\downarrow, \uparrow\rangle, |0, \downarrow\uparrow\rangle\}$ , where  $|\uparrow, \downarrow\rangle$  would describe the state with a spin up atom in site  $i = 1$  and a spin down atom in site  $i = 2$ :

$$\hat{H}_{\text{DW}} = \begin{pmatrix} U & -J & -J & 0 \\ -J & 0 & 0 & -J \\ -J & 0 & 0 & -J \\ 0 & -J & -J & U \end{pmatrix}$$

The Eigenvalues of  $\hat{H}_{\text{DW}}$  can be readily obtained, and are:

$$E_1 = 0 \quad (4.47)$$

$$E_2 = U \quad (4.48)$$

$$E_{3/4} = \frac{U}{2} \pm \sqrt{4J^2 + \frac{U^2}{4}}, \quad (4.49)$$

with the corresponding Eigenstates:

$$|\psi_1\rangle \propto |\uparrow, \downarrow\rangle - |\downarrow, \uparrow\rangle \quad (4.50)$$

$$|\psi_2\rangle \propto |\uparrow\downarrow, 0\rangle - |0, \downarrow\uparrow\rangle \quad (4.51)$$

$$|\psi_{3/4}\rangle \propto |\uparrow\downarrow, 0\rangle + |0, \downarrow\uparrow\rangle + \left( U/4J \mp \sqrt{1 + (U/4J)^2} \right) (|\uparrow, \downarrow\rangle + |\downarrow, \uparrow\rangle). \quad (4.52)$$

We can see that  $|\psi_1\rangle$  corresponds to an anti-symmetric spin state with atoms localized in separate wells. On the other hand,  $|\psi_2\rangle$  corresponds to an anti-symmetric spin state where the spin up and spin down atoms sit together in either site 1 or site 2, picking up an interaction energy  $U$ . The Eigenstates  $|\psi_3\rangle$  and  $|\psi_4\rangle$  are a superposition of all the basis states and correspond to the largest and smallest energy states of the system, respectively. The ground state of the system,  $|\psi_4\rangle$ , is symmetric under spin exchange. It therefore must have an anti-symmetric spatial wave function. We can see by looking at a plot of  $E_4$  v.s.  $U/J$  in Figure 5.2 that  $|\psi_4\rangle$  behaves similarly to  $|\psi_4\rangle$  when  $U$  is large and negative. That is, the ground state is the state with atoms predominantly in the same well, with a small energy correction that lowers the energy by  $4J^2/U$  due to the allowance of a spin exchange process. On the other hand, when  $U$  is large and positive,  $|\psi_4\rangle$  becomes similar in character to  $|\psi_1\rangle$ , with atoms localized in separate sites. Again,  $|\psi_4\rangle$  is lower in energy than the localized state  $|\psi_1\rangle$  by the exchange energy  $4J^2/U$ . The exchange energy can be understood as the the energy associated with two spins exchanging position, requiring two tunnelling events (and the associated  $J^2$  tunnelling energy) and the tunnelling to a site detuned by  $\pm U$  in energy due to an intermediate double occupancy. The factor of 4 arises because each tunnelling process can occur in one of two different ways.

We also see the origins of the bandwidth from this simple model. Inspecting Figure 5.2 at the  $U = 0$  point, the difference between the largest ( $E_3$ ) and smallest ( $E_4$ ) energies is  $4J$ . This defines the bandwidth in the double-well model, consistent with the bandwidth for the many-site Fermi-Hubbard model derived in Equation 5.40.

### 4.5.1 The Heisenberg model as a limiting case of the Hubbard model

In the two-spin double-well system just described, we saw that in the  $U/J \rightarrow \infty$  limit, the ground state exhibited antiferromagnetic order: an alternating arrangement of up and down spins. Admittedly, this anti-ferromagnetic order was rather trivial: any state in which the atoms were localized corresponded to a state with staggered spin direction. However, we can show that antiferromagnetic ordering remains a feature of the many-site Fermi-Hubbard model at half-filling (that is, with a system that is filled with an average of one atom per site) in the  $U \gg J$  limit. In this limit, we show that the Fermi-Hubbard model reduces to the Heisenberg

model:

$$\hat{H}_{\text{Heisenberg}} = J_{\text{ex}} \sum_{\langle i,j \rangle} \hat{\mathbf{S}}_i \cdot \hat{\mathbf{S}}_j. \quad (4.53)$$

The Heisenberg model describes the interaction between spins on neighbouring sites  $i$  and  $j$ . The energy of the system is lowered when the spins are antiferromagnetically aligned. We can see this by investigating the double well Heisenberg model, which has the Eigenstates:

$$|\psi_s\rangle \propto |\uparrow, \downarrow\rangle - |\downarrow, \uparrow\rangle \quad (4.54)$$

$$|\psi_t^+\rangle \propto |\uparrow, \uparrow\rangle \quad (4.55)$$

$$|\psi_t^0\rangle \propto |\uparrow, \downarrow\rangle + |\downarrow, \uparrow\rangle \quad (4.56)$$

$$|\psi_t^-\rangle \propto |\downarrow, \downarrow\rangle. \quad (4.57)$$

Using the fact that  $\hat{\mathbf{S}}_1 \cdot \hat{\mathbf{S}}_2 = 1/2 (\hat{S}_1^+ \hat{S}_2^- + \hat{S}_1^- \hat{S}_2^+) + \hat{S}_1^z \hat{S}_2^z$ , we can determine the corresponding Eigenvalues for the singlet and triplet states:

$$E_s = -\frac{3J_{\text{ex}}}{4} \quad (4.58)$$

$$E_t = \frac{J_{\text{ex}}}{4}, \quad (4.59)$$

and see that they are separated in energy by  $J_{\text{ex}}$ .

For comparison, we can do second order perturbation theory on  $\hat{H}_{\text{DW}}$ . We do this in the  $U/J \rightarrow \infty$  limit, where the Hamiltonian can be written in terms of the small parameter  $J/U$ :

$$\hat{H}_{\text{DW}} = U \left( \hat{H}_{\text{U}} + J/U \hat{H}_{\text{J}} \right), \quad (4.60)$$

where  $\hat{H}_{\text{U}}$  is the interaction (second) term and  $\hat{H}_{\text{J}}$  is the tunnelling (first) term in Equation 5.46. We do perturbation theory on  $|\psi_1\rangle$ , the ground state of  $\hat{H}_{\text{U}}$ , and find a second order energy correction:

$$\Delta E^{(2)} = -\frac{4J^2}{U}. \quad (4.61)$$

Comparing our results from  $U/J \rightarrow \infty$  perturbation theory on the Fermi-Hubbard model to the diagonalization of the Heisenberg model, we notice that the Eigenstates and Eigenvalues are the same, after identifying the super-exchange energy:

$$J_{\text{ex}} = -\frac{4J^2}{U}. \quad (4.62)$$

Thus the Fermi-Hubbard reduces to the Heisenberg model in this limit. The exchange energy also defines the Néel temperature,  $T_N = J_{\text{ex}}/k_B$ , the temperature at which a transition to an antiferromagnetically ordered state occurs in the  $U \gg J$  limit. In the  $U < J$  region, it turns out that there is also an instability towards the Néel state, and the transition temperature varies as  $T_N \approx J e^{-\sqrt{J/U}}$  [144]. Because  $T_N$  decreases with  $U/J$  in the  $U \gg J$  limit and increases with  $U/J$  in the  $U < J$  region, we might guess that it would reach a maximum at a few  $U/J$ . Monte-Carlo studies confirm this estimate, predicting a maximum Néel temperature at  $U/J = 14$  [145].

## 4.6 Metal-Insulator transition in the $U \rightarrow 0$ limit.

In previous sections, we have explored the behaviour of atoms in a periodic potential under certain simplifying conditions that allowed us to notice different aspects of the system. For instance, in Section 5.2, we saw that the state of an atom in a purely periodic potential may be written in a basis of de-localized Bloch waves. In Section 5.3, we saw that localized Wannier states form a more natural basis when the lattice depth becomes deeper than a few  $E_R$ . While we were able to define the Fermi-Hubbard model in Section 5.4 in terms of these Wannier states, we did not solve for the Eigenvalues and Eigenstates, settling instead for a solution of the simple double well model in Section 5.5.

In this section, we calculate the energy spectrum and states of a system described by the 1D Hamiltonian:

$$\hat{H} = -\frac{\hbar^2}{2m}\nabla^2 + V_{\text{latt}}(x) + \frac{1}{2}m\omega_x^2 x^2 \quad (4.63)$$

Notice that this is the same Hamiltonian - albeit in position-space representation - as described in Equation 5.25, minus the interaction term. We present a 1D Hamiltonian to solve because solutions to periodic and Harmonic potentials are separable. This Hamiltonian is important because it is relatively simple to experimentally implement, exactly calculable, and describes interesting metallic - insulating phase transition physics. Physically, we may think of Equation 5.63 as describing either a spin-polarized cloud of fermions, or a system of spin-up and spin-down fermions where a Feshbach field has tuned the  $s$ -wave scattering length to zero.

We numerically diagonalize Equation 5.63 and plot the solutions to the Eigenvalue equation

$$\hat{H}\psi^i(x) = E_i\psi^i(x) \quad (4.64)$$

in Figure 5.3. In contrast to Figure 5.1, we do not observe a gap in the energy spectrum between

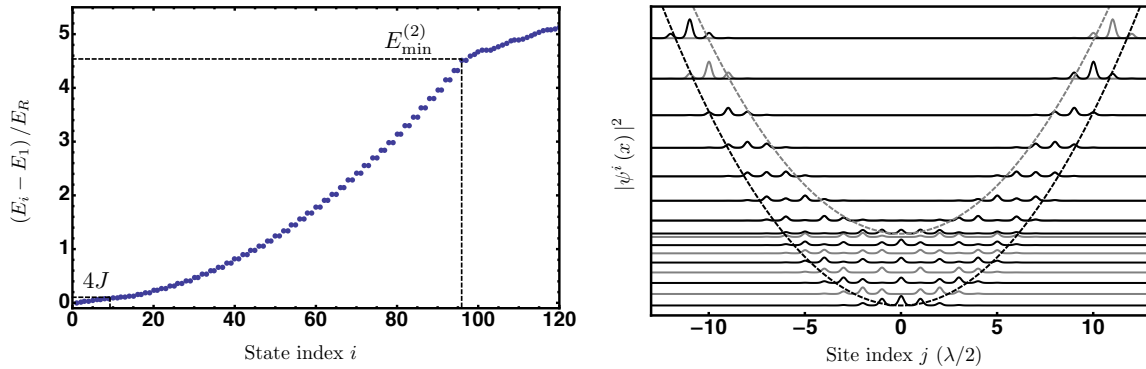


**Figure 4.3: Eigenvalues and Eigenstates of a  $10E_R$  optical lattice:** The plot on the left shows three different regions of behaviour in the energy spectrum. For  $E_i < 4J$ , corresponding to less than 10 atoms, the energy spectrum is linear. This is the harmonic oscillator region. For  $4J < E_i < E_{\min}^{(2)}$ , corresponding to atom numbers between 10 and 96, the energy spectrum is harmonic. This is the localized state region. For  $E_i > E_{\min}^{(2)}$ , corresponding to atoms numbers greater than 96, atoms start to fill a combination of second band harmonic oscillator states and first band localized states. The corresponding Eigenstates are plotted on the right, offset by their energies. We can see that the lowest states, the harmonic oscillator states, have probability densities spread across many lattice sites. This is in contrast to the higher lying, localized, states whose probability densities are centred on only a few sites. The black and grey dashed lines define the minimum and maximum allowed energies of the first band, offset by the harmonic energy.

different bands. This is due to the inclusion of the harmonic confinement term in Equation 5.63. In Figure 5.3, the energy increases linearly with the site index of (or, equivalently, the number of particles in) the system up to  $4J$ . The dispersion relation in this region,  $E \propto i$ , suggests that these are harmonic oscillator-like states, de-localized across lattice sites. If there are enough atoms in the system to populate energy levels above  $4J$ , then the dispersion relation becomes quadratic:  $E \propto i^2$ . Here, we have filled up all the energy levels in the band, with each additional atom increasing the system size, filling a newly available site. Once there are enough atoms to fill energies above  $E_{\min}^{(2)}$ , the dispersion relation is no longer quadratic. This defines the point at which second band states begin to be filled.

In order to see how these energies and state might manifest themselves in the observables of our local probe apparatus, we use the states  $\psi^{(i)}(x)$  to define the local filling probability at site  $j$  from state  $i$ :

$$\langle n_j^i \rangle = \int_{x_j}^{x_j+\lambda/2} |\psi^{(i)}(x)|^2 dx. \quad (4.65)$$

In order to calculate temperature-dependent quantities, we must include the Boltzmann factor:

$$P(E_i) = \frac{1}{1 + e^{(E_i - \mu)/k_B T}} \frac{1}{Z} \quad (4.66)$$

where  $Z = \sum_i e^{(\mu - E_i)/k_B T}$  is the partition function,  $\mu \equiv E_{i=N}$  is the chemical potential, and  $N$  is the number of atoms in our system. We may then define a filling probability at site  $j$  by summing over all states:

$$\langle n_j(T) \rangle = \frac{\sum_i P(E_i) \langle n_j^i \rangle}{Z}. \quad (4.67)$$

A plot of  $\langle n_j(T=0) \rangle$  v.s. lattice site index  $j$  for different  $N$  can be seen in Figure 5.4. We notice that when we do not have enough atoms in the system to fill states with energies at or above the bandwidth energy  $4J$ ,  $\langle n_j(T=0) \rangle < 1$ . When we have enough atoms to populate states above  $4J$ , but not enough to population states with energies at or above the minimum energy of the second band  $E_{\min}^{(2)}$ , then  $\langle n_j(T=0) \rangle = 1$ . When we have so many atoms that second band sites begin to be populated, then  $\langle n_j(T=0) \rangle > 1$ . We hasten to add the obvious: that our single-site imaging apparatus will be able to directly measure the local filling, allowing for the position-space measurement of band populations.

Another quantity that is both useful for differentiating phase behaviour and directly mea-

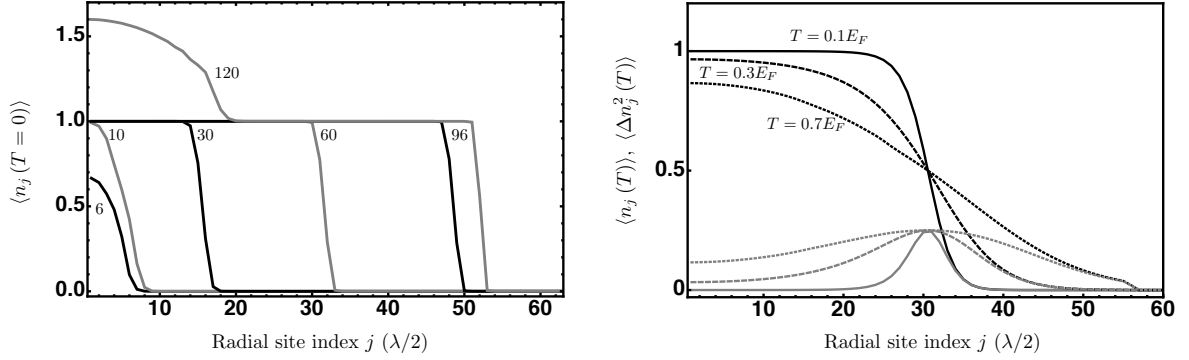


**Figure 4.4: Numerical simulation of site filling in a  $10E_R$  lattice** The left plot shows the zero temperature local filling density  $\langle n_j(T=0) \rangle$  as a function of the radial site index. We can see that when there are an insufficient number of atoms to fill states up to the band energy, the local filling fraction is less than 1. The filling fraction is equal to 1 when we have enough atoms to fill up the first band, but not so much that we start populating the second. The filling fraction rises above 1 when second band states begin to be populated. The plot on the right shows  $\langle n_j(T=0) \rangle$  (black lines) and  $\langle \Delta n_j^2(T) \rangle$  (grey lines) for 60 atoms at different temperatures:  $T = 0.1E_F$  (solid),  $T = 0.3E_F$  (dashed),  $T = 0.7E_F$  (dotted). We see that it becomes hard to distinguish Band insulating physics from a normal Fermi gas for temperatures above  $0.3E_F$ .

surable with a single site imaging  $j$  probe are the fluctuations in the local density:

$$\langle \Delta n_j^2(T) \rangle = \langle (n_j(T))^2 \rangle - \langle n_j(T) \rangle^2. \quad (4.68)$$

This quantity may be used alongside  $\langle n_j(T) \rangle$  to determine the local entropy:

$$s = -k_B \sum_i P(E_i) \ln P(E_i). \quad (4.69)$$

The local entropy is a useful quantity because it provides an intuitive way to distinguish phase behaviour in our system. We can see this by considering the case of a spin-polarized gas of Fermions with enough atoms to fill a single band. Near the centre of the system where insulating behaviour is prevalent, we expect only one atom per site, and so  $s/k_B \approx \ln 1 \approx 0$ . Farther away from the center, at a distance corresponding to a harmonic energy roughly equal to the chemical potential  $j \approx \sqrt{8\mu/m\omega_x^2\lambda^2}$ , the system is exhibiting metallic behaviour with either 1 or 0 atoms expected in each site. With two possible states in this region, the local entropy is  $s/k_B \approx \ln 2$ . At distances  $j \gg \sqrt{8\mu/m\omega_x^2\lambda^2}$ , the local density is expected to be zero, and so  $s/k_B \approx \ln 1 \approx 0$ , again. We can see in Figure 5.4 that  $\langle \Delta n_j^2(T) \rangle$  qualitatively follows  $s/k_B$ .

In Section 5.9 we discuss the experimental realization of a localized state of spin-polarized fermions in an optical lattice, measured using time-of-flight imaging.

## 4.7 Experimental creation of an optical lattice

The optical lattice is produced from light derived from the same amplified 100 kHz linewidth 1053.6 nm source as is used for the optical dipole trap. Light is directed to the optical lattice path or the optical dipole path using a motorized rotating wave plate and a polarizing beam splitter cube. We use AOMs to actively control the amount of optical lattice light using a PID feedback servo. Optical lattice light is coupled into a high-power fiber (PMJ-3AHCP-1064-6/125-5AS-2-1-SP) to clean up the spatial mode of the light and de-couple the thermally-dependent AOM deflection direction from the alignment of the lattice.

The three-dimensional optical lattice potential is created from the interference of three retro-reflected beam pairs. Light is focused onto the atoms to a waist of 60  $\mu\text{m}$  and 85  $\mu\text{m}$  for the horizontal and vertical lattice beams, respectively, using a 200 mm lens sitting just outside the science chamber. The beam is collimated with another 200 mm lens, reflected off of a dichroic mirror (DMSP850), and is then retro-reflected along the same path as the forward beam. We use an optical isolator to prevent back-coupling through the optical fiber. The optical lattice optics schematic is presented in Figure 5.5.

### 4.7.1 High power fiber coupling

Optical fibers are a convenient way to spatially filter and transport light. However, fiber-coupling high power optical beams of over 1W involves a set of challenges not present in lower power applications. One of these challenges is spontaneous Brillouin scattering (SBS). SBS is a process whereby an incident radiation field  $\mathbf{E}_1(z, t) = \mathbf{E}_{01}e^{i(k_1z - \omega t)} + c.c.$  scatters off of an acoustic density wave present in thermal equilibrium in the fiber  $\rho(z, t) = \langle \rho_0 \rangle + (\rho_0 e^{i(qz - \Omega t)} + c.c.)$ , resulting in a back-scattered radiation field  $\mathbf{E}_2(z, t) = \mathbf{E}_{02}e^{i(-k_2z - \omega t)} + c.c..$  Here,  $\langle \rho_0 \rangle$  is the equilibrium density value. The more power there is in the incident field, the more likely back-scattering is to occur. Any back-scattered radiation  $\mathbf{E}_2(z, t)$  will interfere with the incident field  $\mathbf{E}_1(z, t)$  to produce a standing wave intensity pattern. The standing wave intensity pattern causes density modulations in the fiber by a process of *electrostriction*, and these density modulations will in turn cause more radiation scattering. The process is phase-matched and so it exponentially builds upon itself above a certain threshold, limiting the amount of power that is able to be transmitted through the fiber.

The intensity threshold above which SBS becomes dominant can be estimated by solving



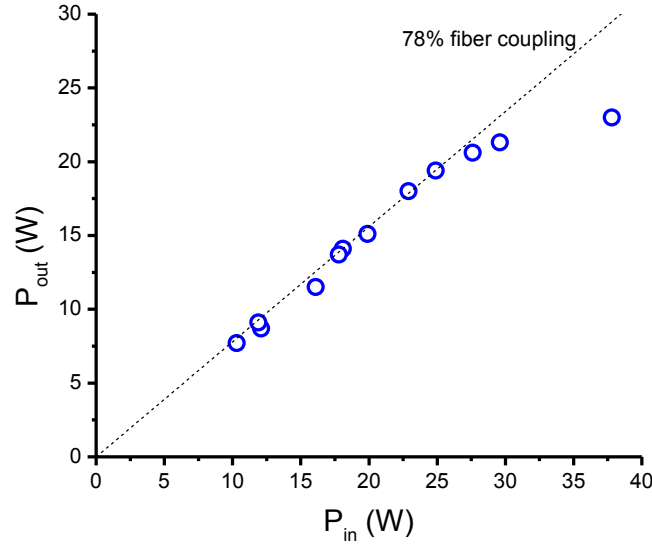


**Figure 4.6: High power fiber coupling** A plot showing the relationship between incident power  $P_{in}$  and transmitted power  $P_{out}$ . The incident power is related to the power in the fiber  $P_1$  via the efficiency that we are able to initially couple light into the fiber  $f_c$ :  $P_1 = f_c P_{in}$ . Accounting for the fiber coupling efficiency of  $f_c = 0.78$ , we measure a threshold power of approximately 25 W.

the coupled equations for the intensities [146]:

$$\frac{dI_1}{dz} = -g(\Omega) I_1 I_2 - \alpha_R I_1 \quad (4.70)$$

$$\frac{dI_2}{dz} = -g(\Omega) I_2 I_1 + \alpha_R I_2 \quad (4.71)$$

where  $\alpha_R$  is the loss coefficient in the fiber (3 dB/km for our fiber), and  $g(\Omega)$  is the SBS gain factor given by

$$g(\Omega) = g_0 \frac{(\Gamma_B/2)^2}{(\Omega_B - \Omega)^2 + (\Gamma_B/2)^2}. \quad (4.72)$$

$\Gamma_B$  is the rate at which acoustic phonons decay (typically  $2\pi \times 50$  MHz),  $\Omega_B = 2nv_s/\lambda$  is the doppler-shifted frequency of the Brillouin scattered field  $\mathbf{E}_2(z, t)$ ,  $n$  is the index of refraction and  $v_s$  is the velocity of sound in the fiber.  $\Omega_B$  is typically  $2\pi \times 10$  GHz. The resonance gain  $g_0$  is also a function of these parameters, and is given by:

$$g_0 = \frac{(n^2 - 1)^2 \omega^2}{nv_s c^3 \langle \rho_0 \rangle \Gamma_B}. \quad (4.73)$$

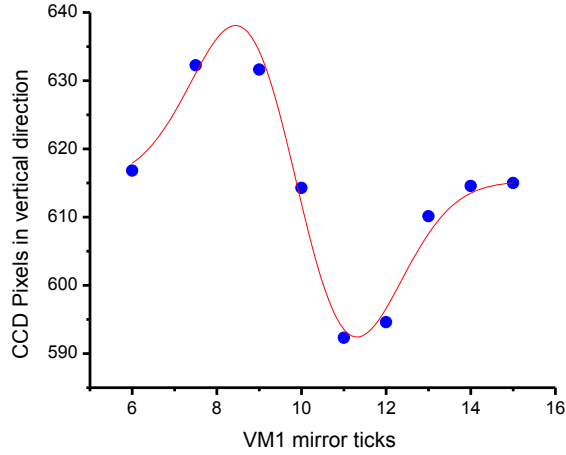


**Figure 4.7: Forward lattice beam alignment:** A forward propagating lattice beam (with retro beam blocked) is pulsed on for 1 ms at 250 mW. The plot here shows a scan of the vertical alignment of the beam. The resulting “dispersion” curve measures the force  $\mathbf{F} = -\nabla U$  imparted to the atoms by the beam in directions perpendicular to the imaging axis.

For optical fibers,  $g_0$  is typically  $5 \times 10^{-11} \text{m/W}$ . The threshold intensity  $I_{th}$  is dependent on an empirically determined constant  $C = 21$  [147], a polarization factor  $p$  which can vary between 1 and 2, as well as the gain factor  $g(\Omega)$  and the effective fiber length  $L_E$  which, for short fibers and small loss  $\alpha_R$ , is equal to the physical fiber length  $L$ :

$$I_{th} = \frac{Cp}{g(\Omega)L} \quad (4.74)$$

For a fiber of cross-sectional area  $30 \mu\text{m}^2$ , length  $L = 2 \text{m}$ , and  $p = 1$ , this corresponds to a power threshold of 6 W. This is to be compared to the 5 W that we would like to couple through for the dipole and lattice beams. Figure 5.6 shows the measured fiber coupling efficiency as a function of input power  $P_1$ . The amount of power able to be transmitted through the fiber is better than expected from Equation 5.74, perhaps as a result of imperfections in the polarization purity.

Whereas the Brillouin scattered radiation  $\mathbf{E}_2(z, t)$  is broadened by  $\Gamma_B$ , the incident light that is not Brillouin scattered remains narrow-band as long as Rayleigh scattering (loss) processes are small [146].

## 4.7.2 Optical lattice alignment

Atoms are loaded into the optical lattice from the crossed dipole trap after evaporation. The adiabatic criterion requires that this process be slow and controlled, so that atoms do not pick up any kinetic energy during the transfer that unduly heats them out of their low-entropy state.

This, in turn, requires that the optical lattice beams be well aligned to the cross-dipole trap at final evaporation powers. The optical lattice beam alignment proceeds in four steps for each beam pair: A coarse, then fine, alignment of the forward, then retro-reflected, beam.

The coarse alignment of the forward beam is accomplished by first taking an *in situ* absorption image of the atom cloud in the crossed dipole trap using a CCD camera focused to the atoms along the same axis as the lattice beam being aligned. The imaged cloud position is noted, and then the lattice beam can be aligned to the same position *ex situ*. This alignment step is requires only a single experimental run worth of time, and is made possible by the fact that we have incorporated dichroic optics into the optical lattice design that transmit imaging light, and reflect optical lattice light: see Figure 5.5.

Fine alignment of the forward beam is accomplished by pulsing it on for 1 ms at high power ( $\approx 250$  mW) immediately after release from the crossed-dipole trap. We use a  $^{87}\text{Rb}$  BEC for this procedure due to the inherent stiffness of the cloud, and make sure to block the retro-reflected lattice beam. When the forward beam is aligned, it will “blow-up” the cloud symmetrically, increasing its width, but not changing its centre-of-mass position. Conversely, a slightly mis-aligned beam will both “blow up” the cloud asymmetrically and push its centre-of-mass off to the side: see Figure 5.7.

After aligning the forward beam, we are ready to coarsely align the retro-reflected beam. This is done by maximizing the light coupled back through the optical isolator and out the rejection port. We can check whether there is any spatial overlap, and thus interference, of the forward and retro-reflected beams by pulsing them on for a few tens of  $\mu\text{s}$  at some tens of mW of power and observing whether or not atoms are diffracted by the lattice and have picked up an extra  $\hbar k$  of momentum. Quantitatively predicting how much the atoms should be diffracted by the lattice for a given power and pulse duration lies at the heart of the subsequent fine alignment process, and so we discuss it in detail in the following section.

### 4.7.3 Diffraction alignment

The diffraction alignment of an optical lattice beam involves the sudden turn-on, wait for a variable hold-time, then turn-off of the lattice potential. The amount of diffraction from the  $q = 0$  into the  $q = \pm 2\hbar k$  states varies sinusoidally with the wait time  $\tau$ . We explain why this is so by following the argument articulated in [148].

We begin with a BEC of  $^{87}\text{Rb}$  in a harmonic trap. We make the approximation that because the Thomas-Fermi radius of the BEC is much larger than the lattice spacing, the corresponding momentum spread of the BEC is small compared with that of atoms in the lattice, and we may approximate the state of the BEC as a plane wave  $|\phi_q\rangle$ . In fact, this argument suggest that

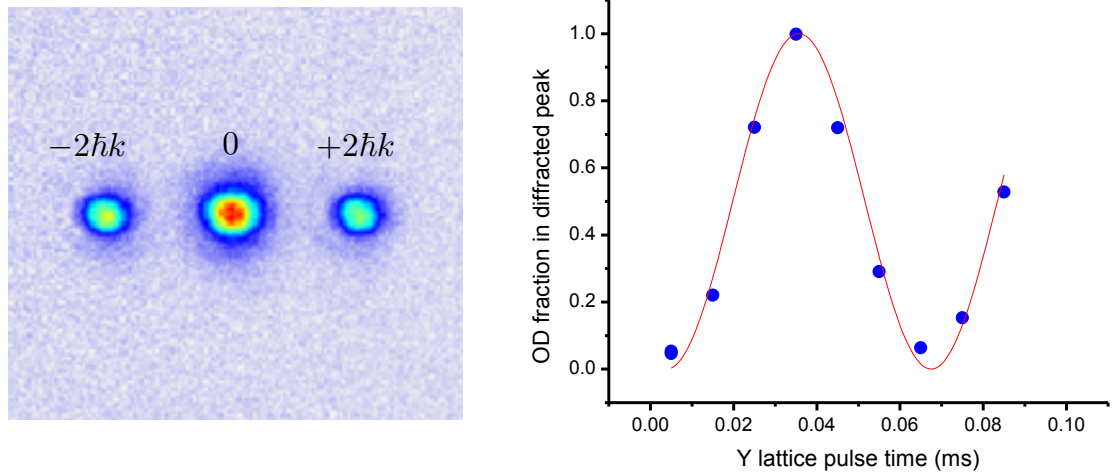


**Figure 4.8: Kaptiza-Dirac Alignment** The picture on the left shows a  $^{87}\text{Rb}$  BEC that has been partially diffracted by the  $\mathbf{y}$  lattice beam. The un-diffracted peak sits in the middle, whereas the diffracted satellite peaks have travelled an extra distance  $\pm\hbar kt/m$  in time  $t$  due to the  $\pm 2\hbar k$  of momentum imparted to them by the lattice. The picture on the right shows the OD fraction in the diffracted peaks as a function of the lattice pulse time. Fitting this gives a Kaptiza-Dirac period of  $\tau_{\text{KD}}=68\ \mu\text{s}$ . We may consult with the predicted  $\tau_{\text{KD}}$  in Figure 5.9 to determine a lattice depth of  $8E_R$ . If this equals the measured power in beam, then the lattice has been well aligned.

we may neglect the harmonic confinement for this particular problem altogether, using results calculated in Section 5.2. Therefore, upon sudden switch-on of the lattice, the plane-wave state may be written as a discrete sum of the Bloch states:

$$|\psi(t=0)\rangle = \sum_{n=0}^{\infty} |n, q\rangle \langle n, q | \phi_q\rangle. \quad (4.75)$$

After some wait time  $\tau$ , the state evolves, with each stationary Bloch state acquiring a phase:

$$|\psi(\tau)\rangle = \sum_{n=0}^{\infty} e^{-iE_q^{(n)}\tau/\hbar} |n, q\rangle \langle n, q | \phi_q\rangle. \quad (4.76)$$

The lattice is then suddenly switched off. This action projects the state back into the plane-wave basis. However, because the Bloch states have the same spatial periodicity as the lattice, and thus momentum contributions at integer multiples of the reciprocal-lattice vector  $2\hbar k$ , we must allow for non-zero coupling to these higher momenta states:

$$|\psi(\tau^+)\rangle = \sum_m \sum_{n=0}^{\infty} e^{-iE_q^{(n)}\tau/\hbar} |\phi_{q+2m\hbar k}\rangle \langle \phi_{q+2m\hbar k} | n, q\rangle \langle n, q | \phi_q\rangle. \quad (4.77)$$

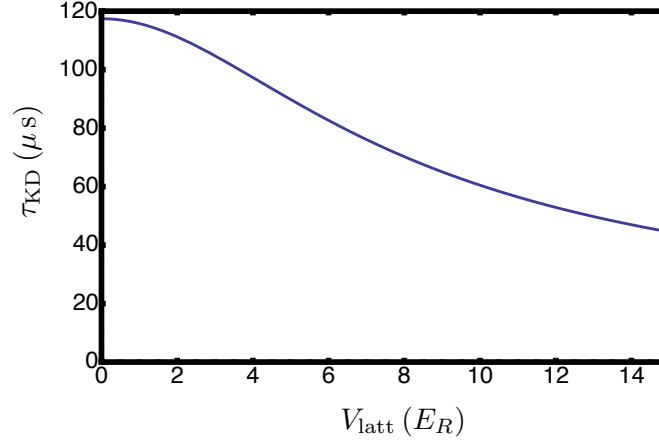


**Figure 4.9: Calculated Kapitza-Dirac diffraction period** Calculation of  $\tau_{\text{KD}}$  from band structure.

We can simplify the interpretation of Equation 5.77 by considering lattice depths below  $10E_R$ . In this limit, we only have significant population of the  $n = 0, 1$  and  $2$  bands. Furthermore, because the BEC plane wave state is even and the  $n = 1$  Bloch state is odd in position,  $|\psi(\tau^+)\rangle$  will only have  $n = 0$  and  $n = 2$  contributions. Therefore, we will have beating between states  $|0, q\rangle$  and  $|2, q\rangle$ , with the period:

$$\tau_{\text{KD}} = \frac{4\pi\hbar}{E_q^{(2)} - E_q^{(0)}}. \quad (4.78)$$

This is Kapitza-Dirac scattering [149]. In Figure 5.8 we plot the fraction of atoms in the  $+2\hbar k$  or  $-2\hbar k$  peaks as a function of the  $\mathbf{y}$  lattice beam pulse (on) time. We then compare the observed diffraction period to the one calculated in Figure 5.9.

#### 4.7.4 Optical lattice heating and switch-off

After alignment of all three lattice beams using the methods described in Section 5.7.2 and Section 5.7.3, atoms are able to be loaded into the optical lattice. In Figure 5.10 we measure the amount heating experienced by atoms loaded into a single optical lattice beam. Doing this for all three beams, we can make sure that the heating rate is negligible compared with the energy and time scales of our system. After optimizing the intensity stabilization servo, we measure a heating rate of roughly  $30 \text{ nK/s}$  at  $50E_R$  in Figure 5.10. This is very close to the heating rate predicted from spontaneous recoil heating:

$$\dot{T}_R \approx \frac{\Gamma_{sc} E_R}{k_B} \approx 20 \text{ nK/s}. \quad (4.79)$$

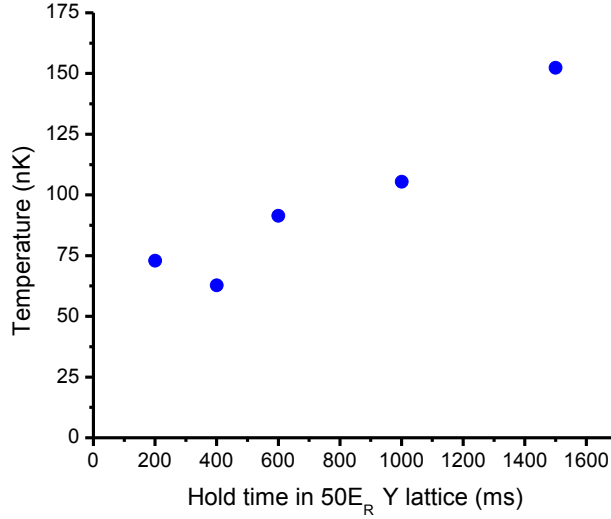


**Figure 4.10: Lattice heating**

Most experiments will involve atoms confined in a potential created by 3 lattice beams at powers of roughly  $10E_R$  for approximately 100 ms. This translates to a temperature increase of 2 or 3 nK during the course of an experiment. This is small compared with a Fermi temperature of order 100 nK.

We also measure the time it takes the optical lattice to switch off. For both shallow ( $< 10E_R$ ) and deep ( $> 500E_R$ ) lattice depths, the lattice may be shut off with a TTL in  $< 100$  ns. It is important for this shut-off time to be as fast as possible for time-of-flight thermometry. Briefly, time-of-flight imaging requires diabatic shut-off. That is, if the fastest time scale in our problem is associated with the lattice oscillation frequency  $\omega_{\text{latt}}$ , then we wish to shut off the laser power from  $P = P_{\text{max}}$  to  $P = 0$  quickly enough that it satisfies the diabaticity criterion:

$$\frac{\dot{\omega}_{\text{latt}}}{\omega_{\text{latt,max}}^2} \gg 1 \rightarrow \frac{d}{dt}(\ln P) \gg 1. \quad (4.80)$$

This criterion is satisfied for all accessible lattice depths (i.e. for  $\omega_{\text{latt,max}}$  up to  $2\pi \times 200$  kHz) in our experiment.

## 4.8 $^{87}\text{Rb}$ SF-MI transition

Because our apparatus is a dual  $^{40}\text{K}$  and  $^{87}\text{Rb}$  system, we may sensitively test the alignment and power regulation of our optical lattice system by attempting to observe the superfluid-Mott insulator (SF-MI) phase transition. The SF-MI transition was first seen in a bosonic cold

atoms system in 2002 by Greiner *et al.* [138]. It has since been observed in systems of different dimensions [150, 151] and geometries [152], as well as being used as medium to store light [153].

The SF-MI transition may be described by the same Hubbard model as described in Equation 5.36, with the changes that  $\hat{b}_i^\dagger$  are bosonic operators that obey the commutation relations  $[\hat{b}_i, \hat{b}_j^\dagger] = \delta_{i,j}$  and we have a single spin state of bosons. The Bose-Hubbard model is then [42]:

$$\hat{H}_{\text{BH}} = -J \sum_{\langle i,j \rangle} \hat{b}_i^\dagger \hat{b}_j + \frac{U}{2} \sum_i \hat{n}_i (\hat{n}_i - 1) + \sum_i \epsilon_i \hat{n}_i. \quad (4.81)$$

When  $J \gg U$ , the states which diagonalize  $\hat{H}_{\text{BH}}$ ,  $|\psi_{J \gg U}\rangle$ , must have the non-zero expectation values  $-\langle J \sum_{\langle i,j \rangle} \hat{b}_i^\dagger \hat{b}_j \rangle$ , and thus  $\langle \hat{b}_j \rangle$  must also be non-zero. States that are Eigenfunctions of the annihilation operator are called coherent states, and can be defined in the basis Fock (number) states  $|n\rangle$ :

$$|\psi_{J \gg U}\rangle \approx |\alpha\rangle \equiv e^{-\frac{|\alpha|^2}{2}} \sum_{n=0}^{\infty} \frac{\alpha^n}{\sqrt{n!}} |n\rangle. \quad (4.82)$$

For a sufficient number of atoms, the expectation value of the annihilation operator is  $\langle \hat{b}_j \rangle = \sqrt{\langle n_j \rangle} e^{i\phi_j}$ , and so the expectation value of  $H_{\text{BH}}$  becomes:

$$\langle H_{\text{BH}} \rangle \approx -\langle J \sum_{\langle i,j \rangle} \hat{b}_i^\dagger \hat{b}_j \rangle = -J \sum_{\langle i,j \rangle} \sqrt{\langle n_j \rangle \langle n_i \rangle} \cos(\phi_j - \phi_i). \quad (4.83)$$

Equation 5.83 expresses that in the limit  $J \gg U$ , the Eigenstates of  $H_{\text{BH}}$  have a definite phase relationship  $(\phi_j - \phi_i)$  between sites  $j$  and  $i$ .

We contrast this to the states which diagonalize  $H_{\text{BH}}$  in the  $J \ll U$  limit, the Fock states:  $|\psi_{J \ll U}\rangle \approx |n\rangle$ . Because Fock states are Eigenstates of the number operator, the  $J \ll U$  Bose-Hubbard model describes a state with a definite number of atoms on each site. Furthermore, we can use the conjugate relationship between number and phase  $[\hat{\phi}, \hat{n}] = i$  to derive an uncertainty relationship:

$$\Delta\phi \Delta n \geq \frac{1}{2}. \quad (4.84)$$

In the experiment,  $\Delta\phi$  is the observable we are able to experimentally access. We adiabatically load atoms into an optical lattice potential of different depths in 200 ms. After a 10 ms hold time, the lattice is instantaneously switched off. After 15 ms of free-fall, the atoms are absorption imaged. Images may be seen in Figure 5.11. The critical ratio of  $J$  to  $U$  in our system is  $(J/U)_C = 0.0341$  [154], corresponding to a critical lattice depth of  $V_{\text{latt},C} \approx 13E_R$ . We can see

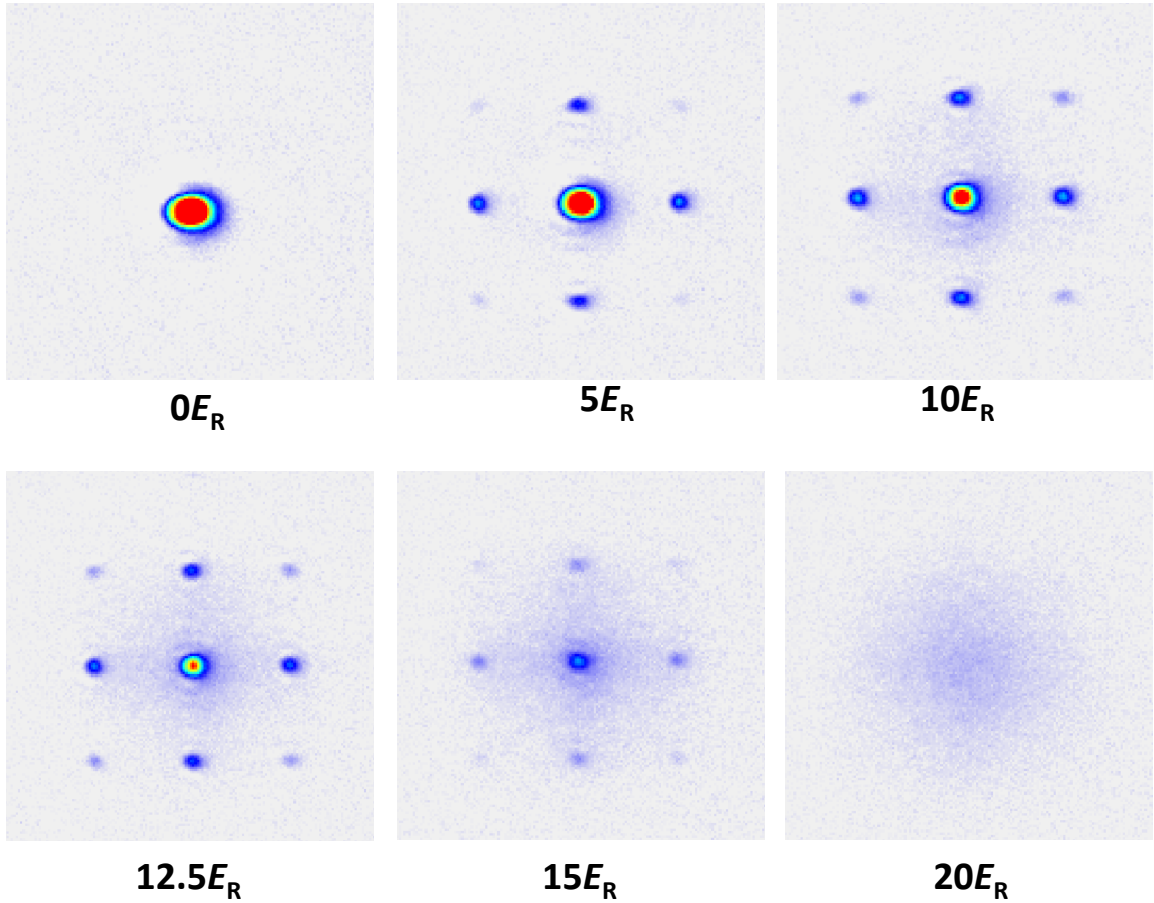


**Figure 4.11: Superfluid-Mott insulator transition** The diffraction pattern after releasing the  $^{87}\text{Rb}$  cloud from a lattice of varying depth. The diffraction peaks are spaced  $\pm 2\hbar k$  from the central peak in momentum. That diffraction peaks exist above the critical depth  $V_{\text{latt,C}} \approx 13E_R$  may be evidence of double occupied sites for which  $J \rightarrow \sqrt{2}J$ .

that for depths less than  $V_{\text{latt,C}}$ , corresponding to  $(J/U) > (J/U)_C$ , we see a diffraction pattern resulting from the interference of coherent states of atoms in the lattice that share a definite phase relationship.

In contrast, when the lattice depth is greater than  $V_{\text{latt,C}}$ , the diffraction visibility disappears. Here, the Eigenstates of the system are Fock states, with definite number at each site but - because of the number-phase uncertainty relation in Equation 5.84 - an indeterminate phase.

We may more quantitatively explain the difference in time-of-flight images between SF and MI phases by considering how a cloud of atoms expand upon release from a one-dimensional lattice potential. After release from position  $x_i$ , the expansion results in a re-scaling of the coordinates:

$$x_i \rightarrow \frac{x_i}{\sqrt{1 + (\omega_i t)^2}} \xrightarrow{\omega_i t \gg 1} \frac{x_i}{\omega_i t} \quad (4.85)$$

We will work in the  $\omega_i t \gg 1$  limit, where the cloud will be assumed to have expanded to be much larger than its original size. Furthermore, if we work in the tight-binding limit where the Wannier functions may be approximated as Gaussians, then we may then write the expanded wave-function as:

$$\psi_i(\mathbf{r}, t) = f(\mathbf{r}, t) e^{im|\mathbf{r}-\mathbf{r}_i|^2/2\hbar t}, \quad (4.86)$$

where  $f(\mathbf{r}, t)$  is the envelope function. Including contributions from each site, the combined wave-function is:

$$\hat{\psi}(\mathbf{r}, t) = \sum_i \psi_i(\mathbf{r}, t) \hat{b}_i, \quad (4.87)$$

and so the density is:

$$\hat{n}(\mathbf{r}, t) = |f(\mathbf{r}, t)|^2 \sum_{\langle i,j \rangle} e^{im(\mathbf{r}-\mathbf{r}_i) \cdot \mathbf{r} / \hbar t} \hat{b}_i^\dagger \hat{b}_j. \quad (4.88)$$

In a time-of-flight image, we measure the average density  $\langle n(\mathbf{r}, t) \rangle$ . This quantity involves the expectation value  $\langle \hat{b}_i \rangle$ , and so for  $\mathbf{r}_i = i\pi/k$ ,  $\langle n(\mathbf{r}, t) \rangle$  in the SF regime is equal to:

$$\langle n(\mathbf{r}, t) \rangle_{\text{SF}} = |f(\mathbf{r}, t)|^2 \sum_{\langle i,j \rangle} e^{2\pi i(i-j)x/l} \sqrt{n_i} \sqrt{n_j} = |f(\mathbf{r}, t)|^2 \frac{\sin^2(\pi N x/l)}{\sin^2(\pi x/l)} \quad (4.89)$$

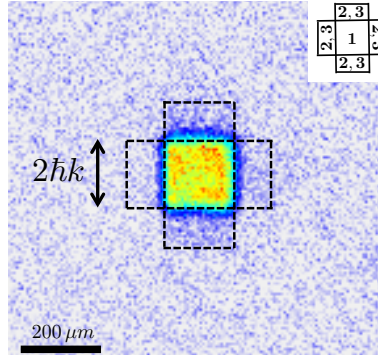


**Figure 4.12:  $^{40}\text{K}$  localization** A band-mapped cloud of  $6 \times 10^4$   $^{40}\text{K}$  atoms after an adiabatic ramp-on and fast ( $200\mu\text{s}$ ) exponential ramp-off of a  $100E_R$  lattice. The mask that is superimposed over the image identifies the first three Brillouin zones for a 2D lattice. The inset figure labels the Brillouin zones and indicates that the second and third Brillouin zones are degenerate in energy.

whereas  $\langle n(\mathbf{r}, t) \rangle$  in the MI regime is equal to:

$$\langle n(\mathbf{r}, t) \rangle_{\text{MI}} = |f(\mathbf{r}, t)|^2 \sum_{\langle i, j \rangle} e^{im(\mathbf{r}-\mathbf{r}_i) \cdot \mathbf{r} / \hbar t} \delta_{i, j} n_i = N |f(\mathbf{r}, t)|^2. \quad (4.90)$$

Here,  $l = 2\hbar kt/m$  and  $N$  is the number of atoms. We see that whereas  $\langle n(\mathbf{r}, t) \rangle_{\text{SF}}$  is sinusoidally modulated,  $\langle n(\mathbf{r}, t) \rangle_{\text{MI}}$  retains only the unmodulated envelope function, in agreement with the images in Figure 5.11.

## 4.9 $^{40}\text{K}$ localization

In contrast to  $^{87}\text{Rb}$  atoms in an optical, Fermi-Dirac statistics prohibits a coherent state of  $^{40}\text{K}$  for low lattice depths. Atoms are still free to tunnel, however, exhibiting “metallic” behaviour analogous to electrons hopping between sites in a crystal. As seen in Figure 5.3, when there are enough atoms (or, equivalently, harmonic confinement) to fill states above the bandwidth energy  $4J$ , atoms populate the localized “edge” states. These edge states not only clamp the average filling per site at 1, but also have identical momentum distributions.

We can see from Figure 5.1 that if we populate only the lowest band of the optical lattice, then atoms will be restricted to *quasi*-momentum between  $-\hbar k$  and  $+\hbar k$ . We may experimentally access the quasi-momentum of our system by quickly ramping down the lattice depth in  $200\mu\text{s}$ , a time that is fast compared with the tunnelling time but slow compared with the energy difference between the ground and first excited band. This quasi-momentum conserving

*band-mapping* process [155] has the effect of reducing the momentum contribution from the lattice, leaving only the quasi momentum  $q$  to be imaged after time of flight. That is, the position of an atom with quasi momentum  $q$  after time-of-flight time  $t$  is  $x = qt/m$ . Figure 5.12 shows an image of a band-mapped cloud of  $^{40}\text{K}$ . Notice that the cloud retains the symmetry of the lattice potential.

Band-mapping is unable to distinguish between localized band insulating states and localized edge states due to the similarity in quasi momentum distributions. A single-site measurement would be able to discriminate between the two states, however. In the following chapter, we outline our approach to realizing a local probe measurement of  $^{40}\text{K}$  in an optical lattice.

## Chapter 5

# New tools for single-site imaging

We have described in previous chapters the apparatus responsible for cooling a cloud of  $^{40}\text{K}$  and  $^{87}\text{Rb}$  to quantum degeneracy, and then controlling its behaviour in an optical lattice. This work is preparatory, however, to our goal of imaging quantum states with resolution on the scale of the inter-particle, or lattice, spacing. In this chapter, we describe the tools and techniques developed in order to achieve this goal.

Atoms have been imaged with single site resolution before. In 2007, Nelson *et al.* fluorescence imaged  $^{133}\text{Cs}$  atoms that had been loaded into a 3D optical lattice with  $4.9\ \mu\text{m}$  site spacing [21].  $^{133}\text{Cs}$  atoms have also been absorption imaged *in situ* in a 2D 532 nm-spaced optical lattice [20]. In two separate observations, the site occupation of  $^{87}\text{Rb}$  atoms in a single plane of a 640 nm [9] and 532 nm [10] 3D optical lattice were determined by capturing the scattered fluorescence from atoms as they were being sub-Doppler cooled. In a novel experiment,  $^{87}\text{Rb}$  atoms loaded into a 1D 600 nm-spaced optical lattice were individually ionized by a narrowly-focused electron beam and detected [156]. The only single-site imaging to date of a Fermi gas has been the absorption imaging of  $^6\text{Li}$  atoms trapped in a 4x4-site 2D optical lattice with a minimum site-spacing of  $1.2\ \mu\text{m}$  [157].

It is possible to determine the number occupation of a lattice site even when the diffraction limited resolution is larger than the site spacing [158, 159]. The site occupation of  $^{133}\text{Cs}$  atoms loaded into a 433 nm 1D optical lattice was measured using an imaging system with a diffraction limited resolution of  $1.79\ \mu\text{m}$ , over four times that of the lattice spacing [158]. The problem of imaging atoms was reduced to one of parameter estimation when prior information about the discrete positioning of atoms was used alongside a thorough characterization of the point spread function (PSF). Prior information about the lattice structure has also been used to determine the 3D distribution of atomic nano particles with atomic resolution by combining information from two orthogonal scanning transmission electron microscopy images [159].

The Rayleigh criterion for resolving point source emitters is a more stringent imaging measure, though a useful heuristic. It states that two point sources may be resolved if the position of one source sits at the minimum of the Airy function of the other [160]. The minimum Rayleigh resolvable distance for point sources emitting light with wavelength  $\lambda$  is  $0.61\lambda/\text{NA}$ , where NA is the numerical aperture of the imaging system. It is evident that the resolution is minimized when  $\lambda$  is small and NA is large. Because the critical temperatures for phase transitions in a lattice scale as the square of the lattice period, we would like to be able to image distances that are as small as possible.

The vacuum and magnetic transport systems have been designed in order to allow for the integration of a high NA imaging system. We describe the imaging system in detail in Section 6.1. The choice of  $\lambda$  is constrained by the available optical transitions in  $^{40}\text{K}$ . We showed in Chapter 4 the ability to control atoms with light near-detuned from the 405 nm  $4S_{1/2} \rightarrow 5P_{3/2}$  transition. Due to shot noise, the ability to identify the occupation of a lattice site depends on the detected photon number: if the pixels on a camera capture an average of  $N_\gamma$  photons, there will be a  $\sqrt{N_\gamma}$  variation in the number of detected photons on each individual pixel. In order to increase the signal-to-noise of the imaging system, we would like to collect many hundreds of photons per atom. This means scattering many times more, due to the finite collection, transmission, and detection efficiencies of the system. Each time that an atom scatters a photon it picks up  $2E_R = \hbar^2 k^2/m$  in energy. This means that an atom that scatters just a few hundred photons would have enough energy to escape from the optical lattice. It is therefore necessary to cool atoms to a temperature much less than the lattice depth, while simultaneously collecting fluorescence from them. In Section 6.2, we demonstrate a sub-Doppler cooling technique that uses the 770 nm  $4S_{1/2} \rightarrow 4P_{1/2}$  transition to cool atoms to  $10 \mu\text{K}$ , a temperature much less than the  $200 \mu\text{K}$  lattice depth. We describe the properties of this transition and show evidence that D1 sub-Doppler cooling plus 405 nm fluorescence is a promising approach towards single-site imaging of  $^{40}\text{K}$  in an optical lattice.

## 5.1 Imaging hardware

### 5.1.1 Imaging requirements

We consider here the numerical aperture, photon wavelength, and detected photon number necessary for measuring the number occupancy of individual lattice sites with high fidelity.

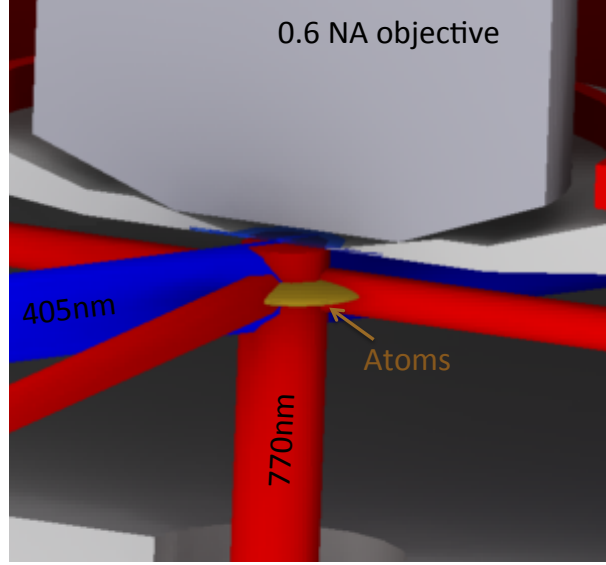


**Figure 5.1: Single-site imaging approach:** A 2D plane of atoms (yellow disk) are trapped  $800\ \mu\text{m}$  below a  $200\ \mu\text{m}$  thick sapphire imaging window. On the air side of this window is an  $\text{NA}=0.6$  imaging objective with a working distance of  $2\ \text{mm}$ . Atoms are simultaneously cooled using light tuned near the  $770\ \text{nm}$  D1 transition and excited with a  $405\ \text{nm}$  beam.

### Single-plane imaging

The Debye integral for the 3D electric field near the focus of an imaging lens is given by [160]:

$$\mathbf{E}(x, y, z) = -i\mathbf{A} \frac{2\pi}{\lambda} \left(\frac{a}{f}\right)^2 e^{i\left(\frac{f}{a}\right)^2 u} \int_0^1 J_0(v\rho) e^{-iu\rho^2} \rho d\rho \quad (5.1)$$

where  $u$  and  $v$  are the scaled axial and radial coordinates, respectively:

$$u = \frac{2\pi}{\lambda} \left(\frac{a}{f}\right)^2 z, \quad v = \frac{2\pi}{\lambda} \left(\frac{a}{f}\right) \sqrt{x^2 + r^2}. \quad (5.2)$$

Here,  $f$  is the effective focal length,  $a$  is the radius of the aperture,  $\lambda$  is the wavelength of the light being collected,  $\mathbf{A}$  is the amplitude of the electric field,  $J_0(x)$  is the zeroth order Bessel function, and  $\rho$  is the scaled aperture coordinate that we integrate over. The Debye integral Equation 6.1 is valid over all space when  $f \rightarrow \infty$ , and becomes approximate in the parameter  $a/f$  otherwise. The intensity is:

$$I(x, y, z) = \frac{c\epsilon_0}{2} |\mathbf{E}(x, y, z)|^2 \quad (5.3)$$

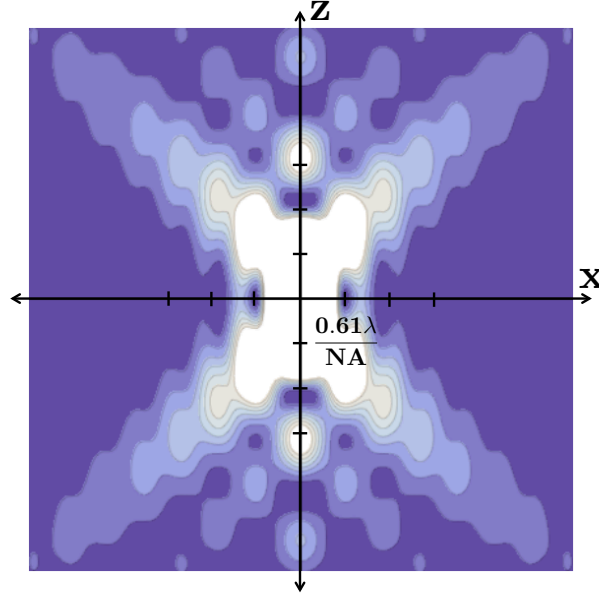


**Figure 5.2: 3D Intensity distribution from a point source:** The intensity distribution of light focused to the  $z = 0$  plane by an imaging system with aperture radius  $a$  and effective focal length  $f$ .

We can make Equation 6.3 an explicit function of the numerical aperture by making the substitution:

$$\frac{a}{f} = \frac{1}{\sqrt{(n/\text{NA})^2 - 1}} \quad (5.4)$$

Figure 6.2 shows a projection of the intensity onto the  $xz$  plane.

We see from Figure 6.2 that the first intensity minima - the distance which defines the resolution - is farther away in the axial direction ( $2\lambda/\text{NA}^2$ ) versus the transverse direction ( $0.61\lambda/\text{NA}$ ). The intensity in the axial direction also propagates well beyond the first minima before decaying, in contrast to the transverse direction. For these reasons, it is necessary to isolate a single plane of atoms to image.

The transverse PSF of an imaging system is the 2D intensity distribution in the focal plane:

$$\text{PSF}(x, y) = I(x, y, 0). \quad (5.5)$$

### A criteria for choosing the imaging NA

One measure that we can use to determine the NA and  $N_\gamma$  required in order to measure occupation of a lattice site is to imagine whether it is possible to distinguish between the two scenarios depicted in Figure 6.3. In these scenarios, our problem is to correctly identify whether

there is an atom at the site of interest, or not, when there are zero or one atoms randomly distributed in neighbouring sites. We are helped by the fact that we have prior knowledge of our system. We know, for instance, that all  $^{40}\text{K}$  atoms are identical and will scatter, on average, the same number of photons. We also know that the atoms will sit at discrete points of the optical lattice. Finally, because of high probability that two atoms sitting in the same lattice site will undergo light-assisted collisions when illuminated by the cooling and fluorescing light, each site will have either zero or one atom.

The number of photons collected on pixel  $i, j$  on a focused camera ( $\mathbf{z} = 0$ ) with pixel size  $d_p$  in time  $\Delta t$  is:

$$N_{ij} = I(i d_p, j d_p, 0) d_p^2 \Delta t / \hbar \omega \quad (5.6)$$

Let's call  $N_0$  the average number of photons scattered into the pixels circumscribed by the box in Figure 6.3a with zero atoms, and  $N_1$  the average number of photons scattered for the one atom scenario depicted in Figure 6.3b:

$$N_{0(1)} = \sum_{i,j}^{\text{box } 0(1)} N_{i,j} \quad (5.7)$$

Photon shot noise will add uncertainty to the number of photons collected at each pixel  $d_{i,j}$ . If the most likely scattered photon number is  $\langle N \rangle$ , the probability of capturing  $k$  photons is given by the Poissonian distribution:

$$P_{i,j}(\langle N_{i,j} \rangle; k) = \frac{\langle N_{i,j} \rangle^k e^{-\langle N_{i,j} \rangle}}{k!} \quad (5.8)$$

The total probability distribution from the collection of pixels within the measurement area  $a_{\text{box}}$  is:

$$P = \frac{d_p^2}{a_{\text{box}}} \sum_{i,j}^{\text{box}} P_{i,j}(\langle N_{i,j} \rangle; k) \quad (5.9)$$

The fidelity with which we are able to correctly identify the presence, or not, of an atom decreases the more two probability distributions overlap:

$$F = 1 - \frac{\sum_{N_\gamma=0}^{\infty} P(N_0; N_\gamma) P(N_1; N_\gamma)}{\sum_{N_\gamma=0}^{\infty} (P(N_0; N_\gamma) + P(N_1; N_\gamma))} \quad (5.10)$$

The ratio of photons collected to photons scattered depends on the solid angle subtended

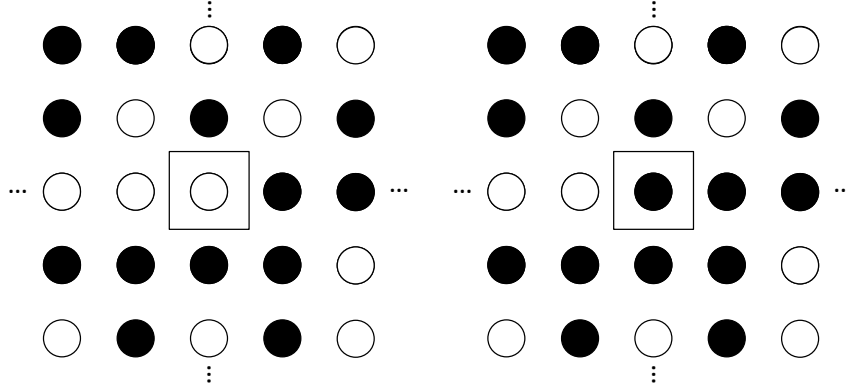


**Figure 5.3: Discerning the presence (or not) of an atom** A scenario imagined to estimate the numerical aperture and detected photon number necessary to correctly identify the presence, or not, of an atom. We assume that the only information available is the number of photons collected on each pixel within the measurement area circumscribed by the box.

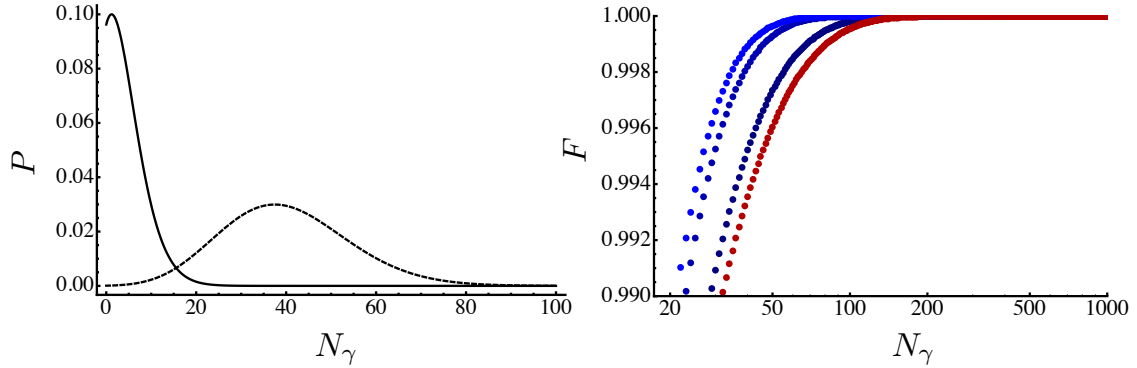


**Figure 5.4: Fidelity: Left**), the probability distributions for  $N_0$  (solid line) and  $N_1$  (dashed line) for atoms that each scatter an average of 40 photons. If we detect a photon number that lies in the overlap region of the two probability distributions, we are unable to distinguish between there being an atom at the site of interest or not. **Right**), the fidelity versus detected photon number of correctly identifying the presence of an atom on site when capturing 405 nm photons through a NA=0.4 (dark blue), NA=0.5 (blue), and NA=0.6 (light blue) objectives. The fidelity when capturing 767 nm photons through a NA=0.6 (red) objective is also shown.

by the imaging system. For small numerical apertures, the collected photon fraction can be estimated to be  $1/4((n/\text{NA})^2 - 1)$ . Accounting for transmission and camera efficiencies (which we conservatively estimate to be 25% total) we conservatively estimate that it is necessary for an atom to scatter 100 photons for every one photon that we detect. If we are using an  $\text{NA}=0.6$  objective at 405 nm then we need to scatter at least a few thousand photons per atom.

Throughout, we have made the approximation that atoms are stationary in lattice sites and not jiggling about with some thermal uncertainty. This approximation is valid since  $\sqrt{k_B T/m\omega^2} \ll \lambda/2\text{NA}$  at  $10\ \mu\text{K}$ .

Note that image reconstruction techniques can make use of additional bits of information, such as the shape of the intensity distribution, in order to more accurately determine lattice occupation. In fact, with enough signal to noise, an image may be reconstructed with any resolution imaging system [161].

### 5.1.2 405 nm objective and sapphire imaging window

Our objective is custom made from Special Optics. It has an  $\text{NA}=0.6$  at 405 nm and an  $\text{NA}=0.45$  at 767 nm. We do not have single-site imaging capability at 767 nm but the resolution is sufficient to aid in coarse alignment and focusing. The effective focal length of the objective is 3.3 mm and the working distance is 2.43 mm. The objective is paired with a 170 mm focal length tube lens for a  $51\times$  magnification.

The objective sits on the atmosphere side of the experiment, separated from the atoms in vacuum by a  $200\ \mu\text{m}$  thick Sapphire window. The feasibility of using a thin Sapphire window to image through was first investigated by Amir Mazouchi [162]. The window is 12 mm in diameter and was brazed to a Titanium sub-flange by the UK Atomic Energy Authority. The window is chosen to be thin in order to accommodate conventional commercial microscopy designs that correct for  $200\ \mu\text{m}$  thick cover-slips. The attachment method constrains the choice of window material. Brazing is a high-temperature process, and sapphire and Titanium have similar coefficients of thermal expansion ( $6 \times 10^{-6} K^{-1}$  and  $8.6 \times 10^{-6} K^{-1}$ , respectively), compared with  $0.6 \times 10^{-6} K^{-1}$  for fused quartz. Sapphire is also more tolerant of mechanical stress than quartz, with a modulus of rupture that is  $10\times$  as large, and a Young's modulus that is  $5\times$  as large. Sapphire is slightly birefringent. This effect is reduced by cutting the window along its  $c$ -axis.

### Objective characterization

We have attempted to characterize our imaging system *ex situ* in three different ways: imaging a nano hole array [163], imaging a 500 nm pinhole [163], and imaging an MRS-5 target [164].

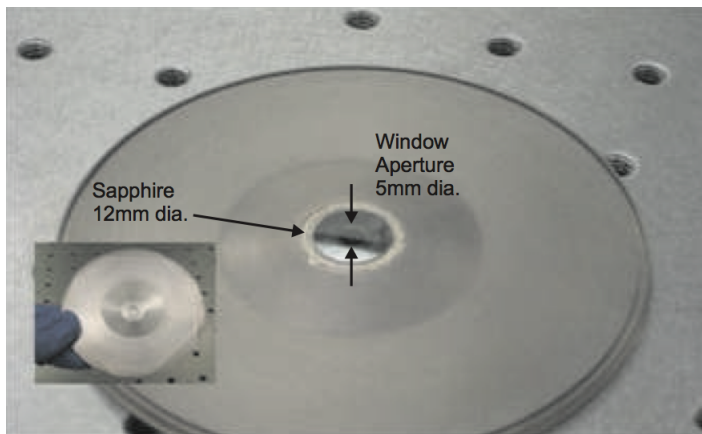


**Figure 5.5: Sapphire window brazed to Ti sub-flange.** Image courtesy of Dave McKay [1].

Imaging through the sapphire window makes a negligible difference to imaging quality.

The nano hole array consists of 200 nm diameter holes, etched in Ag, spaced 500 nm apart. The 100 nm thick Ag layer sits on top of a glass substrate. The sample was provided by the group of Sang-Hyun Oh at the University of Minnesota [165]. Figure 6.6 shows the optical image of this object. The objective collects the light transmitted through the sample. The narrow-band light has a wavelength of 405 nm and is made temporally incoherent by including a rotating diffuse material in its path before Köhler illuminating the sample [166]. Inspecting Figure 6.6, we can clearly distinguish light emanating from different holes in the array. This method provides qualitative confidence that the objective is able to resolve atomic point sources in a 523 nm spaced lattice. See Carolyn Kieran’s report [163] for a quantitative study. We have also imaged diffuse light through a 500 nm pinhole (National Aperture) in an attempt to extract the PSF of our imaging system. The convolution of the PSF with the pinhole window function ( $w(r < d) = 1, w(r > d) = 0$ ) gives the observed intensity distribution:

$$I_{\text{pinhole}}(x, y) = \int_{-\infty}^{\infty} \text{PSF}(x_0, y_0) w(x - x_0, y - y_0) dx_0 dy_0. \quad (5.11)$$

An MRS-5 reflective target (Geller Microanalytical Laboratory) has also been imaged. The MRS-5 target is made from tungsten on an  $\text{SiO}_2$  layer. The sample was reflectively Köhler illuminated during tests. In Figure 6.6, it is clear that features down to 600 nm are resolvable. The PSF may be inferred from the Fourier transform of the pitch contrast. Similarly to the nano hole method, it is encouraging that features comparable in size to the lattice spacing may be resolved. However, due to the ambiguous effect of the reflective illumination of the MRS-5 target, we hazard to draw quantitative conclusions about our imaging system from this method.

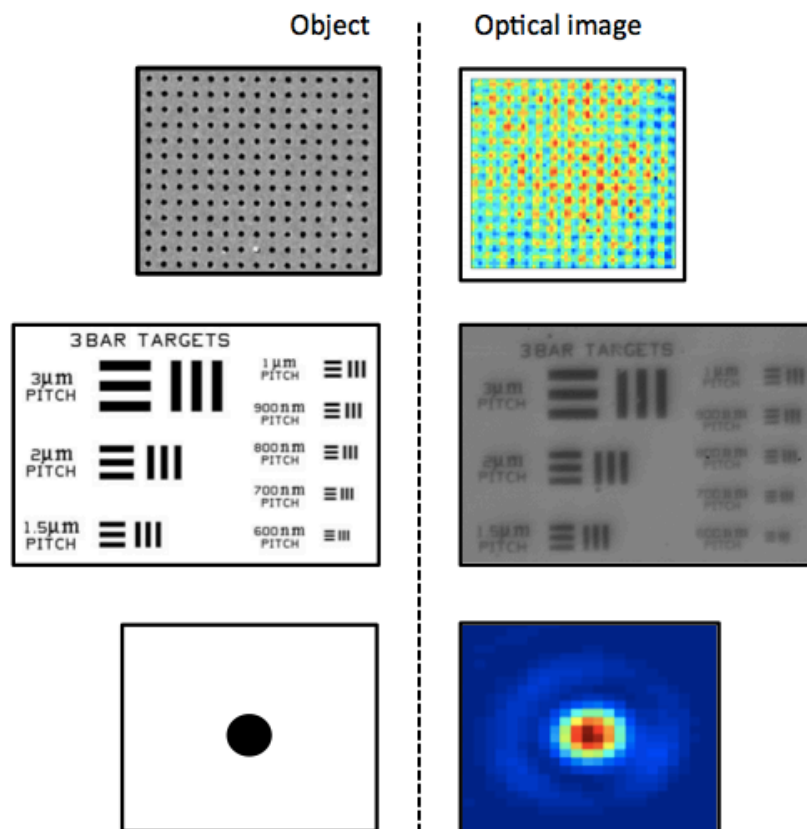


**Figure 5.6: Methods for objective characterization** Nano-hole array with 200 nm diameter holes spaced 500 nm apart (top), MRS-5 target (middle), 500 nm pinhole (bottom).

### 5.1.3 Objective mounting and alignment

The objective is attached to the science chamber using aluminum mounts that support a three-axis manual translation stage (Newport M406), a two-axis tilt stage (Newport TTN80), and a focusing piezo stage (PI P-733.Z). The aluminum mounts were designed by Carolyn Kierans [163] and the microscope stack was stability tested by Thomas Maier [167].

The objective is transversely aligned by imaging the small amounts of vertical lattice beam transmitted through the AR coated imaging window. The alignment is fine-tuned by absorption imaging progressively colder (i.e. smaller) clouds of atoms.

The objective is aligned in the focal direction in two steps. First, the focal position of the objective is chosen to minimize the absorption-imaged cloud size of a small BEC. Then, the objective is positioned to maximize the fluorescence signal of a small resonant beam through a thermal cloud of atoms. We image the wavelength tuneable  $35\mu\text{m}$  plug beam which is well-aligned to the quadrupole trap centre. This final alignment step positions the objective focus to within the plug beam width of the atom's position.

### 5.1.4 Prospects for imaging

We have commissioned and characterized a high resolution objective for imaging 405 nm fluorescence from atoms trapped in a 527 nm-period optical lattice through a  $200\mu\text{m}$ -thick sapphire window. The objective has been characterized *ex situ* by imaging a reflectively illuminated pitch target, and the transmitted light through a nano hole array and a  $500\mu\text{m}$  diameter pinhole. We have been able to qualitatively resolve transmitted light through the nano hole array, giving us confidence in our ability to resolve similarly spaced atomic point sources in an optical lattice.

## 5.2 Sub-Doppler cooling

As discussed in Section 2.1 and Chapter 4, Doppler cooling can cool atoms to a temperature  $T_D$  set by the transition linewidth  $\Gamma$ :

$$k_B T_D = \frac{\hbar\Gamma}{2}. \quad (5.12)$$

For alkali atoms such as  $^{40}\text{K}$  and  $^{87}\text{Rb}$  with  $\Gamma \approx 2\pi \times 6\text{ MHz}$  this translates into  $T_D \approx 150\mu\text{K}$ , or for narrower line excited state transitions as discussed in Chapter 4 and [168], a Doppler temperature  $T_D \approx 70\mu\text{K}$ . These temperatures are not small compared to our available lattice depth of  $200\mu\text{K}$ . Using the Arrhenius model for thermal hopping defined in Equation 1.3 with  $\Gamma_a$  an average of the two previously measured attempt rates for neutral atoms in an optical

lattice [21, 22], we can estimate a hopping rate of  $\sim 1$  Hz for atoms at  $70 \mu\text{K}$  in a  $200 \mu\text{K}$ -deep lattice. We argued in Section 1.1 that a  $10$  mHz hopping rate was necessary for high fidelity imaging and that achieving this requires cooling the atoms to  $30 \mu\text{K}$  in a  $200 \mu\text{K}$ -deep lattice. This temperature is below any observed Doppler temperature in  $^{40}\text{K}$ .

Fortunately, we can cool below the Doppler limit when coherent effects between the cooling beams and atoms with a multiplicity of ground states are included. This new limit is set by the AC Stark shift of the ground state,  $\hbar\Delta'$ , which can be an order of magnitude less than  $\hbar\Gamma$ . These *sub-Doppler* cooling mechanisms can achieve temperatures of order the recoil temperature  $k_B T_R = \hbar^2 k^2 / 2m$  and lower. For  $^{40}\text{K}$  atoms that scatter  $767$  nm photons,  $T_R = 414$  nK.

Sub-Doppler cooling, first observed in 1988 [169], is a common technique in laser cooling and cold atom experiments. A sub-Doppler cooling mechanism can be achieved by creating a polarization gradient in the light field. Polarization gradient cooling on the D2 transition has been widely demonstrated in  $^{87}\text{Rb}$  and other bosonic alkalis, including as a way to cool and image atoms trapped in an optical lattice [21, 9, 10].

However, D2 polarization gradient cooling of  $^{40}\text{K}$  is either weak [97, 98] or difficult to observe [99], likely due to the unresolved and inverted excited hyperfine state structure. Recently it was shown that with a precise tuning of the D2 wavelength within the similarly unresolved excited state structures of  $^{39}\text{K}$  and  $^{41}\text{K}$  it was possible to cool these isotopes to  $25 \mu\text{K}$  and  $47 \mu\text{K}$ , respectively [170].

In 1996, a new type of polarization gradient cooling was demonstrated in  $^{133}\text{Cs}$  [171]. This cooling mechanism makes use of internal states on the  $F \rightarrow F - 1$  transition that are uncoupled from the light field. As an atomic sample cools, atoms spend more time in these dark states, with a corresponding reduction in the density-limiting radiation pressure from re-scattered photons. Recently, it was shown that this “gray” cooling mechanism was also present in  $^{40}\text{K}$  on the D1  $4S_{1/2} \rightarrow 4P_{1/2}$  transition: Fernandes *et al.* were able to cool a cloud of  $^{40}\text{K}$  initially at  $4$  mK to  $20 \mu\text{K}$  [172].

The idea of velocity trapping atoms in a dark state was first demonstrated in  $^4\text{He}$  [173]. In this velocity selective coherent population trapping (VSCPT) technique, atoms near zero velocity were coherently trapped in a dark superposition of Zeeman ground states, allowing for cooling below the recoil limit. Sub-recoil cooling can also be achieved by making use of the Raman coherence between different hyperfine ground states [174]. Because the Raman transition linewidth can be extremely narrow, so too can the velocity class of atoms addressed by the two-photon cooling process.

Recent work with  $^6\text{Li}$  [175] and  $^{39}\text{K}$  [176, 177] has shown that it is possible to combine gray D1 cooling with an additional polarization gradient cooling mechanism resulting from a

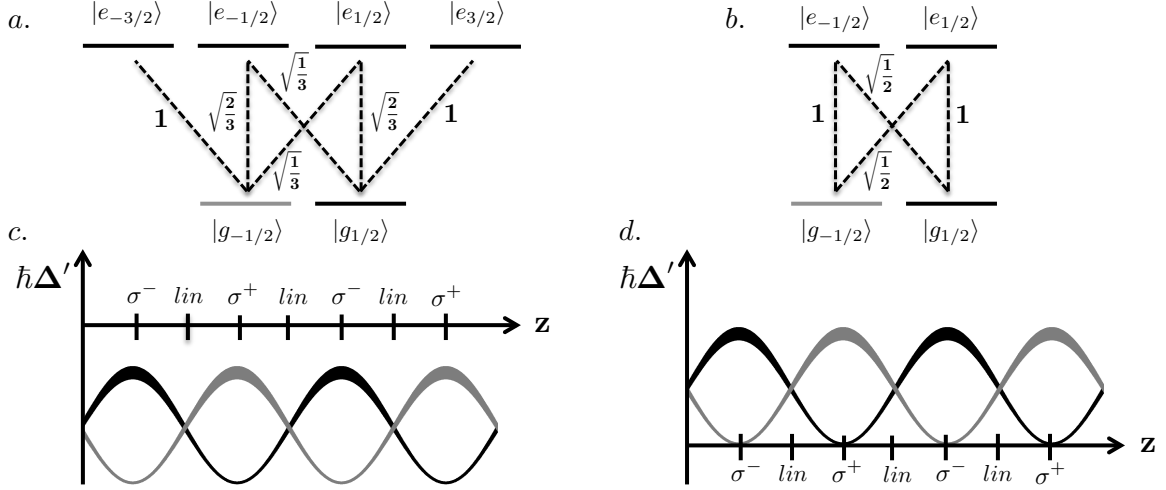


**Figure 5.7: Toy atom level diagram (a)**  $F = 1/2 \rightarrow F' = 3/2$  level scheme with associated Clebsch-Gordan coefficients. **(b)**  $F = 1/2 \rightarrow F' = 1/2$  level scheme with associated Clebsch-Gordan coefficients. **(c)** Light shift of the  $F = 1/2 \rightarrow F' = 3/2$  ground states in a red-detuned  $lin \perp lin$  polarization lattice. **(d)** Light shift of the  $F = 1/2 \rightarrow F' = 1/2$  ground states in a blue-detuned  $lin \perp lin$  polarization lattice.

two-photon Raman cooling process. In this section, we report on the combined D1 + Raman cooling of  $^{40}\text{K}$  to  $16 \mu\text{K}$  in free space.

In addition, we investigate the laser cooling of  $^{40}\text{K}$  atoms that have been loaded into the lowest band of an optical lattice. In previous work,  $^{133}\text{Cs}$  atoms trapped in a 2D  $29 \mu\text{m}$ -period optical lattice were cooled with a gray molasses to  $2 \mu\text{K}$  and  $n \approx 10^{19} \text{m}^{-3}$  [178]. We observe cooling to  $12 \mu\text{K}$  in a  $250 \mu\text{K}$ -deep 3D  $527 \text{nm}$ -period optical lattice, to our knowledge the lowest laser-cooled temperature of  $^{40}\text{K}$  yet reported. We also explore whether  $^{40}\text{K}$  atoms in an optical lattice may be laser cooled while being simultaneously excited on the  $405 \text{nm } 4S_{1/2} \rightarrow 5P_{3/2}$  transition.

### 5.2.1 The Sisyphus cooling mechanism

Sisyphus cooling is a sub-Doppler cooling technique where the polarization gradient is created from the interference of  $lin \perp lin$ -polarized counter propagating beam pairs in one dimension, or with  $\sigma^+ - \sigma^-$  polarized beam pairs in all three dimension. The common feature among all Sisyphus cooling realizations is that optical pumping is most likely to occur at the top of a light-shift potential rather than at the bottom. In the following, we illustrate this effect using model  $F = 1/2 \rightarrow F' = 3/2$  and  $F = 1/2 \rightarrow F' = 1/2$  transitions that contain the ingredients required to understand and compare the Sisyphus mechanism on the  $5S_{1/2} - 5P_{3/2}$  D2 transition in  $^{87}\text{Rb}$  and the  $4S_{1/2} - 4P_{1/2}$  D1 transition in  $^{40}\text{K}$ , respectively.

Figure 6.7a shows the atomic levels for the  $F = 1/2$  ground and the  $F' = 3/2$  excited state. The atom sits in a 1D polarization lattice formed from the interference of counter-propagating beams with crossed linear polarizations, i.e. the  $lin \perp lin$  configuration. The resulting polarization lattice is shown on the horizontal axes of Figure 6.7c. and d. The state dependent light shift potential is:

$$\hbar\Delta' \approx \frac{\hbar}{4\delta} \sum_{q;i,j} \Omega_q^2 |c_{ij}|^2 \quad (5.13)$$

where  $q$  is the polarization that connects states  $i$  and  $j$ ,  $c_{ij}$  is the Clebsch-Gordan coefficient, and  $\Omega_q$  is the Rabi rate for light with polarization  $q$ . If the detuning is chosen to be negative  $\delta < 0$ , as is required for Doppler cooling, it becomes evident that  $|g'_{1/2}\rangle$  is shifted to its lowest energy in the  $\sigma^+$  region of the polarization lattice, and shifted the least in the  $\sigma^-$  region. In contrast,  $|g'_{-1/2}\rangle$  is shifted to its lowest energy in the  $\sigma^-$  region of the polarization lattice, and the shifted least amount in the  $\sigma^+$  region.

The optical pumping rates are also position dependant: an atom in  $|g'_{1/2}\rangle$  is most likely to be pumped into  $|g'_{-1/2}\rangle$  when at the  $\sigma^-$  point of the polarization lattice - i.e. at the top of the light-induced potential. This is indicated in figure 6.7 as a broadening of the energy shift. Similarly, an atom in  $|g'_{-1/2}\rangle$  is most likely to be pumped into  $|g'_{1/2}\rangle$  when at the  $\sigma^+$  point of the polarization lattice, also at the top of its light shift. This broadening can be understood as an admixture of the excited state with the ground state:

$$|g'\rangle \approx |g\rangle - i\Omega/\delta|e\rangle. \quad (5.14)$$

We can infer an optical pumping rate proportional to the probability that an atom is in the excited state, which in the large detuning limit is:

$$\Gamma' \approx \Gamma \left| \frac{\Omega}{\delta} \right|^2. \quad (5.15)$$

Every time that an atom is pumped from  $|g'_{\pm 1/2}\rangle$  to  $|g'_{\mp 1/2}\rangle$ , it coherently absorbs a  $\sigma^\mp$  photon and emits a  $\sigma^\pm$  photon, losing  $\hbar|\Delta'_{1/2} - \Delta'_{-1/2}| \sim \hbar\Delta'$  in energy. Because this process happens every optical pumping time  $1/\Gamma'$ , we can define a cooling rate:

$$\left( \frac{dE}{dt} \right)_{\text{cool}} = \hbar\Delta'\Gamma'. \quad (5.16)$$

Note that this cooling mechanism would turn into a heating mechanism if the red-detuning became blue. In this case, the light shift would take on the opposite sign at the same points in

the polarization lattice - with hills in the potential becoming valleys, and vice versa - yet with the optical pumping's position dependence remaining unaffected. An atom would instead *gain* an additional  $\hbar\Delta'$  worth of energy every optical pumping time.

However, for the case of a  $F = 1/2 \rightarrow F' = 1/2$  atom as illustrated in Figure 6.7b, a *Sisyphus mechanism only exists for blue-detuned light*. This is because certain transitions are “dark” to the incident light. For example, an atom in  $|g'_{1/2}\rangle$  sitting at the  $\sigma^+$  point in the polarization lattice will not experience a light shift because all Clebsch-Gordan coefficients for this polarization are zero. But, as can be seen in Figure 6.7d, optical pumping from  $|g'_{\pm 1/2}\rangle$  to  $|g'_{\mp 1/2}\rangle$  will still happen most frequently at the  $\sigma^\mp$  points in the polarization lattice, that is, at the top of the light-induced potentials. In this case, red-detuning  $\delta$  would lead to heating, in contrast with the  $F = 1/2 \rightarrow F' = 3/2$  case.

There are a few key points to consider when choosing parameters for a Sisyphus cooling stage:

- **Capture velocity:** Similar to Doppler cooling where the capture velocity is determined by the line width of the transition  $\Gamma$ , sub-Doppler cooling captures atoms travelling with velocities determined by the optical pumping rate  $\Gamma'$ :

$$kv_c \approx \Gamma' \approx \Gamma \left| \frac{\Omega'}{\delta} \right|^2. \quad (5.17)$$

This suggests that in order to capture as many atoms as possible it is best to use high powers and small detunings.

- **Equilibrium temperature:** The Sisyphus cooling mechanism works only as long as an atom is able to climb high enough on the light shift potential to be optically pumped into a lower energy state. This argument sets the minimum temperature at a fraction of the light shift  $\hbar\Delta'$ , and indeed a semi-classical calculation [179] estimates the equilibrium temperature to be:

$$k_B T_S = \frac{\hbar\Delta'}{8} = \frac{\hbar\Omega^2}{32|\delta|} \quad (5.18)$$

This would encourage low powers and large detunings, contrary to what one would like maximize for capture velocity. A common technique, then, is to have high powers during the initial stage of the Sisyphus molasses in order to capture as many atoms as possible, then lower the power in order to achieve low temperatures.

- **Sisyphus cooling v.s. Doppler heating in a blue detuned molasses:** In the  $F = 1/2 \rightarrow F' = 1/2$  blue-detuned molasses scheme, a natural question to ask is how

the cooling from the Sisyphus mechanism compares with the heating from the Doppler mechanism. In the low-temperature limit, when  $kv \ll \Gamma'$ , we saw that the Sisyphus frictional force, and thus the cooling rate, was a factor  $\Delta'/\Gamma' = \delta/4\Gamma$  as strong as that of Doppler cooling. This means that blue-detuned Sisyphus schemes must work at detunings  $\delta$  greater than the natural line width  $\Gamma$  in order to overcome the Doppler heating mechanism.

### 5.2.2 The $^{40}\text{K}$ D1 Sisyphus mechanism

In real alkali atoms, the level structure is more complicated than the simple transitions considered in the previous section. A complication arises when there are  $F \rightarrow F' + 1$  and  $F \rightarrow F'$  or  $F \rightarrow F' - 1$  transitions close to each other in energy. In this case, the Sisyphus cooling from one transition may have to compete with the Sisyphus heating from another. This is evidently the case on the D2 transition in  $^{40}\text{K}$ : if we red-detune from the bright  $F = 9/11 \rightarrow F' = 11/2$  transition, we are also red-detuned from the dark  $F \rightarrow F$  and  $F \rightarrow F - 1$  transitions, only a few line widths away. This fact may explain why sub-Doppler cooling is known to work best for atoms with a resolved and non-inverted excited state hyperfine structure such as  $^{87}\text{Rb}$  and  $^{133}\text{Cs}$ .

There exists a Sisyphus cooling mechanism on the 770 nm  $4S_{1/2} - 4P_{1/2}$  D1 transition shown in Figure 6.8. This is a  $F = 9/2 \rightarrow F' = 7/2$  transition and so it has two dark states. Notably, there are only two excited states in this hyperfine manifold, well-separated in energy and both providing a Sisyphus cooling mechanism to blue-detuned incident light. Figure 6.8 shows the eigenvalues of this transition in the presence of a  $lin \perp lin$  cooling  $F = 9/2 \rightarrow F' = 7/2$  and repumping  $F = 7/2 \rightarrow F' = 7/2$  light. From the broadening of the levels in Figure 6.8 it is evident that atoms are most likely to be optically pumped when at the top of the light shift potential. This then realizes the Sisyphus condition.

Inspecting Figure 6.8, we see that there are dark eigenstates that are unshifted by the light at every point in space. This would seem to be a bad thing - if atoms were pumped to these dark states, they would be lost to the cooling process. However, these states are not completely dark. There are two mechanisms which bring atoms back into bright states: motional coupling and off-resonant coupling. Motional coupling describes the process whereby an atom in a dark state that is moving through the polarization lattice hops into a bright state. The motional coupling rate increases with velocity [180], and has been estimated to be equal to  $\Gamma_m = kv$  [172]. Because this process is most likely to occur at the valley points of the light-shift potential, when the two levels are closest, this process does not heat. Off-resonant coupling transfers atoms from

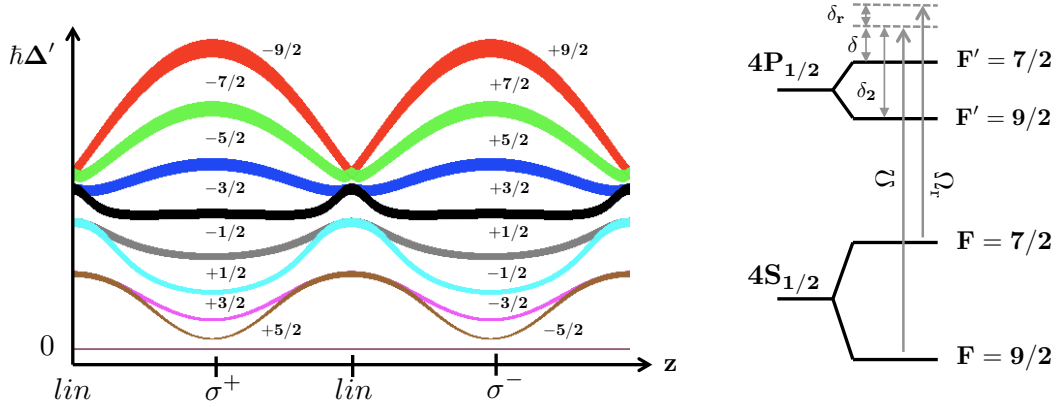


**Figure 5.8:**  $^{40}\text{K}$  D1 energy levels in  $lin \perp lin$  polarization lattice. Left) Energies of the coupled system with  $\Omega_r = 0.1\Omega$  in a blue-detuned  $lin \perp lin$  polarization lattice. Energies are broadened in proportion to the optical pumping rate  $\Gamma' = \Gamma|\Omega/\delta|^2$ . Dark states (at  $\hbar\Delta' = 0$ ) are not shifted or broadened by the light. Right)  $^{40}\text{K}$  D1 atomic level structure.

dark states into bright via a nearby excited state  $\hbar\delta_2$  away in energy:

$$\Gamma_{\text{off}} \approx \Gamma \frac{\Gamma}{\delta_2} \frac{I}{I_{\text{sat}}}. \quad (5.19)$$

As with motional coupling, the off-resonant process usually couples atoms into the bottom of the bright state potential and so does not add any energy. These two coupling processes are equal in magnitude when  $v \approx \frac{\Gamma}{k} \frac{\Gamma}{\delta_2} \frac{I}{I_{\text{sat}}}$ , corresponding to a temperature of  $50 \mu\text{K}$  for typical experimental parameters. Atoms below this temperature spend more and more time in the dark state, owing to the decrease of  $\Gamma_m$ , hence the name “gray molasses” for this type of Sisyphus cooling technique. A gray molasses is especially well-suited for the cooling of cold, dense clouds where the re-absorption of scattered photons from nearby atoms can be a limitation.

### 5.2.3 Raman-enhanced cooling

The temperature of the D1 gray molasses can be lowered if the frequency of the repump beam is chosen carefully. Our explanation of this effect follows the arguments presented in [175]. The 3-level system in Figure 6.9 represents a simplified picture of the  $\Lambda$ -coupled  $^{40}\text{K}$  D1 system in Figure 6.7. The choice of repump frequency  $\delta_r$  determines whether atoms in the dark state  $|1\rangle$  (representing  $F = 7/2$ ) are more likely to absorb into the excited state  $|3\rangle$  (representing  $F' = 7/2$ ), or into the bright state  $|2\rangle$  (representing  $F' = 9/2$ ). These two processes occur with the rates:

$$\Gamma_{1 \rightarrow 3} = \frac{\Gamma}{2} \frac{s}{1 + s + (2(\delta_r + \delta + \hbar\Delta')/\Gamma)^2}, \quad \Gamma_{1 \rightarrow 2} = \frac{\Gamma'}{2} \frac{s'}{1 + s' + (2(\delta_r - \hbar\Delta')/\Gamma')^2} \quad (5.20)$$

where  $s = 2(\Omega/\Gamma)^2$  and  $s' = 2(\Omega/\Gamma')^2$ . If the atom absorbs into  $|3\rangle$  at the top of the light-shift potential, it will immediately decay to  $|2\rangle$  in a valley. This is a cooling process as the atom has to climb the potential in order to scatter back into  $|1\rangle$ . On the other hand, the atom is most likely to scatter from  $|1\rangle$  into  $|2\rangle$  at the top of the potential where  $\Gamma'$  is largest. This is a heating process as the atom may only be pumped back into  $|1\rangle$  when at a lower point in the potential.

Different cooling behaviour is expected for different values of the repump detuning  $\delta_r$ : for  $\delta_r < 0$  and  $|\delta_r| < \Gamma$ , strong cooling is expected as the atom preferentially scatters from  $|1\rangle$  into  $|3\rangle$ ; for  $\delta_r > 0$  and  $|\delta_r| < \Gamma$ , strong heating is expected as the atom preferentially scatters from  $|1\rangle$  into  $|2\rangle$ ; for  $\delta_r < 0$  and  $\Gamma < |\delta_r| < \text{few } \Gamma$ , weak cooling is expected as the atom only slightly prefers scattering from  $|1\rangle$  into  $|3\rangle$ ; for  $\delta_r > 0$  and  $\Gamma < |\delta_r| < \text{few } \Gamma$ , weak heating is expected as the atom only weakly prefers scattering from  $|1\rangle$  into  $|2\rangle$ ; for  $|\delta_r| > \text{few } \Gamma$ , sub-Doppler cooling ceases to be effective as atoms get caught in  $|1\rangle$  without any way to couple back into  $|2\rangle$ .

### 5.3 D1 cooling observations

We present an observation of the D1 Sisyphus cooling of  $^{40}\text{K}$  atoms in two different locations in our apparatus: the MOT cell and the science chamber. Cooling in the MOT cell was investigated in order to directly compare our observations to those of Fernandes *et al.* [172]. Investigating cooling in the MOT cell before the science chamber has a few practical advantages as well. First, the ability to shine a D1 probe beam onto a continuously loaded trapped cloud of atoms and see an immediate “push” or “quench” from the D1 light allows for quick troubleshooting of the early stages of laser-locking and AOM set-up. Second, the use of an interference filter (Semrock FF01-769/41-25) aligned at the appropriate angle allows the 770 nm D1 light to be overlapped onto the 767 nm D2 beam path, obviating alignment, polarization, and power balancing work that would otherwise need to be done. Third, the short cycle time needed to load and image a MOT + molasses sequence compared with transporting and evaporatively cooling a cloud in the science chamber allows for a quick optimization of molasses parameters.

In the science chamber, D1 cooling observations are presented for atoms in free space, as well as atoms trapped in harmonic and optical lattice potentials of varying depths. We present evidence suggesting that D1 cooling used in combination with 405 nm excitation light is a promising approach towards single-site imaging of  $^{40}\text{K}$  atoms in an optical lattice.

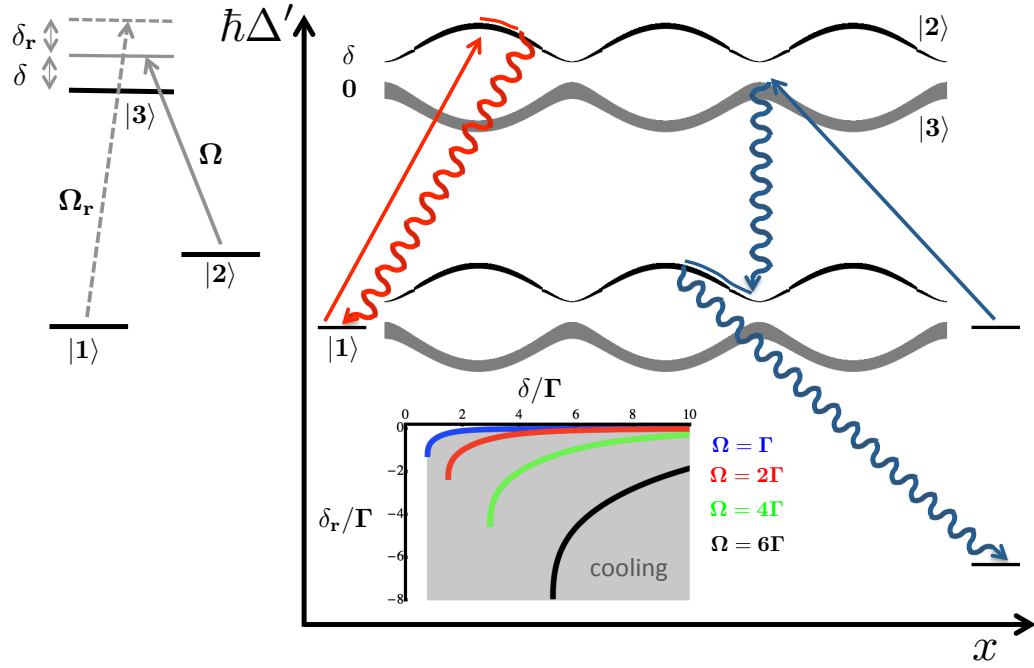


**Figure 5.9:  $\Lambda$ -cooling mechanism** Atoms in the dark state  $|1\rangle$  can either scatter into the excited state  $|3\rangle$  (blue arrow), or into the bright state  $|2\rangle$  (red arrow). For small detunings,  $\delta_r < |\Gamma|$ , scattering into  $|3\rangle$  is most likely at the top of its light-shift potential. The atom immediately decays to  $|2\rangle$  at the bottom of its light-shift potential. The atom completes the cooling cycle by scattering back into  $|1\rangle$ , something it is most likely to do after losing energy climbing near the top of the potential. Scattering into  $|2\rangle$  from  $|1\rangle$ , on the other hand, is most likely to happen at the top of the light shift potential where  $\Gamma'$  is largest. It decays back to  $|1\rangle$  at a lower point in the potential, on average, causing heating. Note that we have considered the specific case where  $\Omega$  and  $\Omega_r$  are in phase. The inset plot shows the critical detuning  $\delta_r^c$  determined from the condition  $\Gamma_{1\rightarrow 3} = \Gamma_{1\rightarrow 2}$ . For any  $\delta_r < \delta_r^c$ , cooling occurs.

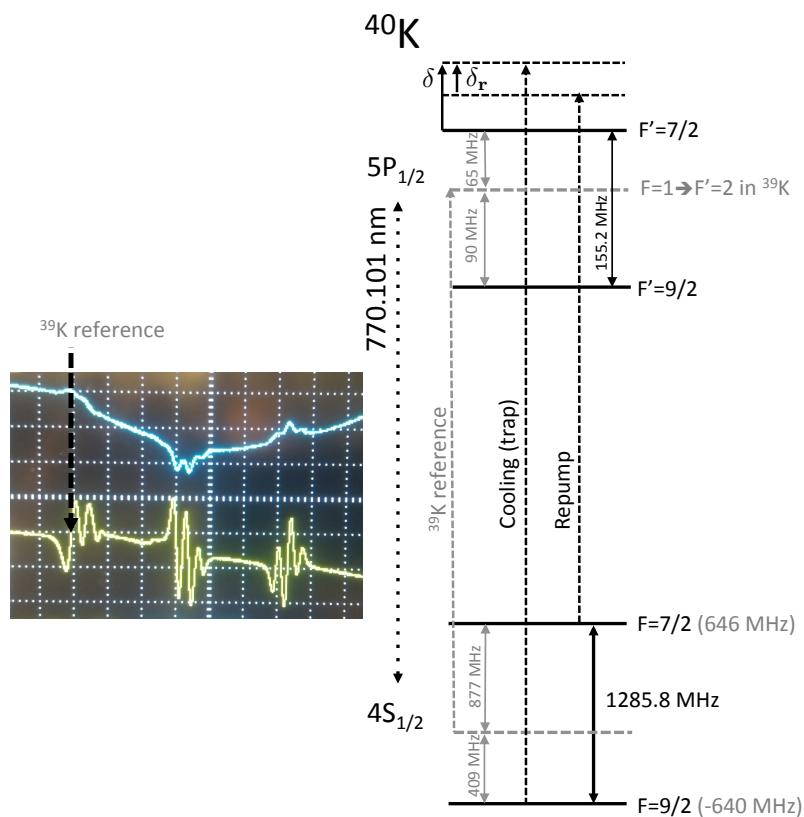


**Figure 5.10:  $^{40}\text{K}$  D1 level structure and spectroscopy:** The  $^{39}\text{K}$  Doppler-free spectroscopy signal that we use for frequency locking is shown at left. Notice that the excited state hyperfine structure is resolved. The D1 level structure is also presented, with the cooling and repump transitions identified, as well as the  $^{39}\text{K}$  reference lock frequency.

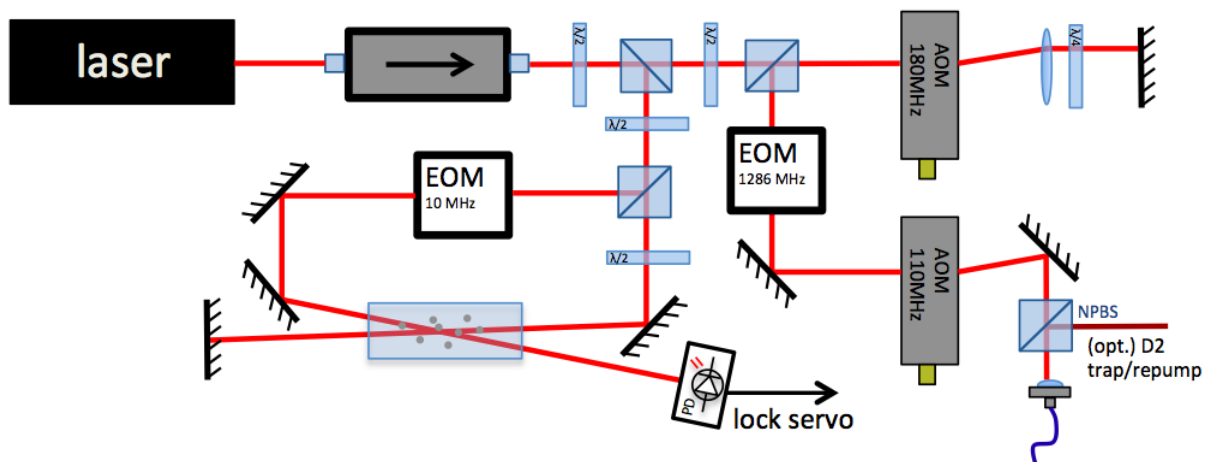


**Figure 5.11: D1 laser table schematic** 770 nm light is generated with a home-built interference filter laser. A portion of the light is used to frequency stabilize the light by sending (almost) counter-propagating beams through a K vapour cell. The probe beam is frequency modulated at 10 MHz using an EOM and the resultant photodiode signal is mixed with the 10 MHz reference in order to produce the error signal seen in figure 6.10. The remaining portion of the light is shifted by +474 MHz using a  $2 \times 180$  MHz AOM and a 110 MHz AOM. Sidebands resonant with the repump transition are generated using a 1286 MHz EOM.

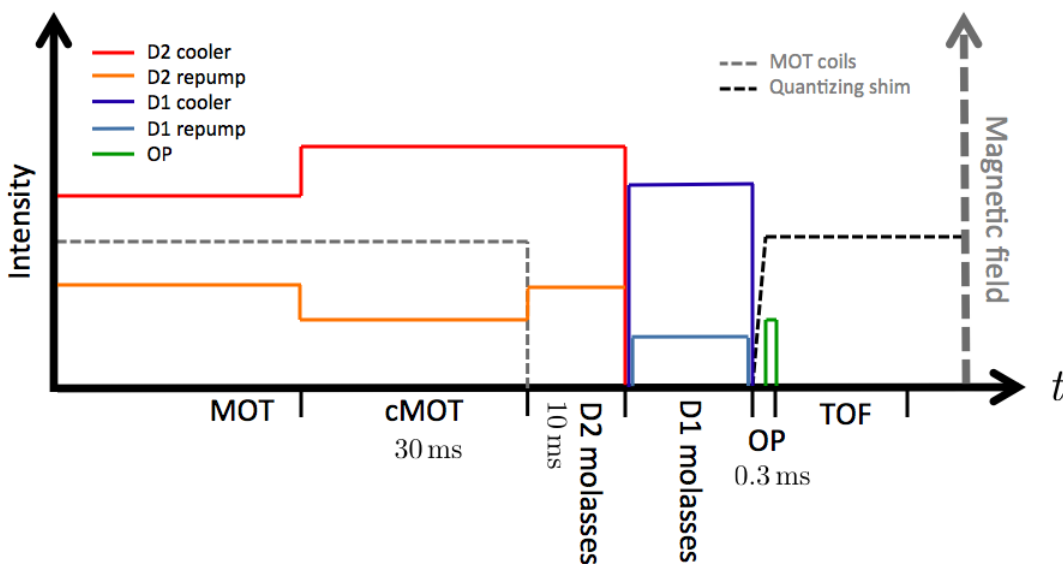


**Figure 5.12: D1 cooling sequence from MOT** Note that axes are not to scale. The D2 cooling light changes frequency between the MOT ( $\delta = -30$  MHz), cMOT ( $\delta = -10$  MHz), and molasses ( $\delta = -15$  MHz) stages.

### 5.3.1 Creation of 770 nm light

The D1 master laser is a home-built interference filter laser assembled by Simon Heun, similar to the lasers used to generate D2 light and  $^{87}\text{Rb}$  trap light [70, 181]. The laser outputs 20 mW of light, 0.5 mW of which is needed for frequency stabilization. The laser is locked to the  $F = 1 \rightarrow F' = 2$  D1 transition in  $^{39}\text{K}$  using frequency modulation spectroscopy [182]: see Figure 6.10. In contrast with D2 spectroscopy, the excited state hyperfine structure can be resolved. Figure 6.11 shows the schematic for the D1 laser system. The light needs to be shifted by +474 MHz in order to be resonant with the  $F = 9/2 \rightarrow F' = 7/2$  D1 cooling transition in  $^{40}\text{K}$ . This is done with a double-passed 180 MHz AOM and a single-passed 110 MHz AOM. Light resonant with the  $F = 9/2 \rightarrow F' = 9/2$  D1 repump transition is generated with the use of an EOM tuned to a frequency equal to the ground state hyperfine splitting  $\Delta E_{\text{HF}}/h$ . For the MOT cell experiment, a tapered amplifier was added in between the final AOM and the fiber coupler in order to boost the MOT-side power to 70 mW, corresponding to 25  $I_{\text{sat}}$  of total intensity for beams 1 cm in waist.

### 5.3.2 D1 cooling in free space

As discussed in Section 6.2, Sisyphus cooling has a low capture velocity. This means that in order for atoms to be sub-Doppler cooled, they must first be Doppler cooled. We collect  $2.5 \times 10^7$  atoms in our MOT at temperatures of around 200  $\mu\text{K}$ . We use 5  $I_{\text{sat}}$  of cooling power per beam, red-detuned by 5  $\Gamma$ , and 3  $I_{\text{sat}}$  of repump light red-detuned by 3  $\Gamma$ . The beams are  $\sigma^+/\sigma^-$  polarized and a 10 G/cm magnetic gradient is applied. After a cMOT and D2 molasses stage in which the cloud has been compressed to fit within the smaller-width D1 beams, the temperature has increased to 300  $\mu\text{K}$ .

The D2 beams are then quickly shut off as the D1 trap and repump light are turned on to  $I_{\text{cool}} = 4I_{\text{sat}}$  and  $I_{\text{repump}} = I_{\text{cool}}/10$ , respectively. The detuning is initially chosen to be  $\delta = 2\Gamma$  for the trap and  $\delta_r = 0$  repump light. Because the D1 light travels along the same path as the D2 beams, it is also  $\sigma^+/\sigma^-$  polarized. We can observe the cooling dynamics in Figure 6.13. The D1 molasses cools the 300  $\mu\text{K}$  cloud to 30  $\mu\text{K}$  within 2 ms. The cooling time shortens to 200  $\mu\text{s}$  and final temperature increases to 60  $\mu\text{K}$  with only a very slight amount of D2 repump light present. We attribute this to a “brightening” of the dark state: atoms are more quickly coupled out of the dark state to join the cooling process, but the final temperature is higher due to the increased rate of photon rescattering.

Next, we measure the number and temperature of atoms captured as a function of D1 trap detuning  $\delta$ . As shown in Figure 6.14, for  $\delta \sim \Gamma$  we capture  $2.5 \times 10^7$  atoms, the same number initially present in the MOT. The captured number v.s.  $\delta$  is peaked: too close to

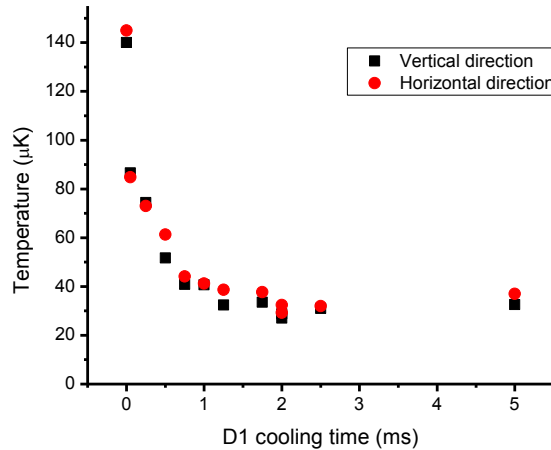


**Figure 5.13: D1 sub-Doppler cooling time:** Beginning from a  $300 \mu\text{K}$  D2 cMOT, the temperature as a function of D1 cooling time with  $\delta = 6 \text{ MHz}$  and  $\delta_r = -0.4 \text{ MHz}$ . The temperature of the cloud is seen to drop to  $80 \mu\text{K}$  within  $100 \mu\text{s}$ , taking a further 2 ms to reach an asymptotic temperature of  $30 \mu\text{K}$ . This value may be compared a previously observed asymptotic time of 6 ms [172] and a predicted value of 14 ms [183].

resonance, and atoms are heated out of the molasses; too far from resonance, and the capture velocity becomes too small. We see that the temperature behaviour is also consistent with the arguments presented in Section 6.2: the cloud cools as  $\delta$  is increased. We observe that the molasses is largely insensitive to the repump power above a 5% ratio of repump power to trap power.

Perhaps the most striking aspect of the D1 sub-Doppler cooling mechanism is the sensitivity of the final temperature to the repump detuning  $\delta_r$ . Figure 6.14 shows that by changing  $\delta_r$  from 0 to 2 MHz, we heat the cloud from  $30 \mu\text{K}$  to temperatures greater than  $180 \mu\text{K}$ . This is due to the Raman Sisyphus mechanism discussed in Section 6.2.3. When  $\delta_r < 0$ , atoms in dark states are more likely to absorb into the states with strong excited state character and undergo a cooling cycle before returning to the dark state. Conversely, when  $\delta_r > 0$  an atom is most likely to scatter via a two-photon transition directly into the bright state and be heated before returning to the dark state. Because the Raman heating and cooling mechanism relies on the presence of a polarization lattice, it is a sensitive measure of beam alignment and so can be used to optimize the alignment of the much smaller-width beams that are used for cooling in the lattice.

We notice in Figure 6.14 that the  $\delta_r$ -dependent heating and cooling mechanism is unaffected by the presence of an exciting 405 nm beam directed onto the atoms. The affect of the 405 nm light is to couple more atoms from  $F = 9/2 \rightarrow F = 7/2$ . Therefore, we do not expect a 405 nm

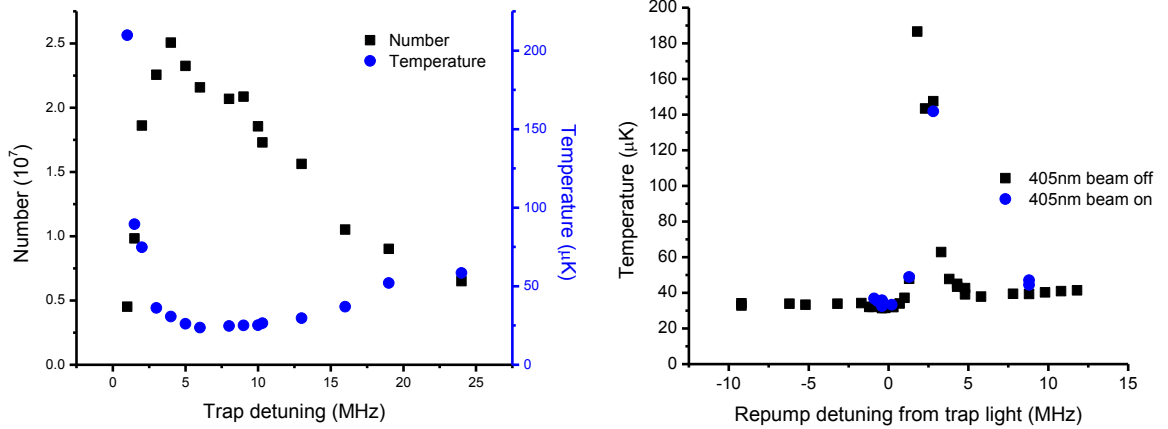


**Figure 5.14: D1 sub-Doppler detuning dependence:** Left) The number and temperature of atoms captured into a D1 molasses after 20 ms as a function of the trap detuning  $\delta$ . Right) The temperature of atoms captured into a D1 molasses after 20 ms as a function of the repump detuning  $\delta_r$ , with and without an exciting  $0.05I_{\text{sat}}$  405 nm beam. For both plots  $I_{\text{cool}} = 4I_{\text{sat}}$  and  $I_{\text{repump}}/I_{\text{cool}} = 0.1$ .

beam to ruin the dark state cooling mechanism. However, the addition of 405 nm will result in a new heating source  $(dE/dt)_{\text{heat}}^{405} = E_R^{405}\Gamma'_{405}$  that must be compensated by the cooling from the D1 molasses  $(dE/dt)_{\text{cool}}$  defined in Equation 6.16. This gives an upper bound on the allowed 405 nm scattering rate  $\Gamma'_{405}$ :

$$\Gamma'_{405} \ll \Gamma' \hbar \Delta' / E_R^{405}. \quad (5.21)$$

Finally, in order for sub-Doppler cooling to work, it must be the light field which lifts the energy degeneracy of the different Zeeman sub-levels. The presence of a magnetic field strong enough to compete with the light field  $\mu_B B \approx \hbar \Delta'$  would be expected to ruin the state-dependent light shifts and destroy the sub-Doppler cooling mechanism. Indeed, we have seen that by applying a bias magnetic field of different strengths, we increase the temperature quadratically according to  $\delta T = 100 \mu\text{K}/\text{G}^2$ .

### 5.3.3 D1 cooling in an optical lattice

Sub-Doppler cooling a cold, dense cloud of atoms in a far-detuned optical lattice involves a set of considerations not present when cooling atoms in free space. Because atoms are trapped in lattice sites separated by only 527 nm, the cloud has a number density of around  $10^{19} \text{m}^{-3}$ , compared with  $10^{14} \text{m}^{-3}$  after the MOT. This increase in density means that atoms are much more likely to be heated from the re-absorption of scattered photons from neighbouring atoms.

To avoid this process, the scattering rate  $\Gamma'$  should be kept small. In the lattice, it is the oscillation frequency  $\omega_{\text{latt}}$  that sets the kinetic energy scale. To prevent photon re-absorption, the scattering rate should be kept smaller than the lattice oscillation frequency:

$$\Gamma' < \omega_{\text{latt}}. \quad (5.22)$$

Equation 6.22 expresses the *festina lente* condition: the scattering rate must not be broadened such that it can span two vibrational levels separated by  $\omega_{\text{latt}}$ , allowing an atom to be heated by Raman scattering from one level to the next [133, 184]. Previous experiments [133] have shown that the heating from rescattered spontaneously emitted photons is negligible when the *festina lente* condition is met. For atoms at  $10 \mu\text{K}$ , the atoms are sufficiently dark to the cooling beam that it is the off-resonant coupling rate  $\Gamma_{\text{off}}$  that sets the condition in Equation 6.22. Using the expression for  $\Gamma_{\text{off}}$  defined in Equation 6.19, we get a constraint on the saturation parameter:

$$\frac{I}{I_{\text{sat}}} < \frac{\delta_2 \omega_{\text{latt}}}{\Gamma^2}. \quad (5.23)$$

Using our experimental parameters ( $\delta_2 \approx 160 \text{ MHz}$  and  $\omega_{\text{latt}} \sim 2\pi \times 200 \text{ kHz}$ ) we may evaluate the RHS of Equation 6.23, and determine that  $I/I_{\text{sat}}$  should be kept below 1. Note also that we are within the Lamb-Dicke regime  $\eta \equiv \sqrt{E_R/\hbar\omega_{\text{latt}}} < 1$  for both the  $770 \text{ nm}$  ( $\eta = 0.2$ ) and  $405 \text{ nm}$  ( $\eta = 0.4$ ) transitions in a  $200 \mu\text{K}$  deep lattice.

Another consideration when sub-Doppler cooling in a lattice is that the same light shift potential which traps atoms also causes a shift in the transition energy. A multi-level calculation of the AC Stark shift [1] shows that the  $4P_{1/2}$  state is shifted by a factor of almost 5 *up* in energy for every amount that the  $4S_{1/2}$  ground state is shifted down. This means that for a lattice of depth  $V_{\text{latt}}$ , the D1 resonance will be blue-shifted by  $6V_{\text{latt}}$ . To first order, then, the effect of the optical lattice is to make  $\delta$  position dependent:

$$\delta \approx \delta_0 - 6V_{\text{latt}} \cos^2(kz) \quad (5.24)$$

where  $\delta_0$  is the free-space detuning. We have argued that Sisyphus cooling works when the optical pumping rate  $\Gamma'$  is greatest at the top of the light shift potential  $\hbar\Delta'$ . Because  $\Gamma'$  and  $\hbar\Delta'$  have different functional dependences on the detuning  $\delta$ , the optical lattice might be expected to confuse this relationship when  $\hbar\Delta'$  becomes comparable to  $6V_{\text{latt}}$ .

Atoms at  $10 \mu\text{K}$  are trapped to within  $\sqrt{k_B T/m\omega_{\text{latt}}} \approx 35 \text{ nm}$  in a deep lattice, a distance that is small compared to the  $\lambda_{\text{D1}}/4$  polarization gradient period that an atom must traverse

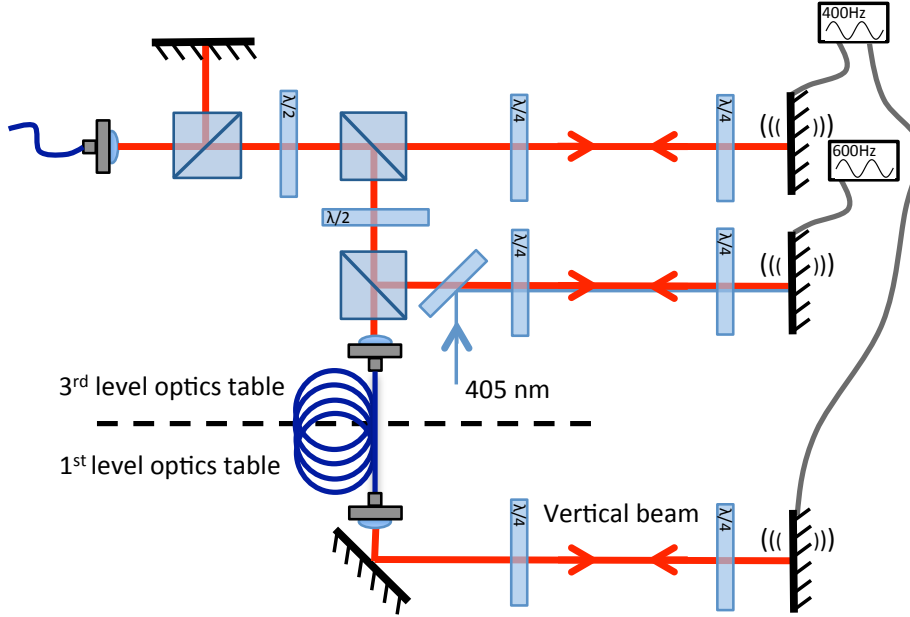


Figure 5.15: D1 lattice optics

in order to be cooled.

In order to circumvent both of these issues, we shake the polarization lattice at 400 Hz in the vertical and one of the horizontal directions, and 600 Hz in the other horizontal direction. The shaking is accomplished by placing a piezoelectric transducer onto the mirror that retro-reflects the D1 light: see Figure 6.15. The shaking rate is slow compared with  $\Gamma'$ , but fast compared with time required for imaging, and so allows us to average the Sisyphus cooling force over the polarization lattice wavelength.

### D1 lattice optics and alignment

Figure 6.15 shows the D1 optics schematic. After the fiber, we have 1.5 mW of 770 nm of light to split between the trap and repump frequencies. We control how much repump power we want by changing the amplitude of the 1286 MHz signal that is sent to the EOM. Note that the repump power comes at the expense of trap power. We choose a beam waist of 1 mm, limited by the distance between the atoms and imaging window. After transmission and coupling losses, we are left with a maximum of  $200 \mu\text{W}$  per beam, or  $4 I_{\text{sat}}$ . We choose a  $\sigma^+ - \sigma^-$  polarization configuration, similar to the free space experiment conducted in the MOT cell.

Coarse alignment of the 1 mm waist D1 beams is accomplished by making use of the large  $^{87}\text{Rb}$  atom number in the science chamber. Coupling  $^{87}\text{Rb}$  780 nm light into the fiber, we perform the first alignment iteration by attempting to heat atoms out of the lattice with a

single beam. Once this has been done individually for all (non-retro-reflected) beams, the alignment of a retro-reflected beam pair is fine-tuned by optimizing the fluorescence signal of a re-captured 1D MOT using the quadrupole coils in the science cell. This allows us to check that the polarization of the light has been set correctly. After all three retro-reflected beam pairs have been aligned using the re-captured MOT fluorescence, the beams are aligned again by optimizing the 1D, then 3D, fluorescence signal after a re-captured molasses stage. This alignment procedure accounts for any spatial differences between the magnetic field zero of the quadrupole coils and optical lattice trap.

Having aligned the beams to this point using a  $^{87}\text{Rb}$  signal, we switch to 770 nm  $^{40}\text{K}$  light for final alignment stage. With the D1 light, we can no longer optimize alignment using a fluorescent signal as the D1 light shelves atoms into a dark state. Instead, we can use absorption imaging to align the beams so that the atom cloud is symmetrically “pushed” (for a single beam) or “squeezed” (for a retro-reflected pair). Finally, we measure whether we have aligned the beams well-enough to create a polarization lattice by changing the repump detuning  $\delta_r$  to observe the heating and cooling mechanisms described in Section 6.2.3.

### D1 lattice cooling sequence and results

The lattice cooling experiment is performed after evaporating a cloud of  $5 \times 10^4$   $^{40}\text{K}$  atoms to approximately 200 nK in the cross-dipole trap. Before loading the  $^{40}\text{K}$  atoms into the lattice, the  $F = 1$   $^{87}\text{Rb}$  coolant atoms are removed by applying a 5 ms pulse of trap and repump light. The optical lattice is then ramped on in 250 ms to a final depth between 0 and 200  $\mu\text{K}$ . The 20 G quantizing field is ramped off slowly (50 ms) in order to prevent eddy currents in the surrounding metal chamber. If measurements are being made using absorption imaging, we have found that it is important to pulse (0.5 ms) a D2 repump and optical pumping beam onto the atoms in order to efficiently image them.

We measure the equilibrium temperature of atoms after 20 ms of D1 cooling as a function of the lattice depth. This is done by fitting the width after time-of-flight after a diabatic (see Equation 5.80) shut-off of the lattice. For zero lattice depth, we surpass our free-space results from the proof-of-principle experiment in Section 6.3 and achieve a temperature of 16  $\mu\text{K}$ . This could be the result of better magnetic field zeroing and better stray-light shielding. We observe that increasing the lattice depth lowers the temperature of the laser-cooled atoms slightly to 10-12  $\mu\text{K}$ .

Figure 6.17 shows a plot of the *in situ* temperature v.s. repump detuning  $\delta_r$  for atoms trapped in an crossed dipole trap and a 200  $\mu\text{K}$  lattice. We can see that the temperature has the same qualitative dependence on  $\delta_r$  as in the free-space results plotted in Figure 6.14. That

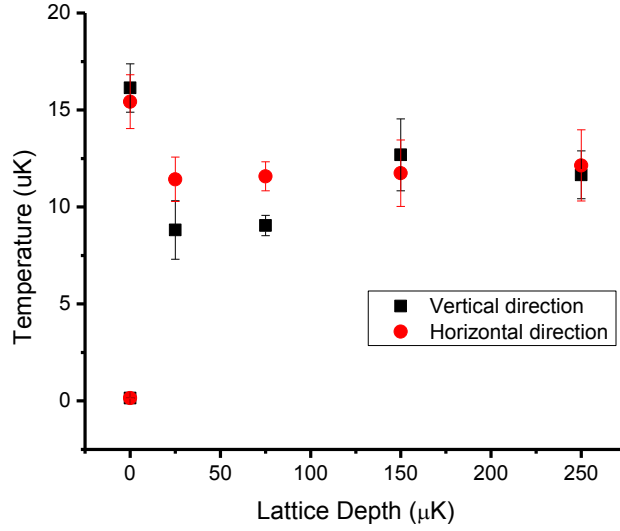


**Figure 5.16: Temperature v.s. lattice depth:** Approximately  $10^5$   $^{40}\text{K}$  atoms are cooled to 200 nK in a crossed dipole trap (XDT) and then loaded into an optical lattice of varying depth. 20 ms of D1 cooling light is then applied and the temperature is then measured by fitting the width of the cloud after time of flight. The data points at 0  $\mu\text{K}$  lattice depth show the initial temperature of the cloud (200 nK) and the temperature of the cloud after D1 cooling in free space (16  $\mu\text{K}$ ).

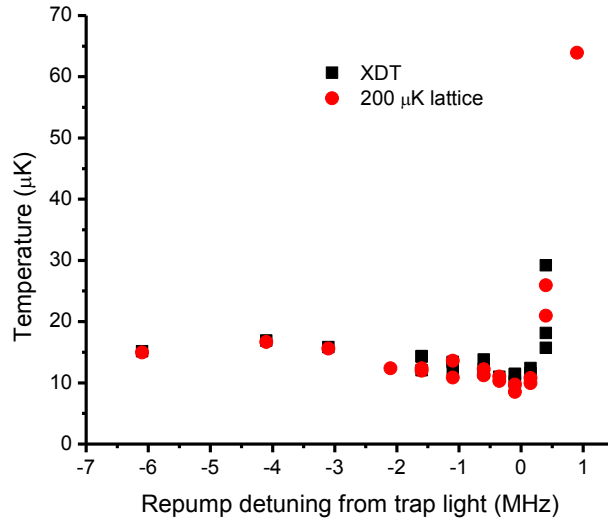


**Figure 5.17: *In situ* temperature v.s. repump detuning:** Approximately  $10^5$   $^{40}\text{K}$  atoms are cooled to 200 nK in a crossed dipole trap (XDT). We may then load the atoms into an optical lattice (or not). We then apply 20 ms of D1 cooling light for various repump beam detunings  $\delta_r$  and then measure the temperature after time of flight imaging.

is, the presence of the optical lattice does not destroy the Raman Sisyphus cooling mechanism.

In addition, we have observed that it is possible to continuously collect fluorescence from lattice trapped atoms when simultaneously D1 cooling and exciting using a low-power 405 nm beam. This preliminary data suggests that using both 770 nm and 405 nm light for cooling and imaging represents a promising approach towards the high-resolution imaging of  $^{40}\text{K}$  atoms in an optical lattice.

## Chapter 6

# Conclusion and Outlook

We have designed, built, rebuilt, tested, and demonstrated full functionality of an apparatus with the capability of imaging individual  $^{40}\text{K}$  atoms that have been loaded into an optical lattice. We have created low-entropy states of matter that, when loaded into an optical lattice potential, simulate the Hubbard model. We have described a novel approach to the problem of imaging  $^{40}\text{K}$  with single-site resolution: combining a gray sub-Doppler laser cooling with fluorescence from the  $5P_{3/2} \rightarrow 4S_{1/2}$  excited state transition. Here we summarize the main results of this thesis.

**A new ultracold atoms apparatus for  $^{40}\text{K}$  and  $^{87}\text{Rb}$ :** The design and construction of a new apparatus for cooling and magnetically transporting a cloud of  $^{87}\text{Rb}$  and  $^{40}\text{K}$  atoms is presented in Chapter 2. In particular, we outline the particular benefits and challenges encountered in our vacuum system design, magnetic transport system design, and choice of atomic species for evaporation. We have found that the most reliable way to attain a high vapour pressure of  $^{40}\text{K}$  is through a home-made dispenser source. Having a well-studied and abundant boson such as  $^{87}\text{Rb}$  that is able to sympathetically cool  $^{40}\text{K}$  has proven invaluable in trouble-shooting all aspects of the apparatus. The magnetic transport of  $^{87}\text{Rb}$  and  $^{40}\text{K}$  along the axial direction of a set of coils has been shown to be well-suited for an apparatus that prizes optical access. The sympathetic evaporation of  $^{87}\text{Rb}$  and  $^{40}\text{K}$  atoms in a quadrupole, plugged quadrupole, and crossed dipole trap has been performed less than 1 mm from air, at the focus of a high-NA imaging system. We have described the experimental sequence developed in the lab, and provided alignment and trouble-shooting suggestions that we have found to be helpful in optimizing the performance of our apparatus.

**A quantum gas of  $^{40}\text{K}$  and  $^{87}\text{Rb}$ :** In Chapter 3 we outlined the thermodynamics describing a quantum gas of bosons and fermions. In particular, we described the density distributions expected for  $^{87}\text{Rb}$  and  $^{40}\text{K}$  in a harmonic trap. We described the plugged quadrupole potential

and used it to evaporate of  $^{87}\text{Rb}$  to quantum degeneracy. Evaporation of both  $^{87}\text{Rb}$  and  $^{40}\text{K}$  in a crossed dipole trap was observed, and we observed the importance of transferring  $^{87}\text{Rb}$  to its lowest hyperfine ground state in order to protect against spin relaxation processes.

**A 405 nm MOT for  $^{40}\text{K}$ :** Chapter 4 provides an observation of Doppler cooling along the  $4S_{1/2} \rightarrow 5P_{3/2}$  transition in  $^{40}\text{K}$ . We chose to explore cooling on this transition due to its narrow linewidth compared and the possibility of capturing high frequency photons for single-site fluorescence imaging. We observed a minimum temperature of  $63(6) \mu\text{K}$  and an increase phase space density by a factor of twenty in the MOT. When cooling without a magnetic gradient present, the lowest temperature that we observed was  $85 \mu\text{K}$ .

**Optical lattices for  $^{40}\text{K}$  and  $^{87}\text{Rb}$ :** The energies and states of atoms loaded into an optical lattice potential were calculated in Chapter 5. In particular, we derived the Hubbard model for a gas of cold atoms with short-range interactions in the lowest band of the optical lattice. We described our experimental implementation of an optical lattice, including high-power fiber coupling, optics layout, and beam alignment procedures. We present an observation of the  $^{87}\text{Rb}$  superfluid-to-Mott insulator phase transition as a demonstration of our capability to create a quantum many-body state in an optical lattice. We also observed the site-localization of  $^{40}\text{K}$  atoms in an optical lattice as an example of a state that is ripe for probing with a single-site imaging tool.

**High-resolution imaging and  $^{40}\text{K}$  sub-Doppler cooling:** We present an approach to the single-site imaging of  $^{40}\text{K}$  in Chapter 6. We develop an intuitive criteria for determining the objective NA required for determining the optical lattice site occupancy. The imaging objective is characterized by imaging a nano hole array, 500 nm pinhole, and reflective target through a  $200 \mu\text{m}$ -thick sapphire window. We investigated the gray Sisyphus cooling of  $^{40}\text{K}$  on the D1 transition, observing a minimum laser cooled temperature of  $16 \mu\text{K}$  in free space, and  $12 \mu\text{K}$  in a  $250 \mu\text{K}$ -deep optical lattice potential. We observed that the cooling mechanism is not destroyed when exciting the sample of atoms with 405 nm light.

**Outlook:** In the near future, we expect this apparatus to contribute towards a better understanding of locally ordered states described by the Fermi-Hubbard model. In particular, we are curious about the equilibration rates of Band insulating and Mott insulating states, the onset of anti-ferromagnetic correlations, and the use of a single-site probe as a sensitive thermometer to develop novel cooling techniques. We also expect this apparatus to be a useful tool in exploring a broad range of bosonic and fermionic systems at the local level.

# Appendix A

## Atoms in Electromagnetic fields

### A.1 Atom in a Magnetic field

In the presence of a magnetic field, there are four terms in the Hamiltonian of hydrogen-like atoms,

$$\hat{H}_0 = \hat{H}_{\text{el}} + \hat{H}_{\text{FS}} + \hat{H}_{\text{HF}} + \hat{H}_Z, \quad (\text{A.1})$$

where  $\hat{H}_{\text{el}}$  contains the non-relativistic kinetic energy of the electrons and the Coulomb interaction between them;  $\hat{H}_{\text{FS}}$  is the fine structure term that accounts for the interaction between an electron's spin  $\hat{\mathbf{S}}$  and orbital angular momentum  $\hat{\mathbf{L}}$ ;  $\hat{H}_{\text{HF}}$  is the hyperfine structure term induced by the interaction of the nuclear magnetic moment  $\hat{\mathbf{I}}$  and the total electronic angular momentum  $\hat{\mathbf{J}}$ ; and  $\hat{H}_Z$  describes the interaction between the magnetic of the atom and an external magnetic field. The energy contributions of  $\hat{H}_{\text{el}}$  and  $\hat{H}_{\text{FS}}$  are of order hundreds of THz and a few THz, respectively, much larger than the MHz - GHz scales of  $\hat{H}_Z$  and  $\hat{H}_{\text{HF}}$  which can mix in strong magnetic fields. When considering the behaviour an atom in a magnetic field, we will therefore restrict ourselves to the Hamiltonian:

$$\hat{H}_{\text{mag}} = \hat{H}_{\text{HF}} + \hat{H}_Z. \quad (\text{A.2})$$

For atoms with nonzero nuclear and electronic spin,  $\hat{H}_{\text{HF}}$  splits the ground states:

$$\hat{H}_{\text{HF}} = \frac{A_{\text{HF}}}{\hbar^2} \hat{\mathbf{I}} \cdot \hat{\mathbf{J}} + \frac{B_{\text{HF}}}{\hbar^2} \frac{3(\hat{\mathbf{I}} \cdot \hat{\mathbf{J}})^2 + \frac{3}{2}(\hat{\mathbf{I}} \cdot \hat{\mathbf{J}}) - \hat{\mathbf{I}}^2 \hat{\mathbf{J}}^2}{2I(2I-1)J(2J-2)}, \quad (\text{A.3})$$

with  $A_{\text{HF}}$  the magnetic dipole constant and  $B_{\text{HF}}$  the electric quadrupole constant. Using the identity  $\hat{\mathbf{I}} \cdot \hat{\mathbf{J}} = 1/2(\hat{\mathbf{F}}^2 - \hat{\mathbf{I}}^2 - \hat{\mathbf{J}}^2)$ , we may find the energy splitting between  $J = \pm 1/2$  states

of the  $S = 1/2$  ground state manifold:

$$\Delta E_{\text{HF}} = \frac{A_{\text{HF}}}{2} \left( I + \frac{1}{2} \right). \quad (\text{A.4})$$

For  $^{87}\text{Rb}$ ,  $A_{\text{HF}} = 2\pi\hbar \times 3.417\,341\,305\,45215(5)$  GHz and  $I = 3/2$ , giving  $\Delta E_{\text{HF}} \approx 2\pi\hbar \times 6.834\,682$  GHz. For  $^{40}\text{K}$ ,  $A_{\text{HF}} = -2\pi\hbar \times 285.730\,8(24)$  MHz and  $I = 4$ , giving  $\Delta E_{\text{HF}} \approx 2\pi\hbar \times 1.285\,785$  GHz [56].

The Zeeman Hamiltonian  $\hat{H}_Z$  describes the interaction of the atom with an external magnetic field  $\mathbf{B}$ :

$$\hat{H}_Z = \frac{\mu_B}{\hbar} (g_J \hat{\mathbf{J}} + g_I \hat{\mathbf{I}}) \cdot \mathbf{B}, \quad (\text{A.5})$$

where  $g_J$  is the Landé  $g$ -factor of the electron and  $g_I$  is the  $g$ -factor of the nucleus. In  $^{87}\text{Rb}$  the  $S = 1/2$  ground state,  $g_J = 2.002\,331\,13(20)$  and  $g_I = -0.000\,995\,141\,4(10)$ , while in ground state of  $^{40}\text{K}$ ,  $g_J = 2.002\,94,1(24)$  and  $g_I = 0.000\,176\,490(34)$  [56]. Because  $g_I \ll g_J$ , the interaction between the nucleus and the external magnetic field is negligible compared to that of the electron, and so may be neglected in  $\hat{H}_Z$ .

Using this approximation, we may then calculate the eigenvalues of  $\hat{H}_{\text{mag}}$  defined in Equation A.2 using the Breit-Rabi formula [185]:

$$\frac{E}{\Delta E_{\text{HF}}} = -\frac{1}{4F_+} \pm \frac{1}{2} \sqrt{1 + 2\frac{m_F}{F_+}x + x^2}, \quad (\text{A.6})$$

where  $x = g_J \mu_B B / \Delta E_{\text{HF}}$ ,  $m_F = m_I \pm 1/2$  is the magnetic quantum number (projection of total angular momentum along the field axis),  $B = |\mathbf{B}|$  is the magnitude of the field,  $\Delta E_{\text{HF}}$  is the hyperfine splitting, given in Equation A.4, and  $F_+ = i + 1/2$ .<sup>1</sup>

For weak magnetic fields, the magnetic dipole term  $\hat{H}_Z$  can be treated as a perturbation, and the Zeeman shifts are linear:  $\partial E / \partial B \rightarrow g_F m_F \mu_B$ , where  $g_F$  is the Landé factor. For ground states of alkalis,  $g_F = \pm 1/F_+$ , such that the *stretched state* has the moment of one  $\mu_B$ .

The Breit-Rabi equation also gives the Zeeman energy at higher fields. The deviation from linearity is called the quadratic Zeeman shift, and is proportional to  $(\mu_B B)^2 / \Delta E_{\text{HF}}$ . At very high fields,  $B \gg \Delta E_{\text{HF}} / \mu_B$ , the magnetic dipole term is the dominant effect. With the hyperfine interaction now treated as a perturbation, the atomic levels become increasingly well described

<sup>1</sup>There is a sign ambiguity in the square root. When  $m_F = F_+$  the  $\pm \frac{1}{2} \sqrt{\dots}$  term should be replaced by  $+\frac{1}{2}(1+x)$ ; and when  $m_F = -F_+$  the same term should be replaced by  $+\frac{1}{2}(1-x)$ . We have neglected the interaction of the nuclear magnetic moment with the external field in this formula (ie, taken  $g_i = 0$ ), but still retain  $i$  and  $m_i$  as quantum numbers affecting the hyperfine energy and projection of the electronic spin. To calculate microwave transitions to a precision better than 1%, these terms should be added back in: add a term  $+(m_F x)/(g_J/g_I - 1)$  to the energy, and replace  $g_J$  with  $(g_J - g_I)$  in  $x$ .

by the quantum numbers  $m_J$  and  $m_I$ , these being the individual spin projections of the electron and nuclear angular momenta. Since the magnetic moment of the electron is much larger than that of the nucleus, the energy states break up into a higher-energy set of  $m_F = +1/2$  (spin up) eigenstates and a lower-energy set of  $m_J = -1/2$  (spin-down) eigenstates. In this regime,  $E \rightarrow m_J g_J \mu_B B + A_{\text{HF}} m_J m_I$ . In each  $m_J$  set, level spacing is  $A_{\text{HF}}$ .

## A.2 Atom in an Electric field

An atom is polarizable. Take the Alkali atom, for instance: one electron orbiting around a collection of closed shell electrons and a positively charged nucleus, functioning effectively like a Hydrogen atom. The internal ground state of this atom is an  $nS$  state with  $l = 0$  angular momentum, the electron orbiting the nucleus with perfect symmetry. This symmetry can be broken if an electric field is applied, resulting in an induced dipole moment between the electron and the positively charged core proportional to the electric field  $\mathbf{p}(\omega) = \alpha(\omega) \mathbf{E}$ . The proportionality constant  $\alpha(\omega)$  is the complex polarizability which depends on the frequency  $\omega$  of the electric field.

The polarizability can be calculated by considering a classical model of an electron with mass  $m_e$  bound to an atom with an oscillation frequency  $\omega_0$  and damping rate  $\Gamma_\omega$  and driven by an electric field:  $\ddot{x} + \Gamma_\omega \dot{x} + \omega_0^2 x = -eE/m_e$ . The classical oscillation frequency  $\omega_0$  corresponds to the atomic transition frequency whereas the classical damping rate  $\Gamma_\omega = e^2 \omega^2 / 6\pi \epsilon_0 m_e c^3$  is due to the radiative energy loss experienced by the electron and related to the atomic transition linewidth via  $\Gamma = \omega_0^2 / \omega^2 \Gamma_\omega$ . Integrating for  $x$  yields the polarizability

$$\alpha(\omega) = \frac{x e}{E} = \frac{e^2}{m_e} \frac{1}{\omega_0^2 - \omega^2 - i\omega \Gamma_\omega}. \quad (\text{A.7})$$

We see right away that  $\alpha(\omega)$  is complex. A simple check also tells us that the real part of  $\alpha(\omega)$  will dominate the atom's behaviour in the limit when  $(\omega_0^2 - \omega^2)^2 \gg \omega^2 \Gamma_\omega^2$ . This limit describes the *off-resonant* light-matter interaction regime in which the atom interacts dispersively, and without energy loss, with the field, acquiring an energy shift proportional to the intensity  $I(\mathbf{r})$ :

$$V_{\text{dip}}(\mathbf{r}) = -\frac{1}{2} \langle \vec{p} \cdot \vec{E} \rangle = -\frac{1}{2} \text{Re}(\alpha(\omega)) I(\mathbf{r}). \quad (\text{A.8})$$

In limit where the imaginary part of the polarizability  $\alpha(\omega)$  dominates,  $(\omega_0^2 - \omega^2)^2 \ll \omega^2 \Gamma_\omega^2$ , the atom radiates energy away by scattering photons, doing so at a rate:

$$\Gamma_{\text{sc}}(\mathbf{r}) = \langle \dot{\vec{p}} \cdot \vec{E} \rangle = \frac{1}{\hbar \epsilon_0 c} \text{Im}(\alpha(\omega)) I(\mathbf{r}). \quad (\text{A.9})$$

This is the *resonant* light-matter interaction regime. Note that there is different detuning ( $\Delta \equiv \omega - \omega_0$ ) dependence between the potential energy and the scattering rate: whereas  $V_{\text{dip}} \propto I(\mathbf{r})/\Delta$ ,  $\Gamma_{\text{sc}} \propto I(\mathbf{r})\Gamma/\Delta^2$ . For this reason, if the optical power is available, far-detuned optical traps are generally preferable to near-detuned traps due to the reduced photon scattering and associated heating.

Real atoms have more than two states, and thus more than one transition frequency  $\omega_0$ . Including the  $D_1$  and  $D_2$  excited states present in both  $^{87}\text{Rb}$  and  $^{40}\text{K}$ , we can derive an expression for the dipole potential [186]:

$$V_{\text{dip}}(\mathbf{r}) = \frac{\pi c^2}{2} \left( \frac{2\Gamma_{D_2}}{\omega_{D_2}^3} \left( \frac{1}{\Delta_{D_2}} - \frac{1}{\Delta_{D_1} + 2\omega_{D_2}} \right) + \frac{\Gamma_{D_1}}{\omega_{D_1}^3} \left( \frac{1}{\Delta_{D_1}} - \frac{1}{\Delta_{D_1} + 2\omega_{D_2}} \right) \right) I(\mathbf{r}) \quad (\text{A.10})$$

where  $\{\Gamma_{D_1}, \omega_{D_1}, \Delta_{D_1} \equiv \omega - \omega_{D_1}\}$  and  $\{\Gamma_{D_2}, \omega_{D_2}, \Delta_{D_2} \equiv \omega - \omega_{D_2}\}$  are the line widths, transition frequency, and detuning of the  $D_1$  and  $D_2$  states, respectively. The  $D_2$  line contributes twice as much to the dipole potential as the  $D_1$  line owing to its greater line strength factor.

When understanding optical dipole traps, the conceptual point that should not be lost is that an induced dipole moment allows an atom to lower its energy *as long as the electromagnetic field is changing slowly enough for the atom to respond*. The response rate of the atom to an electromagnetic field is given by the transition frequency. Inspecting Equation A.10, we can see that when the field frequency is lower than the transition frequency,  $\Delta$  and  $V_{\text{dip}}(\mathbf{r})$  are negative and so atoms prefer to be in regions of high intensity. The opposite is true when the field frequency is greater than the transition frequency. In this case, atoms are repelled from regions of high intensity since they are not able to respond quickly enough and so are out of phase with the driving field.

# Bibliography

- [1] David McKay. *Quantum simulation in strongly correlated optical lattices*. PhD thesis, University of Illinois at Urbana-Champaign, 2013.
- [2] Nir Navon, Sylvain Nascimbène, Frédéric Chevy, and Christophe Salomon. The equation of state of a low-temperature fermi gas with tunable interactions. *Science*, 328(5979):729–732, 2010.
- [3] Mark JH Ku, Ariel T Sommer, Lawrence W Cheuk, and Martin W Zwierlein. Revealing the superfluid lambda transition in the universal thermodynamics of a unitary fermi gas. *Science*, 335(6068):563–567, 2012.
- [4] Chen-Lung Hung, Victor Gurarie, and Cheng Chin. From cosmology to cold atoms: Observation of sakharov oscillations in a quenched atomic superfluid. *science*, 341(6151):1213–1215, 2013.
- [5] Manuel Endres, Takeshi Fukuhara, David Pekker, Marc Cheneau, Peter Schauß, Christian Gross, Eugene Demler, Stefan Kuhr, and Immanuel Bloch. The/higgs/'amplitude mode at the two-dimensional superfluid/mott insulator transition. *Nature*, 487(7408):454–458, 2012.
- [6] Ariel Sommer, Mark Ku, Giacomo Roati, and Martin W Zwierlein. Universal spin transport in a strongly interacting fermi gas. *Nature*, 472(7342):201–204, 2011.
- [7] Marco Koschorreck, Daniel Pertot, Enrico Vogt, and Michael Köhl. Universal spin dynamics in two-dimensional fermi gases. *Nature Physics*, 9(7):405–409, 2013.
- [8] AB Bardon, S Beattie, C Luciuk, W Cairncross, D Fine, NS Cheng, GJA Edge, E Taylor, S Zhang, S Trotzky, et al. Transverse demagnetization dynamics of a unitary fermi gas. *arXiv preprint arXiv:1310.5140*, 2013.

- [9] Waseem S. Bakr, Jonathon I. Gillen, Amy Peng, Simon Fölling, and Markus Greiner. A quantum gas microscope for detecting single atoms in a hubbard-regime optical lattice. *Nature*, 462:74, 2009.
- [10] Jacob F. Sherson, Christof Weitenberg, Manuel Endres, Marc Cheneau, Immanuel Bloch, and Stefan Kuhr. Single-atom-resolved fluorescence imaging of an atomic mott insulator. *Nature*, 467:68, 2010.
- [11] Jonathan Simon, Waseem S Bakr, Ruichao Ma, M Eric Tai, Philipp M Preiss, and Markus Greiner. Quantum simulation of antiferromagnetic spin chains in an optical lattice. *Nature*, 472(7343):307–312, 2011.
- [12] DA Bonn. Are high-temperature superconductors exotic? *Nature Physics*, 2(3):159–168, 2006.
- [13] Richard P Feynman. Simulating physics with computers. *International journal of theoretical physics*, 21(6):467–488, 1982.
- [14] Walter Hofstetter, JI Cirac, Peter Zoller, Eugene Demler, and MD Lukin. High-temperature superfluidity of fermionic atoms in optical lattices. *Physical review letters*, 89(22):220407, 2002.
- [15] Michael Köhl, Henning Moritz, Thilo Stöferle, Kenneth Günter, and Tilman Esslinger. Fermionic atoms in a three dimensional optical lattice: Observing fermi surfaces, dynamics, and interactions. *Physical review letters*, 94(8):080403, 2005.
- [16] Robert Jördens, Niels Strohmaier, Kenneth Günter, Henning Moritz, and Tilman Esslinger. A mott insulator of fermionic atoms in an optical lattice. *Nature*, 455(7210):204–207, 2008.
- [17] U Schneider, L Hackermüller, S Will, Th Best, I Bloch, TA Costi, RW Helmes, D Rasch, and A Rosch. Metallic and insulating phases of repulsively interacting fermions in a 3d optical lattice. *Science*, 322(5907):1520–1525, 2008.
- [18] SS Kondov, WR McGehee, and B DeMarco. Interplay of disorder and interactions in an optical lattice hubbard model. *arXiv preprint arXiv:1305.6072*, 2013.
- [19] DC McKay and B DeMarco. Cooling in strongly correlated optical lattices: prospects and challenges. *Reports on Progress in Physics*, 74(5):054401, 2011.

- [20] Nathan Gemelke, Xibo Zhang, Chen-Lung Hung, and Cheng Chin. In situ observation of incompressible mott-insulating domains in ultracold atomic gases. *Nature*, 460(7258):995–998, 2009.
- [21] Karl D Nelson, Xiao Li, and David S Weiss. Imaging single atoms in a three-dimensional array. *Nature Physics*, 3(8):556–560, 2007.
- [22] Christof Weitenberg. *Single-atom resolved imaging and manipulation in an atomic Mott insulator*. PhD thesis, lmu, 2011.
- [23] Michael Feld, Bernd Fröhlich, Enrico Vogt, Marco Koschorreck, and Michael Köhl. Observation of a pairing pseudogap in a two-dimensional fermi gas. *Nature*, 480(7375):75–78, 2011.
- [24] Zoran Hadzibabic, Peter Krüger, Marc Cheneau, Baptiste Battelier, and Jean Dalibard. Berezinskii–kosterlitz–thouless crossover in a trapped atomic gas. *Nature*, 441(7097):1118–1121, 2006.
- [25] Chen-Lung Hung, Xibo Zhang, Nathan Gemelke, and Cheng Chin. Observation of scale invariance and universality in two-dimensional bose gases. *Nature*, 470(7333):236–239, 2011.
- [26] Xibo Zhang, Chen-Lung Hung, Shih-Kuang Tung, and Cheng Chin. Observation of quantum criticality with ultracold atoms in optical lattices. *Science*, 335(6072):1070–1072, 2012.
- [27] Chad N Weiler, Tyler W Neely, David R Scherer, Ashton S Bradley, Matthew J Davis, and Brian P Anderson. Spontaneous vortices in the formation of bose–einstein condensates. *Nature*, 455(7215):948–951, 2008.
- [28] Sebastian Will, Thorsten Best, Simon Braun, Ulrich Schneider, and Immanuel Bloch. Coherent interaction of a single fermion with a small bosonic field. *Physical review letters*, 106(11):115305, 2011.
- [29] Sebastian Will, Thorsten Best, Ulrich Schneider, Lucia Hackermüller, Dirk-Sören Lühmann, and Immanuel Bloch. Time-resolved observation of coherent multi-body interactions in quantum phase revivals. *Nature*, 465(7295):197–201, 2010.
- [30] K-K Ni, S Ospelkaus, MHG De Miranda, A Pe’er, B Neyenhuis, JJ Zirbel, S Kotochigova, PS Julienne, DS Jin, and J Ye. A high phase-space-density gas of polar molecules. *science*, 322(5899):231–235, 2008.

- [31] J T M Walraven. Atomic hydrogen in magnetostatic traps. In G-L Oppo, SM Barnett, E Riis, and M Wilkinson, editors, *Proc Scott Univ Summer Sch Phys*, volume 44, pages 315–352. Institute of Physics, 1996.
- [32] W. Ketterle and N. J. van Druten. Evaporative cooling of trapped atoms. *Adv. in At., Mol. and Opt. Phys.*, 37:181–236, 1996.
- [33] Christopher Pethick and Henrik Smith. *Bose-Einstein condensation in dilute gases*. Cambridge university press, 2002.
- [34] W. Ketterle, D. S. Durfee, and D. M. Stamper-Kurn. Making, probing and understanding Bose Einstein condensates. In M. Inguscio, S. Stringari, and C. E. Wieman, editors, *Bose Einstein condensation in atomic gases, Proc. of the Int. School of Phys. Enrico Fermi*, volume CXL, pages 67–176, 1999.
- [35] Y. Castin. Trapped Fermi gases. In M. Inguscio, W. Ketterle, and C. Salomon, editors, *Proc. of the Int. School of Phys. Enrico Fermi*, volume CLXIV, pages 289–349, 2008.
- [36] W. Ketterle and M. W. Zwierlein. Making, probing and understanding ultracold Fermi gases. In M. Inguscio, W. Ketterle, and C. Salomon, editors, *Proc. of the Int. School of Phys. Enrico Fermi*, volume CLXIV, pages 247–422, 2008.
- [37] Michal Karski, Leonid Förster, Jai-Min Choi, Andreas Steffen, Wolfgang Alt, Dieter Meschede, and Artur Widera. Quantum walk in position space with single optically trapped atoms. *Science*, 325(5937):174–177, 2009.
- [38] Marc Cheneau, Peter Barmettler, Dario Poletti, Manuel Endres, Peter Schauß, Takeshi Fukuhara, Christian Gross, Immanuel Bloch, Corinna Kollath, and Stefan Kuhr. Light-cone-like spreading of correlations in a quantum many-body system. *Nature*, 481(7382):484–487, 2012.
- [39] Jean-Philippe Brantut, Jakob Meineke, David Stadler, Sebastian Krinner, and Tilman Esslinger. Conduction of ultracold fermions through a mesoscopic channel. *Science*, 337(6098):1069–1071, 2012.
- [40] Wolfgang Pauli. *Exclusion principle and quantum mechanics*. Springer, 1994.
- [41] Wolfgang Pauli. The connection between spin and statistics. *Physical Review*, 58(8):716, 1940.
- [42] Bruder-C. Cirac J. I. Gardiner C. W. Jaksch, D. and P. Zoller. Cold bosonic atoms in optical lattices.

- [43] Jun John Sakurai and San Fu Tuan. *Modern quantum mechanics*, volume 104. Addison-Wesley Reading (Mass.), 1994.
- [44] B DeMarco, JL Bohn, JP Burke Jr, M Holland, and DS Jin. Measurement of p-wave threshold law using evaporatively cooled fermionic atoms. *Physical review letters*, 82(21):4208, 1999.
- [45] Christopher Ticknor, CA Regal, DS Jin, and JL Bohn. Multiplet structure of feshbach resonances in nonzero partial waves. *Physical Review A*, 69(4):042712, 2004.
- [46] EGM Van Kempen, SJJMF Kokkelmans, DJ Heinzen, and BJ Verhaar. Interisotope determination of ultracold rubidium interactions from three high-precision experiments. *Physical review letters*, 88(9):093201, 2002.
- [47] Y-J Lin, Rob L Compton, K Jimenez-Garcia, James V Porto, and Ian B Spielman. Synthetic magnetic fields for ultracold neutral atoms. *Nature*, 462(7273):628–632, 2009.
- [48] JE Lye, L Fallani, Michele Modugno, DS Wiersma, C Fort, and Massimo Inguscio. Bose-einstein condensate in a random potential. *Physical review letters*, 95(7):070401, 2005.
- [49] Giacomo Roati, Chiara D’Errico, Leonardo Fallani, Marco Fattori, Chiara Fort, Matteo Zaccanti, Giovanni Modugno, Michele Modugno, and Massimo Inguscio. Anderson localization of a non-interacting bose–einstein condensate. *Nature*, 453(7197):895–898, 2008.
- [50] Juliette Billy, Vincent Josse, Zhanchun Zuo, Alain Bernard, Ben Hambrecht, Pierre Lujan, David Clément, Laurent Sanchez-Palencia, Philippe Bouyer, and Alain Aspect. Direct observation of anderson localization of matter waves in a controlled disorder. *Nature*, 453(7197):891–894, 2008.
- [51] SS Kondov, WR McGehee, JJ Zirbel, and B DeMarco. Three-dimensional anderson localization of ultracold matter. *Science*, 334(6052):66–68, 2011.
- [52] André Schirotzek, Cheng-Hsun Wu, Ariel Sommer, and Martin W Zwierlein. Observation of fermi polarons in a tunable fermi liquid of ultracold atoms. *Physical review letters*, 102(23):230402, 2009.
- [53] Sylvain Nascimbene, Nir Navon, KJ Jiang, Leticia Tarruell, Martin Teichmann, Jason Mckeever, Frédéric Chevy, and Christophe Salomon. Collective oscillations of an imbalanced fermi gas: axial compression modes and polaron effective mass. *Physical review letters*, 103(17):170402, 2009.

- [54] Christoph Kohstall, Matteo Zaccanti, Matthias Jag, Andreas Trenkwalder, Pietro Massignan, Georg M Bruun, Florian Schreck, and Rudolph Grimm. Metastability and coherence of repulsive polarons in a strongly interacting fermi mixture. *Nature*, 485(7400):615–618, 2012.
- [55] Cheng Chin, Rudolf Grimm, Paul Julienne, and Eite Tiesinga. Feshbach resonances in ultracold gases. *Reviews of Modern Physics*, 82(2):1225, 2010.
- [56] TG Tiecke. Properties of potassium. *University of Amsterdam, The Netherlands, Thesis*, 2010.
- [57] D. C. McKay, D. Jervis, D. J. Fine, J. W. Simpson-Porco, G. J. A. Edge, and J. H. Thywissen. Low-temperature high-density magneto-optical trapping of potassium using the open  $4s \rightarrow 5p$  transition at 405 nm. *Phys. Rev. A*, 84, 2011.
- [58] J Goldwin, S Inouye, M L Olsen, B Newman, B Depaola, and D S Jin. Measurement of the interaction strength in a Bose-Fermi mixture with  $^{87}\text{Rb}$  and  $^{40}\text{K}$ . *Phys. Rev. A*, 70:021601, 2004.
- [59] Michael Köhl, Henning Moritz, Thilo Stöferle, Kenneth Günter, and Tilman Esslinger. Fermionic atoms in a three dimensional optical lattice: Observing fermi surfaces, dynamics, and interactions. *Phys. Rev. Lett.*, 94:080403, 2005.
- [60] Bernd Fröhlich, Michael Feld, Enrico Vogt, Marco Koschorreck, Wilhelm Zwerger, and Michael Köhl. Radio-frequency spectroscopy of a strongly interacting two-dimensional fermi gas. *Phys. Rev. Lett.*, 106:105301, 2011.
- [61] D. J. Wineland and W. M. Itano. Laser cooling of atoms. *Phys. Rev. A*, 20:1521–1540, 1979.
- [62] V. S. Letokhov and V. G. Minogin. *Phys. Rep.*, 73:1, 1981.
- [63] A. Ashkin and J. P. Gordon. *Op. Lett.*, 4:161–163, 1979.
- [64] Harald F. Hess. Evaporative cooling of magnetically trapped and compressed spin-polarized hydrogen. *Phys. Rev. B*, 34:3476–3479, 1986.
- [65] O. J. Luiten, M. W. Reynolds, and J. T. M. Walraven. Kinetic theory of the evaporative cooling of a trapped gas. *Phys. Rev. A*, 53:381–389, 1996.
- [66] B DeMarco and D S Jin. Onset of Fermi degeneracy in a trapped atomic gas. *Science*, 285:1703–1706, 1999.

- [67] J. D. Miller, R. A. Cline, and D. J. Heinzen. Far-off-resonance optical trapping of atoms. *Phys. Rev. A*, 47:R4567–R4570, 1993.
- [68] K. M. O’Hara, S. R. Granade, M. E. Gehm, T. A. Savard, S. Bali, C. Freed, and J. E. Thomas. Ultrastable  $\text{CO}_2$  laser trapping of Lithium fermions. *Phys. Rev. Lett.*, 82:4204–4207, 1999.
- [69] Felix Stubenrauch. Frequency modulation saturation spectroscopy laser lock of an interference-filter-stabilized external-cavity diode laser. Technical report, University of Toronto, 2010, 2010.
- [70] Matthias Scholl. Interference filter stabilized external cavity diode laser. Technical report, University of Toronto, 2010, 2010.
- [71] X Baillard, A Gauguet, S Bize, P Lemonde, Ph Laurent, A Clairon, and P Rosenbusch. Interference-filter-stabilized external-cavity diode lasers. *Optics Communications*, 266(2), 2006.
- [72] B DeMarco, H Rohner, and DS Jin. An enriched  $^{40}\text{K}$  source for fermionic atom studies. *Review of Scientific Instruments*, 70(4), 1999.
- [73] Brian DeMarco. *Quantum behavior of an atomic Fermi gas*. PhD thesis, University of Colorado, 2001.
- [74] William Happer. Optical pumping. *Rev. Mod. Phys.*, 44:169–249, 1972.
- [75] C. Cohen-Tannoudji. Optical pumping with lasers. In G. Putlitz, E. W. Weber, and A. Winnacker, editors, *Atomic Physics*, volume 4, pages 589–614. Springer, 1975.
- [76] Josefine Metzkes. Design of a magnetic transport system. Technical report, University of Toronto, 2008, 2008.
- [77] Michael Yee. Magnetic trapping and transport of ultracold atoms, Bachelors Thesis, University of Toronto, 2009.
- [78] Markus Greiner, Immanuel Bloch, Theodor W Hänsch, and Tilman Esslinger. Magnetic transport of trapped cold atoms over a large distance. *Physical Review A*, 63, 2001.
- [79] A. Stummer. CATS 2 - Cold Atoms Transfer System, <http://www.physics.utoronto.ca/~astummer>, 2009.
- [80] Tin-Lun Ho and Qi Zhou. Squeezing the entropy of fermions in optical lattices. *Proc. Nat. Acad. Sci.*, 106:6916–6920, 2008.

- [81] Jean-Sébastien Bernier, Corinna Kollath, Antoine Georges, Lorenzo De Leo, Fabrice Gerbier, Christophe Salomon, and Michael Köhl. Cooling fermionic atoms in optical lattices by shaping the confinement. *Phys. Rev. A*, 79:061601, 2009.
- [82] Charles J. M. Mathy, David A. Huse, and Randall G. Hulet. Enlarging and cooling the Néel state in an optical lattice. *Phys. Rev. A*, 86:023606, 2012.
- [83] U Ernst, A Marte, F Schreck, J Schuster, and G Rempe. Bose-einstein condensation in a pure ioffe-pritchard field configuration. *EPL (Europhysics Letters)*, 41(1):1, 1998.
- [84] Wolfgang Petrich, Michael H Anderson, Jason R Ensher, and Eric A Cornell. Stable, tightly confining magnetic trap for evaporative cooling of neutral atoms. *Physical Review Letters*, 74(17):3352, 1995.
- [85] J.H. Thywissen. Majorana depolarization in a quadrupole trap. Technical report, University of Toronto, 2011, 2011.
- [86] Kerson Huang. Statistical mechanics, john wily & sons, 1963.
- [87] KB Davis, M-O Mewes, MR van Andrews, NJ Van Druten, DS Durfee, DM Kurn, and W Ketterle. Bose-einstein condensation in a gas of sodium atoms. *Physical Review Letters*, 75(22):3969, 1995.
- [88] Romain Dubessy, Karina Merloti, Laurent Longchambon, P-E Pottie, Thomas Liennard, Aurélien Perrin, Vincent Lorent, and Hélène Perrin. Rubidium-87 bose-einstein condensate in an optically plugged quadrupole trap. *Physical Review A*, 85(1):013643, 2012.
- [89] Jonathan Michael Goldwin. *Quantum degeneracy and interactions in the 87Rb-40K Bose-Fermi mixture*. PhD thesis, University of Colorado, 2005.
- [90] Thorsten Best. *Interacting Bose-Fermi mixtures in optical lattices*. PhD thesis, Ph. D. Thesis, Universität Mainz, 2011.
- [91] G. Bruun and C. Clark. Ideal gases in time-dependent traps. *Phys. Rev. A*, 61, 2000.
- [92] Thad Walker, David Sesko, and Carl Wieman. Collective behavior of optically trapped neutral atoms. *Phys. Rev. Lett.*, 64:408–411, 1990.
- [93] John Weiner, Vanderlei S. Bagnato, Sergio Zilio, and Paul S. Julienne. Experiments and theory in cold and ultracold collisions. *Rev. Mod. Phys.*, 71:1–85, 1999.
- [94] P.D. Lett, W.D. Phillips, S.L. Rolston, C.E. Tanner, R.N. Watts, and C.I. Westbrook. Optical molasses. *J. Opt. Soc. Am. B*, 6:2084, 1989.

- [95] J. Dalibard and C. Cohen-Tannoudji. Laser cooling below the doppler limit by polarization gradients: simple theoretical models. *J. Opt. Soc. Am. B*, 6:2023–2045, 1989.
- [96] Zhong Lin, Kazuko Shimizu, Mingsheng Zhan, Fujio Shimizu, and Hiroshi Takuma. Laser cooling and trapping of li. *Jpn. J. Appl. Phys.*, 30(Part 2, No. 7B):L1324–L1326, 1991.
- [97] G. Modugno, C. Benkő, P. Hannaford, G. Roati, and M. Inguscio. Sub-doppler laser cooling of fermionic  $^{40}\text{K}$  atoms. *Phys. Rev. A*, 60:R3373, 1999.
- [98] F. S. Cataliotti, E. A. Cornell, C. Fort, M. Inguscio, F. Marin, M. Prevedelli, L. Ricci, and G. M. Tino. Magneto-optical trapping of fermionic potassium atoms. *Phys. Rev. A*, 57:1136–1138, 1998.
- [99] B. DeMarco and D. S. Jin. Onset of Fermi degeneracy in a trapped atomic gas. *Science*, 285(5434):1703–1706, 1999.
- [100] K.R. Vogel, T.P. Dinneen, A. Gallagher, and J.L. Hall. Narrow-line doppler cooling of strontium to the recoil limit. *IEEE Trans. Instrum. Meas.*, 48:618–621, 1999.
- [101] Hidetoshi Katori, Tetsuya Ido, Yoshitomo Isoya, and Makoto Kuwata-Gonokami. Magneto-optical trapping and cooling of strontium atoms down to the photon recoil temperature. *Phys. Rev. Lett.*, 82:1116–1119, 1999.
- [102] J. C. J. Koelemeij, R. J. W. Stas, W. Hogervorst, and W. Vassen. Magneto-optical trap for metastable helium at 389 nm. *Phys. Rev. A*, 67:053406, 2003.
- [103] A. S. Tychkov, J. C. J. Koelemeij, T. Jeltens, W. Hogervorst, and W. Vassen. Two-color magneto-optical trap for metastable helium. *Phys. Rev. A*, 69:055401, 2004.
- [104] J. J. McClelland and J. L. Hanssen. Laser cooling without repumping: A magneto-optical trap for erbium atoms. *Phys. Rev. Lett.*, 96:143005, 2006.
- [105] Saijun Wu, Thomas Plisson, Roger C. Brown, William D. Phillips, and J. V. Porto. Multiphoton magneto-optical trap. *Phys. Rev. Lett.*, 103:173003, 2009.
- [106] P. M. Duarte, R. A. Hart, J. M. Hitchcock, T. A. Corcovilos, T. L. Yang, A. Reed, and R. G. Hulet. All-optical production of a lithium quantum gas using narrow-line laser cooling. 2011.
- [107] E. B. Norrgard D. DeMille J. F. Barry, E. S. Shuman. Laser radiation pressure slowing of a molecular beam. 2011.

- [108] J. E. Sansonetti. Wavelengths, transition probabilities, and energy levels for the spectra of potassium (k i through k xix). *J. Phys. Chem. Ref. Data*, 37:7, 2008.
- [109] H. Wang, J. Li, X. T. Wang, C. J. Williams, P. L. Gould, and W. C. Stwalley. Precise determination of the dipole matrix element and radiative lifetime of the  $^{39}\text{k}$  4p state by photoassociative spectroscopy. *Phys. Rev. A*, 55:R1569–R1572, 1997.
- [110] R.W. Berends, W. Kedzierski, J.B. Atkinson, and L. Krause. The radiative lifetimes of the potassium 5p,6p and 7p states. *Sp. Acta*, 43B:1069, 1988.
- [111] A. Mills, J. A. Behr, L. A. Courneyea, and M. R. Pearson. Lifetime of the potassium  $5p_{1/2}$  state. *Phys. Rev. A*, 72:024501, 2005.
- [112] E. Arimondo, M. Inguscio, and P. Violino. Experimental determinations of the hyperfine structure in the alkali atoms. *Rev. Mod. Phys.*, 49:31, 1977.
- [113] U. Gustafsson, J. Alnis, and S Svanberg. Atomic spectroscopy with violet laser diodes. *Am. J. Phys.*, 68:660, 2000.
- [114] Ulf Gustafsson, Gabriel Somesfalean, Janis Alnis, and Sune Svanberg. Frequency-modulation spectroscopy with blue diode lasers. *Applied Optics*, 39:3774, 2000.
- [115] S. Uetake, K. Hayasaka, and M. Watanabe. Saturation spectroscopy of potassium for frequency stabilization of violet diode lasers. *Jpn. J. Appl. Phys.*, 42:L332, 2003.
- [116] L.J.S. Halloran, S. Fostner, E. Paradis, and J.A. Behr. Specific mass shift of potassium  $5p_{1/2}$  state. *Op. Comm.*, 282:554, 2009.
- [117] Alexandra Behrle, Marco Koschorreck, and Michael Köhl. Isotope shift and hyperfine splitting of the  $4s \rightarrow 5p$  transition in potassium. *Phys. Rev. A*, 83:052507, 2011.
- [118] Chang Yong Park and Tai Hyun Yoon. Frequency stabilization of injection-locked violet laser diode with doppler-free absorption signal of ytterbium. *Jpn. J. Appl. Phys.*, 42:L754–L756, 2003.
- [119] Kaduki Komori, Yosuke Takasu, Mitsutaka Kumakura, Yoshiro Takahashi, and Tsutomu Yabuzaki. Injection-locking of blue laser diodes and its application to the laser cooling of neutral ytterbium atoms. *Jpn. J. Appl. Phys.*, 42:5059, 2003.
- [120] R. V. Ambartzumian, N. P. Furzikov, V. S. Letokhov, and A. A. Puretsky. Measuring photoionization cross-sections of excited atomic states. *Appl. Phys.*, 9:335, 1976.

- [121] Marco Anderlini, Emmanuel Courtade, Donatella Ciampin, Jörg H. Müller, Oliver Morsch, and Ennio Arimondo. Two-photon ionization of cold rubidium atoms. *J. Opt. Soc. Am. B*, 21:480, 2004.
- [122] E. Courtade, M. Anderlini, D. Ciampini, J. H. Müller, O. Morsch, E. Arimondo, M. Aymar, and E. J. Robinson. Two-photon ionization of cold rubidium atoms with a near resonant intermediate state. *J. Phys. B*, 37:967, 2004.
- [123] I.D. Petrov, V.L. Sukhorukov, E. Leber, and H. Hotop. Near threshold photoionization of excited alkali atoms  $ak(np)$  ( $ak = na, k, rb, cs; n = 3-6$ ). *Euro. Phys. J. D*, 10:53, 2000.
- [124] Nasir Amina, S. Mahmooda, S.U. Haqa, M.A. Kalyara, M. Rafiq, and M.A. Baig. Measurements of photoionization cross sections from the 4p, 5d and 7s excited states of potassium. *J. Quant. Spec. Rad. Trans.*, 109:863, 2008.
- [125] Timothy P. Dinneen, Christopher D. Wallace, Kit-Yan N. Tan, and Phillip L. Gould. Use of trapped atoms to measure absolute photoionization cross sections. *Op. Lett.*, 17:1706, 1992.
- [126] G. Modugno, G. Roati, M. Inguscio, M.S. Santos, G.D. Telles, L.G. Marcass, and V.S. Bagnato. Comparative investigation of  $^{39}k$  and  $^{40}k$  trap loss rates: alternative loss channel at low light intensities. *Euro. Phys. J. D*, 23:409, 2003.
- [127] Tobias Tiecke. *Feshbach resonances in ultracold mixtures of the fermionic quantum gases  $^6Li$  and  $^{40}K$* . PhD thesis, University of Amsterdam, 2009.
- [128] A. Ridinger, S. Chaudhuri, T. Salez, U. Eismann, D. R. Fernandes, K. Magalhães, D. Wilkowski, C. Salomon, and F. Chevy. Large atom number dual-species magneto-optical trap for fermionic  $^6Li$  and  $^{40}K$  atoms. 2011.
- [129] Thierry Chanelière, Jean-Louis Meunier, Robin Kaiser, Christian Miniatura, and David Wilkowski. Extra-heating mechanism in Doppler cooling experiments. *J. Opt. Soc. Am. B*, 22:1819, 2005.
- [130] M. Landini, S. Roy, L. Carcagní, D. Trypogeorgos, M. Fattori, M. Inguscio, and G. Modugno. Sub-doppler laser cooling of potassium atoms. 2011.
- [131] Phillip L Gould, George A Ruff, and David E Pritchard. Diffraction of atoms by light: The near-resonant Kapitza-Dirac effect. *Physical review letters*, 56(8):827–830, 1986.

- [132] Peter J Martin, Bruce G Oldaker, Andrew H Miklich, and David E Pritchard. Bragg scattering of atoms from a standing light wave. *Physical review letters*, 60(6):515, 1988.
- [133] Steffen Wolf, Steven J Oliver, and David S Weiss. Suppression of recoil heating by an optical lattice. *Phys. Rev. Lett.*, 85(20), 2000.
- [134] GK Campbell, MM Boyd, JW Thomsen, MJ Martin, S Blatt, MD Swallows, TL Nicholson, T Fortier, CW Oates, SA Diddams, et al. Probing interactions between ultracold fermions. *science*, 324(5925):360–363, 2009.
- [135] JD Thompson, BM Zwickl, AM Jayich, Florian Marquardt, SM Girvin, and JGE Harris. Strong dispersive coupling of a high-finesse cavity to a micromechanical membrane. *Nature*, 452(7183):72–75, 2008.
- [136] Kristian Baumann, Christine Guerlin, Ferdinand Brennecke, and Tilman Esslinger. Dicke quantum phase transition with a superfluid gas in an optical cavity. *Nature*, 464(7293):1301–1306, 2010.
- [137] Robert Raussendorf and Hans J Briegel. Quantum computing via measurements only. *arXiv preprint quant-ph/0010033*, 2000.
- [138] Markus Greiner, Olaf Mandel, Tilman Esslinger, Theodor W Hänsch, and Immanuel Bloch. Quantum phase transition from a superfluid to a mott insulator in a gas of ultracold atoms. *Nature*, 415(6867):39–44, 2002.
- [139] JR Williams, JH Huckans, RW Stites, EL Hazlett, and KM O'Hara. Preparing a highly degenerate fermi gas in an optical lattice. *Physical Review A*, 82(1):011610, 2010.
- [140] Jinyang Liang, Rudolph N Kohn Jr, Michael F Becker, Daniel J Heinzen, et al. 1.5% root-mean-square flat-intensity laser beam formed using a binary-amplitude spatial light modulator. *Applied optics*, 48(10):1955–1962, 2009.
- [141] N.W. Ashcroft and D.N. Mermin. Solid state physics. *Harcourt*, 1976.
- [142] Stefan Trotzky, Patrick Cheinet, Simon Fölling, M Feld, Ute Schnorrberger, Ana Maria Rey, Anatoli Polkovnikov, EA Demler, MD Lukin, and I Bloch. Time-resolved observation and control of superexchange interactions with ultracold atoms in optical lattices. *Science*, 319(5861):295–299, 2008.
- [143] W. Zwerger. Mott-hubbard transition of cold atoms in optical lattices. *Opt. B: Quantum Semiclass. Opt*, 5, 2003.

- [144] Eugene Demler. Strongly correlated systems in atomic and condensed matter physics. Course Notes, Harvard, 2011.
- [145] F Werner, O Parcollet, A Georges, and SR Hassan. Interaction-induced adiabatic cooling and antiferromagnetism of cold fermions in optical lattices. *arXiv preprint cond-mat/0504003*, 2005.
- [146] Robert W. Boyd. Nonlinear optics. *Academic Press*, 2003.
- [147] R. G. Smith. Optical power handling capacity of low loss optical fibers as determined by stimulated raman and brillouin scattering. *Appl. Opt.*, 11, 1972.
- [148] J Hecker Denschlag, JE Simsarian, H Häffner, C McKenzie, A Browaeys, D Cho, K Helmerson, SL Rolston, and WD Phillips. A bose-einstein condensate in an optical lattice. *Journal of Physics B: Atomic, Molecular and Optical Physics*, 35(14):3095, 2002.
- [149] PL Kapitza and PAM Dirac. The reflection of electrons from standing light waves. In *Mathematical Proceedings of the Cambridge Philosophical Society*, volume 29, pages 297–300. Cambridge Univ Press, 1933.
- [150] Thilo Stöferle, Henning Moritz, Christian Schori, Michael Köhl, and Tilman Esslinger. Transition from a strongly interacting 1d superfluid to a mott insulator. *Physical review letters*, 92(13):130403, 2004.
- [151] IB Spielman, WD Phillips, and JV Porto. Mott-insulator transition in a two-dimensional atomic bose gas. *Physical review letters*, 98(8):080404, 2007.
- [152] Parvis Soltan-Panahi, Julian Struck, Philipp Hauke, Andreas Bick, Wiebke Plenkers, Georg Meineke, Christoph Becker, Patrick Windpassinger, Maciej Lewenstein, and Klaus Sengstock. Multi-component quantum gases in spin-dependent hexagonal lattices. *Nature Physics*, 7(5):434–440, 2011.
- [153] U Schnorrberger, JD Thompson, S Trotzky, R Pugatch, N Davidson, S Kuhr, and I Bloch. Electromagnetically induced transparency and light storage in an atomic mott insulator. *Physical review letters*, 103(3):033003, 2009.
- [154] B Capogrosso-Sansone, NV Prokof'ev, and BV Svistunov. Phase diagram and thermodynamics of the three-dimensional bose-hubbard model. *Physical Review B*, 75(13):134302, 2007.

- [155] Markus Greiner, Immanuel Bloch, Olaf Mandel, Theodor W Hänsch, and Tilman Esslinger. Exploring phase coherence in a 2d lattice of bose-einstein condensates. *Physical Review Letters*, 87(16):160405, 2001.
- [156] Tatjana Gericke, Peter Würtz, Daniel Reitz, Tim Langen, and Herwig Ott. High-resolution scanning electron microscopy of an ultracold quantum gas. *Nature Physics*, 4(12):949–953, 2008.
- [157] Bruno Zimmermann, Torben Mueller, Jakob Meineke, Tilman Esslinger, and Henning Moritz. High-resolution imaging of ultracold fermions in microscopically tailored optical potentials. *New Journal of Physics*, 13(4):043007, 2011.
- [158] M Karski, L Förster, JM Choi, W Alt, A Widera, and D Meschede. Nearest-neighbor detection of atoms in a 1d optical lattice by fluorescence imaging. *Physical review letters*, 102(5):053001, 2009.
- [159] Sandra Van Aert, Kees J Batenburg, Marta D Rossell, Rolf Erni, and Gustaaf Van Tendeloo. Three-dimensional atomic imaging of crystalline nanoparticles. *Nature*, 470(7334):374–377, 2011.
- [160] Max Born and Emil Wolf. *Principles of Optics*. Cambridge University Press.
- [161] Xiaowei Zhuang. Nano-imaging with storm. *Nature photonics*, 3(7):365, 2009.
- [162] A. Mazouchi. Feasibility of imaging single atoms in an optical lattice. Master’s thesis, University of Toronto, 2007.
- [163] C. Kierans. Testing of a microscope for site-resolved imaging of atoms in an optical lattice. Master’s thesis, University of Toronto, 2012.
- [164] Gabriello Presenza-Pitman. Determination of the contrast and modulation transfer functions for high resolution imaging of individual atoms. Technical report, University of Toronto, 2009, 2009.
- [165] Nathan J. Wittenberg Timothy W. Johnson Nathan C. Lindquist Prashant Nagpal David J. Norris Hyungsoon Im, Si Hoon Lee and Sang-Hyun Oh. Template-stripped smooth ag nanohole arrays with silica shells for surface plasmon resonance biosensing. *ACS Nano*.
- [166] G L Gattobigio, T Pohl, G Labeyrie, and R Kaiser. New method for illumination of photomicrographic purposes. *Journal of the Royal Microscopical Society*, 14, 1894.

- [167] Thomas Maier. Stability testing of a microscope stack. Technical report, University of Toronto, 2012, 2012.
- [168] P. M. Duarte, R. A. Hart, J. M. Hitchcock, T. A. Corcovilos, T.-L. Yang, A. Reed, and R. G. Hulet. All-optical production of a lithium quantum gas using narrow-line laser cooling. *Phys. Rev. A*, 84, 2011.
- [169] Paul D Lett, Richard N Watts, Christoph I Westbrook, William D Phillips, Phillip L Gould, Harold J Metcalf, et al. Observation of atoms laser cooled below the doppler limit. *Physical Review Letters*, 61(2):169–172, 1988.
- [170] M Landini, S Roy, L Carcagní, D Trypogeorgos, M Fattori, M Inguscio, and G Modugno. Sub-doppler laser cooling of potassium atoms. *Physical Review A*, 84(4):043432, 2011.
- [171] D Boiron, A Michaud, P Lemonde, Y Castin, C Salomon, S Weyers, K Szymaniec, L Cognet, and A Clairon. Laser cooling of cesium atoms in gray optical molasses down to  $1.1 \mu\text{k}$ . *Physical Review A*, 53(6):R3734, 1996.
- [172] D Fernandes, Franz Sievers, Norman Kretschmar, Saijun Wu, C. Salomon, and Frederic Chevy. Sub-doppler laser cooling of fermionic  $^{40}\text{K}$  atoms in three-dimensional gray optical molasses. *Europhysics Letters(EPL)*, 100, 2012.
- [173] A Aspect, E Arimondo, R e al Kaiser, N Vansteenkiste, and C Cohen-Tannoudji. Laser cooling below the one-photon recoil energy by velocity-selective coherent population trapping. *Physical Review Letters*, 61(7):826, 1988.
- [174] Mark Kasevich, Steven Chu, et al. Laser cooling below a photon recoil with three-level atoms. *Physical review letters*, 69(12):1741–1744, 1992.
- [175] Andrew T. Grier, Igor Ferrier-Barbut, Benno S. Rem, Marion Delehaye, Lev Khaykovich, Frédéric Chevy, and Christophe Salomon.  $\lambda$ -enhanced sub-doppler cooling of lithium atoms in  $D_1$  gray molasses. *Phys. Rev. A*, 87, 2013.
- [176] Guillaume Salomon, Lauriane Fouché, Pengjun Wang, Alain Aspect, Philippe Bouyer, and Thomas Bourdel. Gray-molasses cooling of  $^{39}\text{K}$  to a high phase-space density. *EPL (Europhysics Letters)*, 104(6):63002, 2013.
- [177] Dipankar Nath, R Kollengode Easwaran, G Rajalakshmi, and CS Unnikrishnan. Quantum-interference-enhanced deep sub-doppler cooling of  $^{39}\text{K}$  atoms in gray molasses. *Physical Review A*, 88(5):053407, 2013.

- [178] D Boiron, A Michaud, JM Fournier, L Simard, M Sprenger, G Grynberg, and C Salomon. Cold and dense cesium clouds in far-detuned dipole traps. *Physical Review A*, 57(6):R4106, 1998.
- [179] J. Dalibard and C. Cohen-Tannoudji. Laser cooling below the doppler limit by polarization gradients: simple theoretical models. *J. Opt. Soc. Am. B*, 6, 1989.
- [180] G Grynberg and J-Y Courtois. Proposal for a magneto-optical lattice for trapping atoms in nearly-dark states. *EPL (Europhysics Letters)*, 27(1):41, 1994.
- [181] Will Cairncross. Interference filter stabilized external cavity diode laser. 2011.
- [182] Gregory E Hall and Simon W North. Transient laser frequency modulation spectroscopy. *Annual review of physical chemistry*, 51, 2000.
- [183] MS Shahriar, PR Hemmer, MG Prentiss, P Marte, J Mervis, DP Katz, NP Bigelow, and T Cai. Continuous polarization-gradient precooling-assisted velocity-selective coherent population trapping. *Physical Review A*, 48(6):R4035, 1993.
- [184] Z. Idziaszek, L. Santos, M. Baranov, and M. Lewenstein. Laser cooling of a trapped two-component fermi gas. *Phys. Rev. A*, 67, 2003.
- [185] Gregory Breit and II Rabi. Measurement of nuclear spin. *Physical Review*, 38(11):2082, 1931.
- [186] Rudolf Grimm, Matthias Weidemüller, and Yurii B Ovchinnikov. Optical dipole traps for neutral atoms. *arXiv preprint physics/9902072*, 1999.
- [187] JP Gordon and A Ashkin. Motion of atoms in a radiation trap. *Physical Review A*, 21(5):1606, 1980.